

Title	ポリビニルブチラルのレオロジー特性と自己修復性
Author(s)	Arayachukiat, Sunatda
Citation	
Issue Date	2015-03
Type	Thesis or Dissertation
Text version	ETD
URL	http://hdl.handle.net/10119/12766
Rights	
Description	Supervisor:山口 政之, マテリアルサイエンス研究科, 博士

Rheological and Self-healing Properties of
Poly(vinyl butyral)

SUNATDA ARAYACHUKIAT

Japan Advanced Institute of Science and Technology
Rheological and Self-healing Properties of

Doctoral Dissertation

Rheological and Self-healing Properties of
Poly(vinyl butyral)

by

SUNATDA ARAYACHUKIAT

Supervisor: **Professor Dr. Masayuki Yamaguchi**

School of Materials Science
Japan Advanced Institute of Science and Technology

March 2015

Referee-in-chief : **Professor Dr. Masayuki Yamaguchi**
Japan Advanced Institute of Science and Technology

Referees : **Professor Dr. Noriyoshi Matsumi**
Japan Advanced Institute of Science and Technology

Associate Professor Dr. Yuki Nagao
Japan Advanced Institute of Science and Technology

Associate Professor Dr. Toshiaki Taniike
Japan Advanced Institute of Science and Technology

Associate Professor Dr. Ken Kojio
Kyushu University

Abstract

The rheological and self-healing properties of Poly(vinyl butyral) (PVB) are studied. It is found from the viscoelastic measurements that the polymer has low level of entanglement molecular weight M_e and high rubbery plateau modulus G_N^0 . Because of the relatively high value of G_N^0 , it hardly shows shark-skin failure, i.e., the surface roughness on the extrudates at extrusion processing. Therefore, it can be processed at high out-put rate condition. Moreover, the low M_e is responsible for a rubbery region in the wide temperature range. Therefore, it barely shows macroscopic flow in the rubbery region. Furthermore, it is found that PVB shows self-healing behavior even below the glass transition temperature T_g . A large amount of water is found to be adsorbed on the surface of the film. This is attributed to the surface localization of hydroxyl and carbonyl group in PVB, which is confirmed by X-ray photoelectron spectroscopy. Since the surface is plasticized by the water, the scar applied by a razor blade is healed even in the glassy state of the bulk. Moreover, the healing efficiency is enhanced at high humidity condition, owing to the pronounced plasticizing effect by water. This can be noted that self-healing products of PVB are appropriate to be used for outdoor goods.

KEYWORDS: rheology; capillary extrusion; viscoelastic properties; self-healing property; thermoplastics

Preface

Rheology is a modern science related to deformation and flow. It is very important to control the mechanical responses in many applications for plastics, rubbers, fibers, adhesives and paints. Moreover, the molecular motion, a kind of rheological responses, can be used for the self-healing behavior. Poly(vinyl butyral) (PVB), which is widely used in adhesives and paints, is employed for this study, because it can be a good candidate in a self-healing glassy polymer.

In this thesis, self-healing and rheological properties of PVB are demonstrated. I hope the study would provide useful information on the design of self-healing materials.

Sunatda Arayachukiat

Contents

Chapter 1	General Introduction	1
1.1	Introduction	1
1.2	Polymer rheology.....	2
1.2.1	Viscous property	3
1.2.2	Linear viscoelastic property.....	4
1.2.3	Rouse model.....	5
1.2.4	Time-Temperature Superposition (TTS).....	7
1.2.5	Stress relaxation.....	8
1.3	Rheology properties of amorphous polymers.....	10
1.3.1	Four regions of polymers.....	11
1.3.2	Glassy region.....	11
1.3.3	Transition region.....	12
1.3.4	Rubbery region.....	18
1.3.5	Flow region.....	22
1.4	Objective of this research.....	23
	References.....	24

Chapter 2	Rheological Property of Poly(Vinyl Butyral)	28
2.1	Introduction	28
2.1.1	Poly(vinyl butyral)	28
2.1.2	Poly(vinyl acetate)(PVAc)	31
2.1.3	Poly(vinyl alcohol)(PVA)	32
2.1.4	Processability	33
2.1.5	Capillary extrusion	33
2.1.6	Flow instability	35
2.2	Experimental	40
2.2.1	Materials	40
2.2.2	Sample Preparation	41
2.2.3	Measurements	42
2.3	Results and discussion	44
2.3.1	Linear viscoelastic properties	44
2.3.2	Capillary extrusion properties	53
2.4	Conclusions	61
	References	62

Chapter 3	Self-Healing Behavior of Poly(Vinyl Butyral)	66
3.1	Introduction	66
3.1.1	Approaches to self-healing	68
3.1.1.1	Capsule-based self-healing materials	68
3.1.1.2	Vascular self-healing materials	71
3.1.1.3	Self-healing from dispersed thermoplastic polymer	74
3.1.1.4	Self-healing polymers based on reversible reactions	75
3.1.1.5	Ionomeric self-healing materials	77
3.1.1.6	Supramolecular self-healing materials	77
3.1.1.7	Self-healing via molecular diffusion	79
3.1.2	Characterization methods	84
3.1.2.1	Attenuated total reflectance fourier transform infrared spectroscopy (ATR-FTIR)	84
3.1.2.2	X-ray photoelectron (XPS)	86
3.2	Materials	88
3.2.1	Sample Preparation	88
3.3	Measurements	89

3.4	Results and discussion.....	91
3.5	Conclusions.....	108
	References.....	109
Chapter 4	General Conclusions.....	117
	Achievements.....	120
	Abstract of Minor Research Theme.....	123
	Acknowledgements.....	153

This dissertation was prepared according to the curriculum for the Collaborative Education Program organized by Japan Advanced Institute of Science and Technology and Chulalongkorn University.

Chapter 1

General Introduction

1.1 Introduction

Rheology is a branch of physics that deals with the deformation and flow of a material under stress. Therefore, rheological properties play important roles in many applications to provide desired mechanical responses. In other words, rheological control is inevitable to establish a new material design for functional materials with specific mechanical responses, such as thermoplastic elastomer, shape-memory material, and damping material. A self-healing material is one of them, because it shows anomalous behavior of molecular motion. In particular, a self-healing ability provided by molecular motion can be explained by the rheological response.

Self-healing materials have the ability to restore their original properties even when they are damaged through thermal, mechanical, ballistic or other means. Up to now, various methods have been proposed to provide this function as one of the biomimetic properties. Although specific methods using chemical reaction have been focused recently, most of them will not be employed in industry because of their poor cost-performance. In contrast, self-healing materials using molecular diffusion have the great possibility for industrial application. Basically, it is possible to provide the healing ability for all

thermoplastic resin, because they slow marked molecular motion beyond the melting point or glass transition temperature. The most serious problem for this method is macroscopic deformation, i.e., flow. To overcome the difficulty to show healing behavior without flow, a weak gel with a lot of dangling chains was proposed as a self-healing polymer. Because of the permanent network structure in a gel, it does not flow macroscopically. Further, molecular interdiffusion through the boundary of cut area occurs by means of molecular motion of dangling chains. However, it has not been applied in industry yet by the following two reasons; the difficulty to increase the modulus and the thermosetting nature, not thermoplastic one. In this study, self-healing ability is investigated using a thermoplastic, glassy polymer at room temperature with detailed characterization of the rheological properties.

1.2 Polymer Rheology

Besides the phenomenological approach, the rheological study is usually performed based on the relation between molecular motion and its mechanical responses such as elasticity and viscosity. Since rheology is defined as the science of deformation and flow, it involves the measurements under controlled flow and/or deformation. In general, polymer liquids exhibit non-Newtonian flow behavior, and most polymer solids exhibit non-linear elastic properties. Furthermore, real polymer bodies show both elastic and viscous responses, i.e., viscoelasticity. Because of the long-chain nature of polymeric materials, their viscoelastic characteristics come to the forefront. This is especially pronounced when the times for molecular relaxation are of the same order of time scale of an imposed mechanical stimulus. Such situation occurs even at processing operations.

1.2.1 Viscous property

Viscosity is a property to describe a resistance to flow. It can be measured under shear flow or elongational flow. Viscosity can be considered as a friction between neighboring layers in a fluid that are moving at different flow velocities as a laminar flow. When a fluid flows in a tube, molecules in the center of tube move fast and those near its walls move slow. This is one type of shear flow generated by pressure difference. The other type of shear flow is generated by moving a liquid by sliding a plate on the liquid, i.e., drag flow. At the drag flow, the shear force F is required to impose the plate motion. Following the Newton's law, viscosity η is defined as the ratio of shear stress ($\sigma = F/A$), and shear rate $\dot{\gamma}$, where A is the area of the plate.

$$\sigma = \eta \dot{\gamma} \tag{1-1}$$

Besides superfluid, all fluids have positive viscosity, when the viscosity is very high, for instance in pitch, the fluid will behave as a solid under high strain rates.

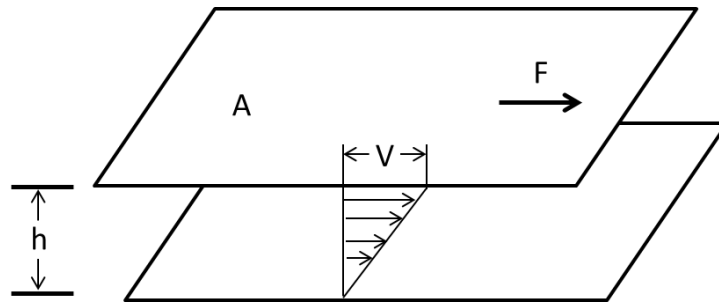


Figure 1-1 Laminar shear of fluid between two plates: friction force between the fluid and the boundaries is caused by shear. Viscosity is given by the stress (F/A) divided by the shear rate (V/h).

1.2.2 Linear viscoelastic property

Linear viscoelastic properties provide basic characterization of a polymer. Some rheometers such as cone-and-plate rheometer and parallel-plate rheometer are used to measure the linear viscoelastic properties under shear strain. The common method to evaluate the linear viscoelasticity is the small-amplitude oscillatory shear measurement. In the oscillatory shear measurement, both shear stress σ and strain γ are measured as a function of angular frequency ω . (Equations 1-2 and 1-3)

$$\gamma(t) = \gamma_0 \sin(\omega t) \quad (1-2)$$

$$\sigma(t) = \sigma_0 \sin(\omega t + \delta) \quad (1-3)$$

where $\gamma(t)$ the sinusoidal strain, γ_0 the strain amplitude, ω the angular frequency of oscillation, $\sigma(t)$ the sinusoidal stress, σ_0 the stress amplitude and δ the phase angle. The shear storage modulus $G'(\omega)$ and loss modulus $G''(\omega)$ are given as follows; (Equations 1-4 and 1-5)

$$G'(\omega) = \frac{\sigma_0}{\gamma_0} \cos \delta \quad (1-4)$$

$$G''(\omega) = \frac{\sigma_0}{\gamma_0} \sin \delta \quad (1-5)$$

At low frequencies, it is possible to calculate the zero-shear viscosity η_0 from the loss modulus.

$$\eta_0 = \lim_{\omega \rightarrow 0} \frac{G''(\omega)}{\omega} \quad (1-6)$$

1.2.3 Rouse model

The Rouse model is frequently used to explain the rheological property of an unentangled polymer melt. In this model, chain diffusion is represented by Brownian motion of beads connected by harmonic springs. Each bead is exposed to a random thermal force and a drag force as described by Langevin dynamics. This model was proposed by Rouse in 1953.¹ Later in 1956, Zimm² developed the Rouse model to include hydrodynamic interactions.

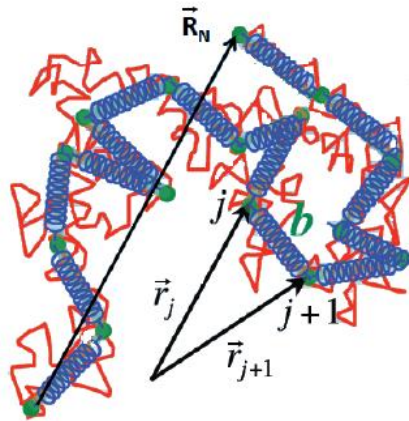


Figure 1-2 Schematic representation of the bead-spring model³ (Vicente, J. D., *Intech*, 2012)

The Rouse model represents a linear chain as a series of beads and springs subjected to entropic forces in a medium with a constant friction. Although this simple approach obviously fails in describing dynamics of a polymer melt in the long time scale, the Rouse model is used to describe the short-time response and thereby it is a common ingredient of all available models and theories. In the past, the validity of the Rouse model has been instigated by means of different experimental techniques and also by molecular dynamics simulations. However, a full and detailed test of the Rouse model is challenging because in unentangled polymer melts the segmental dynamics contribution of different are overlapped each other significantly. This fact, among others, restricts the use of rheological experiments to test accurately the Rouse model for unentangled polymer chains. This is due to the rapid relaxation of a material and the broad spread of the effect of more local molecular mechanisms that affect the modulus at higher frequencies.

1.2.4 Time-Temperature Superposition (TTS)

The time-temperature superposition is used to determine wide range of temperature-dependent linear viscoelastic responses. The elastic moduli of typical amorphous polymers increase with loading rate but decrease at high temperature.⁴ This implies that a master curve at a given temperature can be used as the reference to predict the curves at various temperatures by applying a shift factor.

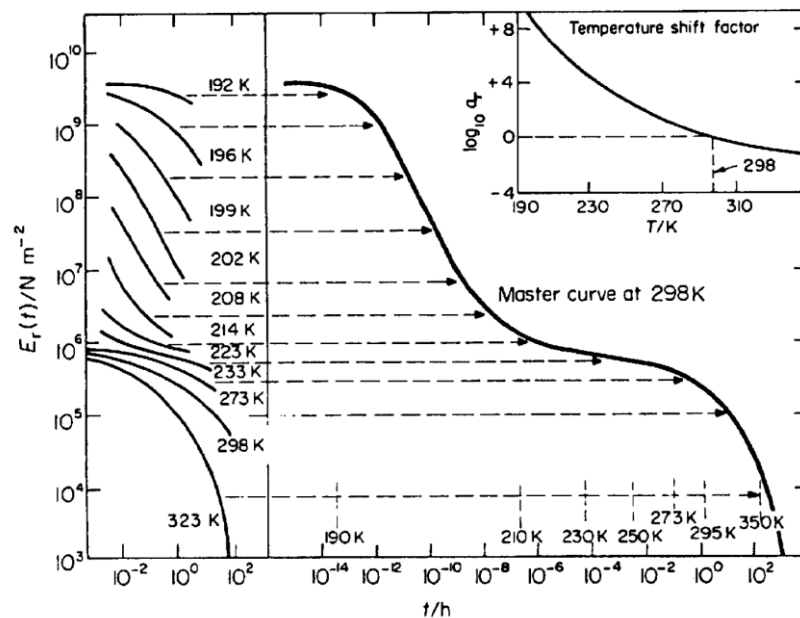


Figure 1-3 A master curve of relaxation modulus for polyisobutylene at 298 K. The classical T_g of this polymer is -70°C .⁵ (Nielsen, L. E., *Mechanical properties of polymers*, 1962)

The empirical relationship introduced independently by Williams, Landel, and Ferry⁶, combined with the principle of time-temperature superposition, can account for variations in the zero-shear viscosity η_0 of an amorphous polymer as a function of temperature. The WLF model expresses the shift factor. Williams, Landel and Ferry proposed the following relationship for a_T :

$$\log a_T = -\frac{C_1(T - T_r)}{C_2 + (T - T_r)} \quad (1-7)$$

where C_1 (dimensionless) and C_2 (absolute temperature) are positive constants that depend on the reference temperature.

This equation is applicable in the wide temperature range as shown in Figure 1-3. When the ambient temperature is much higher than the glass transition temperature T_g , the Arrhenius type equation is also applicable to express the shift factor.

$$a_T = \exp\left(\frac{\Delta E}{RT}\right) \quad (1-8)$$

where ΔE is the activation energy and R is the universal gas constant.

1.2.5 Stress relaxation

The relaxation modulus $G(t)$ is defined by the relaxation stress divided by the strain in the linear region, which expresses the decay of the mechanical response after a step strain. It has equivalent information to the oscillatory response $G^*(\omega)$; one is obtained by the Fourier transform of the other.⁷ A schematic diagram of the stress relaxation for a typical viscoelastic body is shown in Figures 1-4(a) and (b) in linear and logarithmic scales, respectively.⁸

The long time response in $G(t)$ corresponds to the low frequency response in $G^*(\omega)$, whereas the initial short time response of $G(t)$ contains the same information as the high frequency response of $G^*(\omega)$. In short times, a polymeric substance shows a glassy behavior, which goes to the rubbery plateau region (seen clearly in the logarithmic scale in Figure 1-4) and finally to the terminal region. Since $G(t)$ is a kind of an elastic modulus, the response can be understood as being highly elastic in a short time.

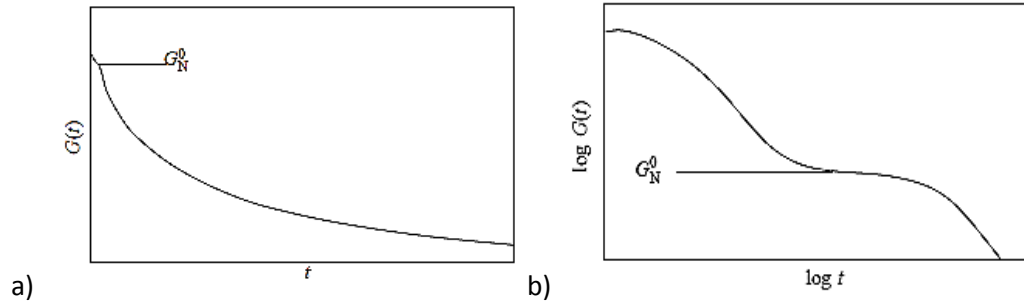


Figure 1-4 Relaxation modulus after a step strain; (a) linear scale and (b) logarithmic scale⁹ (Sunthar, P., *Rheology of complex fluids*, 2010)

The exact relations between $G(t)$ and $G^*(\omega)$ are shown in the following equations. In the case of the transformation from $G(t)$ to $G^*(\omega)$, equations (1-9) and (1-10) are employed.

$$G'(\omega) = \omega \int_0^{\infty} G(t) \sin \omega t dt \quad (1-9)$$

$$G''(\omega) = \omega \int_0^{\infty} G(t) \cos \omega t dt \quad (1-10)$$

Similarly, $G(t)$ is calculated as follows,

$$G(t) = \frac{2}{\pi} \int_0^{\infty} G'(\omega) \frac{\sin \omega t}{\omega} d\omega \quad (1-11)$$

$$G(t) = \frac{2}{\pi} \int_0^{\infty} G''(\omega) \frac{\cos \omega t}{\omega} d\omega \quad (1-12)$$

1.3 Rheology properties of amorphous polymers

Amorphous polymers exhibit widely different types of mechanical properties which depend on temperature and deformation rate. While the structure of crystalline polymers is taken to be regular or ordered to some degree, that of amorphous polymers is basically disorder. At low temperatures, amorphous polymers are glassy, hard, and brittle. Amorphous polymers in the glassy state are called amorphous solids. As the temperature is raised, they go through the glass-to-rubber transition. The glass transition temperature T_g is defined as the temperature at which the polymer softens because of the onset of long-range coordinated molecular motion. Above T_g , cross-linked amorphous polymers exhibit rubber elasticity, for example vulcanized rubbers. Linear amorphous polymers exhibit flow with high viscosity. Polymers such as polystyrene or poly(methyl methacrylate) at room temperature are glassy, taking months or years for significant creep or flow.

1.3.1 Four regions of polymers

Rheological four regions along the time or temperature are observed for most amorphous polymers. For all materials, when modulus is plotted against absolute temperature, a curve is obtained with four characteristic regions. These are glassy region, transition region, rubbery region and flow region.

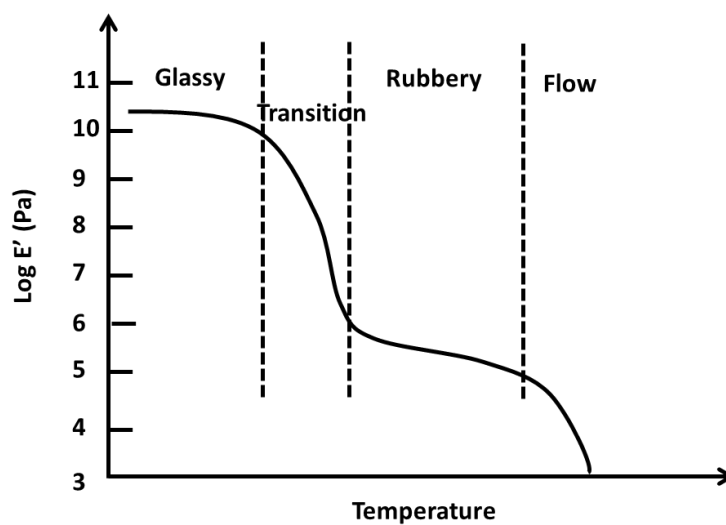


Figure 1-5 Rheological four regions of an amorphous polymer

1.3.2 Glassy Region

In the foregoing, the glassy state exhibits high resistance toward deformation. The glassy modulus of polymers starts with a consideration of the carbon–carbon bonding force fields adopted for the explanation of vibrational frequencies.¹² The glassy modulus is 1-10 GPa. For example, the modulus of polystyrene is 3.3 GPa, poly(methyl methacrylate) is 3.5 GPa and poly(ethyl methacrylate) is 1.7 GPa.¹³

The higher order transitions are attributed to minor motions and can be seen by dynamic mechanical analysis (DMA). The strength of these transitions is related to how

strongly a polymer responds to those processes. These sub- T_g transitions are associated with the materials properties in the glassy state. In paints, for example, peel strength (adhesion) can be estimated from the strength and frequency dependence of the subambient beta transition.¹⁴

1.3.3 Transition region

The glass to rubber transition represents the onset of the Brownian motion, in which all motion between entanglement couplings start to be allowed. Further, the free volume increases rapidly with increasing the temperature, leading to a large scale motion with keeping the entanglement couplings. This transition is usually called a transition for an amorphous polymer, various physical properties are drastically changed at T_g for many polymers. The modulus of this region, 10^6 - 10^{10} Pa, is strongly dependent on temperature. Typically, the modulus drops a factor of about 1000 in a narrow temperature range, e.g., 20- 30 °C. The behavior of polymers in this region is described as leathery, although a few degrees of temperature change will obviously affect the stiffness of a leather. While only 1 to 4 chain atoms are involved in motions below the glass transition temperature, a number of chain atoms move in a coordinated manner in the transition region.¹⁵ The maximum number of chain atoms is equivalent to the entanglement molecular weight.

As the frequency becomes higher, the polymer chains need more high energy to respond in the shorter time scales (Figure 1-6.). The molecular relaxations can only occur at higher temperatures. In general, as the frequency increases, there will be a broadening of $\tan \delta$ peak, and a decrease in the slope of the storage modulus curve in the transition region. T_g increases with increasing the frequency; i.e., time and temperature are interchangeable.

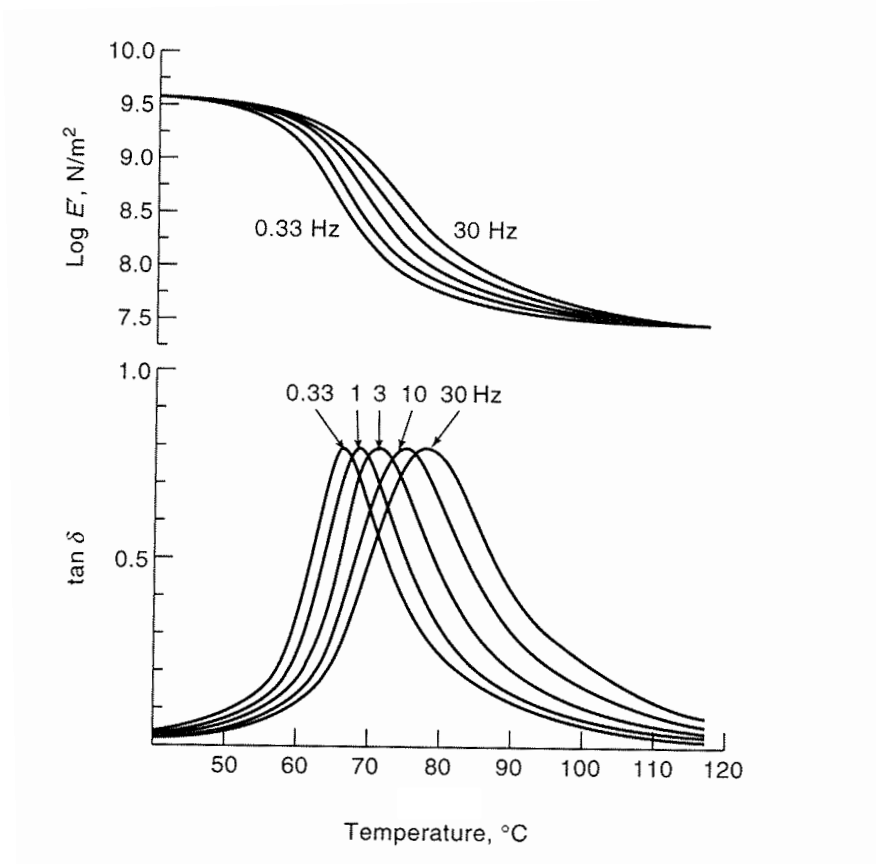


Figure 1-6 Temperature dependent of tensile storage modulus and loss tangent $\tan \delta$ at different measurement frequencies¹⁶ (Schoff, C. K., rheological measurements, 2011)

It is well known that T_g of a polymer depends on the molecular weight. One of the mostly used equations to express this relation was proposed by Fox and Flory:¹⁷

$$T_g = T_g^0 - \frac{c}{M} \quad (1-13)$$

where T_g^0 is the glass transition temperature for an ideal chain with infinite molecular weight in Kelvin scale and c is a constant that related to the free volume of the polymer contribute by chain ends. As M increases, T_g raises (Figure 1-7). This is because the longer chains of a polymer have few chain ends. Polymer chain ends act as hinder for the local

configuration packing and promote free volume, since the intra-molecular covalent bonding is shorter than the inter-molecular interaction of the chain end.

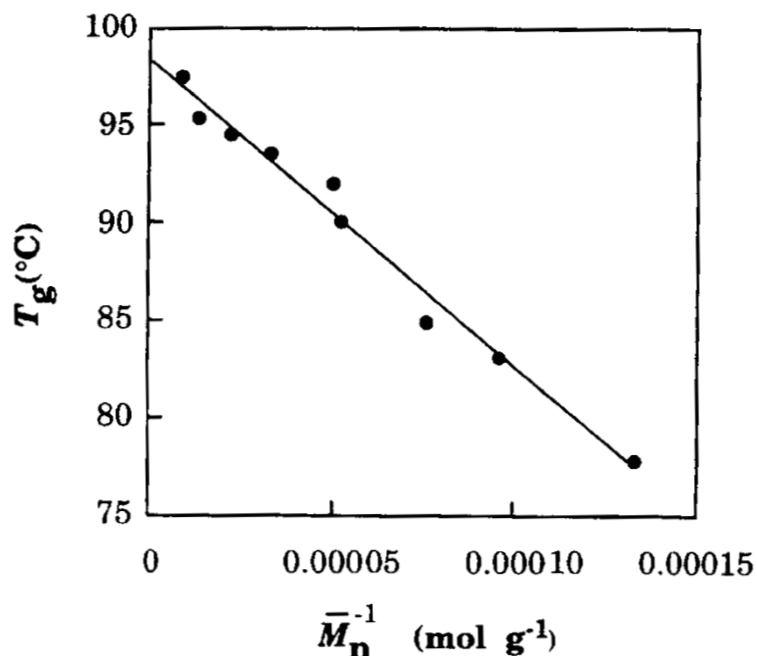


Figure 1-7 Relation between number-average molecular weight and T_g of monodispersed polystyrene¹⁷ (Gedde, U.W., the glassy amorphous state, 1999).

A polymer's ability to show rubber-like behavior is affected by the interaction with its surroundings, e.g., interface. The extamobility is afforded to polymer chains by a relaxation of constraints at a "free" surface which may reduce T_g . There could be a segregation of chain ends to the surface and a consequent reduction in packing density. Near the free surface, therefore, the chain mobility is considered to be more pronounced than that in the bulk. In the center of a film, the chain mobility is considered equivalent to that in the bulk polymer. At the solid interface, the mobility is restricted relative to the bulk polymer. For example, the relation between T_g and the film thickness has been

extensively investigated using polystyrene (PS) films (Figure 1-8).^{18,19} In most cases, there is an apparent depression in T_g with decreasing the film thickness. As seen in Figure 1-8, these are described very well by a linear function of thickness by Equation 1-14.

$$T_g(h) = \begin{cases} T_g(bulk) \left(1 - \frac{(h_0 - h)}{\zeta}\right) & , h < h_0 \\ T_g(bulk) & , h \geq h_0 \end{cases} \quad (1-14)$$

where h is the film thicknesses, h_0 is the threshold value (620 Å) and ζ is 2130 ± 170 Å.

Confinement effects typically onset at a thickness of 60 nm in PS,¹⁸ although this value is reported to depend on parameters such as molecular weight^{20,21} (Figure 1-9) and chain stiffness. Such behavior has been related to an enhanced free volume (lower T_g) provided at the polymer-air interface coupled with relatively weak polymer-substrate interactions.

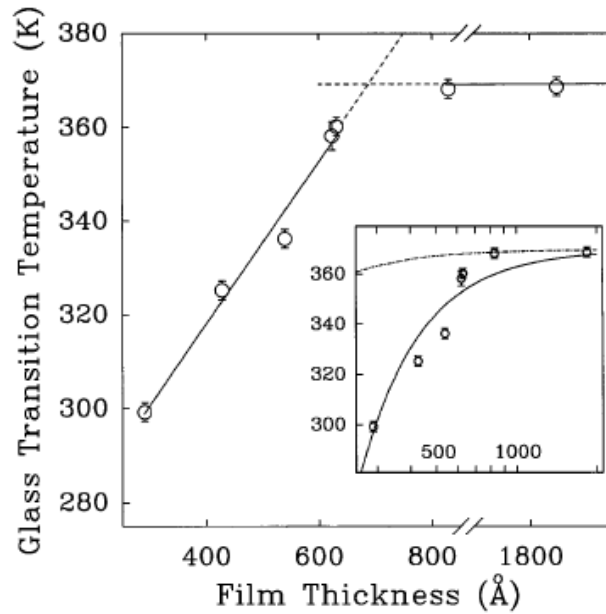


Figure 1-8 Glass transition temperature T_g as a function of film thickness for PS films¹⁸ (Forrest, J. A., *Phys Rev Lett*, 1996)

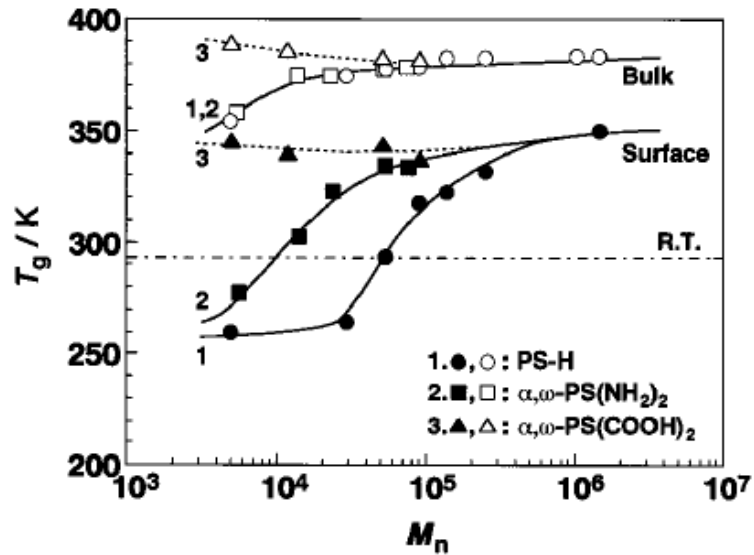


Figure 1-9 M_n dependences of T_g^s and T_g^b for the PS films with various chain end groups based on scanning viscoelasticity microscopy and DSC measurements. The filled and open symbols denote T_g^s and T_g^b , respectively.²¹ (Satomi, N., *Macromolecules*, 2001)

In case of an amorphous polymer, the entanglements act as a chemical crosslink points, but the crosslink points do not relax or become ineffective at high temperatures because of permanent crosslinkages (Figure 1-10). When the crosslink density increases, molecular motion is more restricted, and thus T_g is increased.

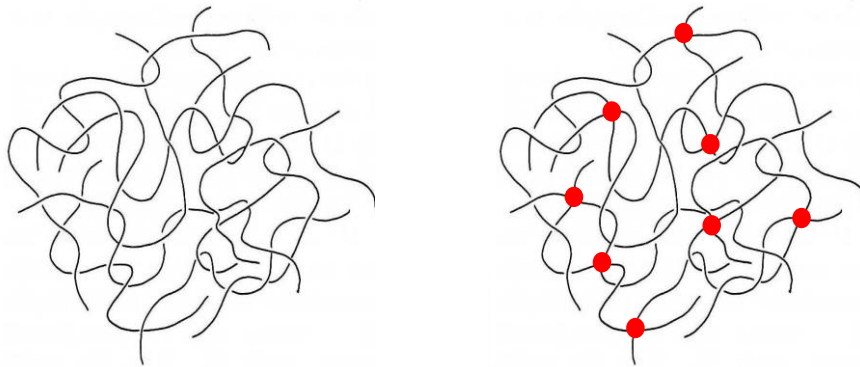


Figure 1-10 Schematic representation showing linear and network polymers

Moreover, the transition region becomes broad due to the heterogeneity in the molecular weight between crosslinks. Widely spaced crosslinks produce only slight restrictions on molecular motions. Consequently, T_g tends to be close to that of the uncrosslinked polymer.



1.3.4 Rubbery region

After the sharp drop of the modulus at T_g , it becomes almost a constant in the rubbery region with typical values of 10^5 - 10^6 Pa of $G(\omega)$ or $G(t)$. The molecules can change their shape between the entanglement couplings by Brownian motion. In this region, the modulus decreases slowly. The rubbery plateau modulus (G_N^0) is the most important parameter in this region.

The length of the rubbery region is governed primarily by the entanglement points per a molecule, i.e., molecular weight divided by the entanglement molecular weight.

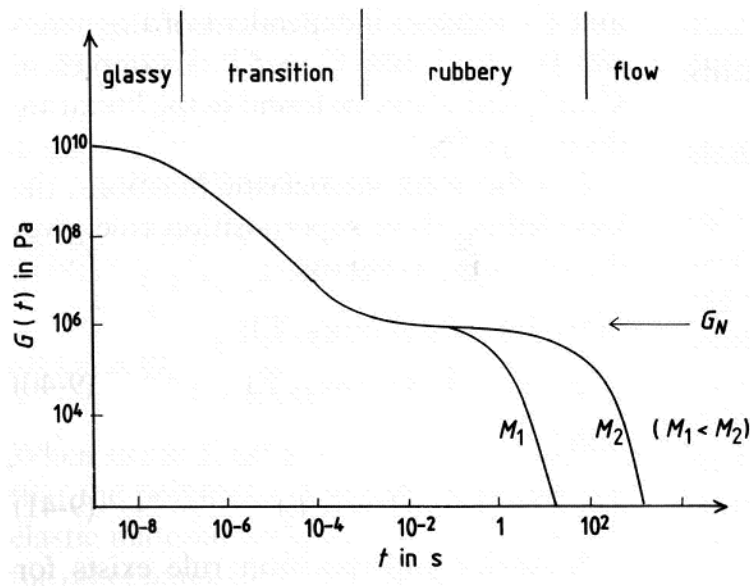


Figure 1-12 Effect of molecular weight on the length of rubbery region ²²

(Cahn, R. W., structure and properties of polymers, 1993)

The measurement of rubbery plateau modulus is not easy, especially for a polymer with broad molecular weight distribution. Generally, G_N^0 can be determined by measuring linear viscoelastic properties in oscillatory shear experiments (dynamic moduli). There are various semi-empirical methods to predict the value of G_N^0 from the linear viscoelastic relaxation spectrum.¹⁰

Figure 1-13 clearly shows a quasi-plateau in the storage modulus *vs* angular frequency curve. The storage modulus G' is flatter and loss modulus G'' peak is more prominent for the sample. Nevertheless, G' is never perfectly flat nor is the G'' peak fully resolved for even extremely high molecular weight with narrow distributions. There is no frequency at which a true plateau can be measured at finite molecular weight due to the overlap of different relaxation modes.^{23,24} The rubbery plateau modulus can be calculated from the value of G' at the frequency ω where G'' reaches a minimum by Equation 1-14.^{10, 25} A similar integration can be performed over the appropriate maximum in G'' . The convention is that the plateau modulus G_N^0 be determined by numerical integration over the terminal relaxation peak of G'' , Equation 1-15.

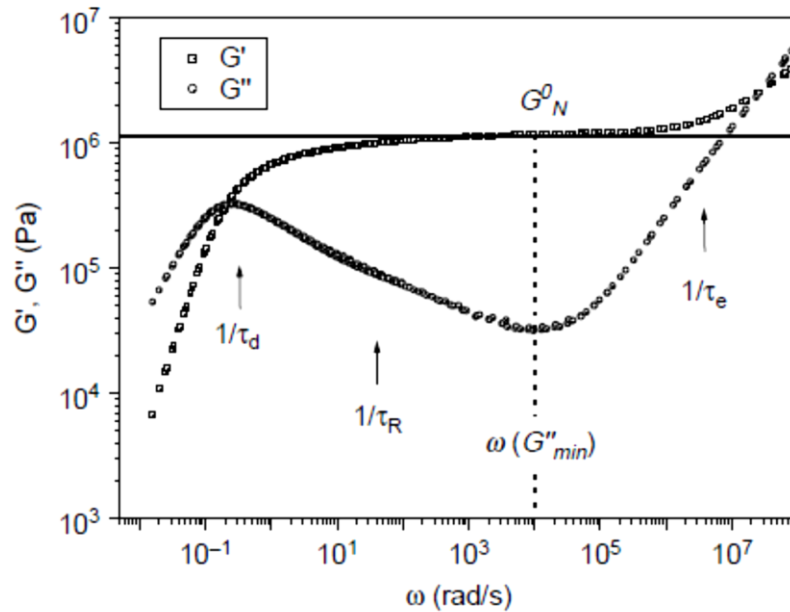


Figure 1-13 Master curves of the storage and loss moduli for a monodisperse for polybutadiene with $M_w = 410,000$.²⁶ (Wang, S., *Macromolecules*, 2003)

For polydisperse polymers, it is more difficult to completely separate the terminal zone from the high frequency. Since the terminal relaxation spectrum is broad for polydisperse system. Therefore, G_N^0 is calculated by taking twice the peak area of up to frequency of a maximum as shown in Equation 1-15. This equation can be used as a replacement in case of insufficient data at high frequencies.

$$G_N^0 = \frac{2}{\pi} \int_{-\infty}^a G'' d \ln \omega = \frac{4}{\pi} \int_{-\infty}^{\frac{a}{2}} G'' d \ln \omega \quad (1-15)$$

The rubbery plateau modulus is related to M_e by Equation (1-13). The plateau modulus is proportional to the number of crosslink points and thus the inverse of the chain length between entanglements. The molecular weight between entanglement couplings, M_e , can be evaluated when the rubbery plateau G_N^0 modulus is identified,^{10,11} using Equation 1-16.

$$M_e = \frac{\rho RT}{G_N^0} \quad (1-16)$$

Effect of crosslinking on the dynamic mechanical properties is shown in Figure 1-14. The modulus in a plateau region increases with increasing the crosslink density.

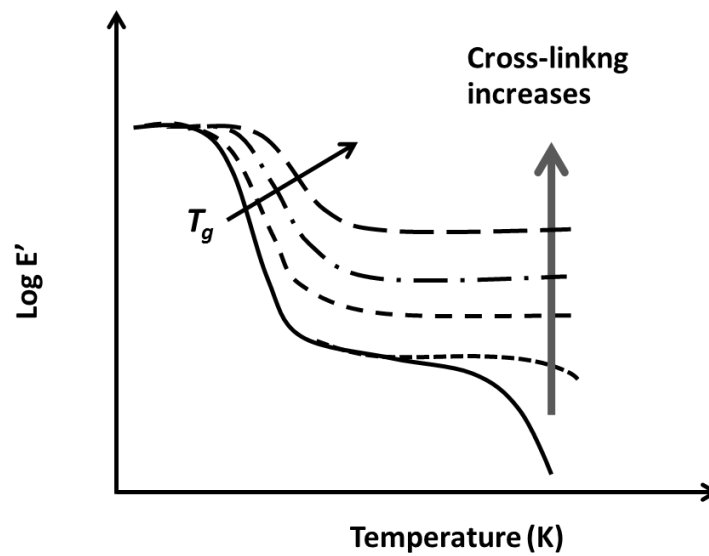


Figure 1-14 Effect of crosslinking on dynamic mechanical properties.

1.3.5 Flow region

At higher temperatures, the flow region is observed, where the translation motion becomes possible. A polymer flows readily, often behaving like molasses. The increased energy allotted to the chains permits them to reptate out through entanglements rapidly. This region is also called the terminal region. It must be mentioned that viscosity is related with the relaxation time.

For semi-crystalline polymers, the modulus depends on the degree of crystallinity. The amorphous portions go through the glass transition, but the crystalline portion remains hard. Only beyond the melting point T_m , the terminal region is detected.

As the length of rubbery region is affected by molecular weight, the flowability is also dependent on the molecular weight of a polymer (Figure 1-15).²⁷

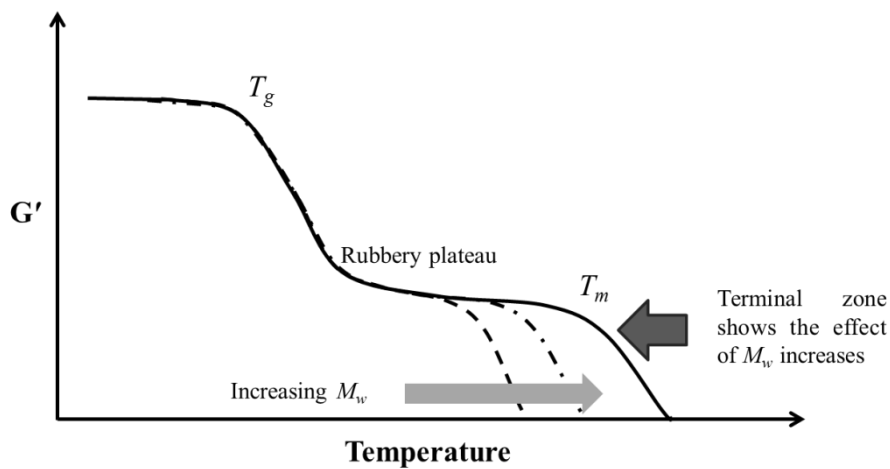


Figure 1-15 Effect of molecular weight on the terminal zone or melting region²⁷ (Turi, E., thermal characterization of polymeric materials, 1987)

1.4 Objectives of this research

Although the rheological properties and processability at extrusion have not been studied in detail for PVB because of its restricted applications, the strong demand for material recycling requires PVB to be available for extrusion. Moreover, intense attention has been paid for PVB because of the amphiphilic properties, which leads to a new material design of polymer blends and composites. The amphiphilic nature is also attractive for material recycling. Considering the current situation of PVB, the aim of this research is to clarify the basic rheological properties and processabilities. The rheological characterization with the evaluation of extrusion properties using a capillary rheometer is carried out for both linear and non-linear rheological measurements. Moreover, it is found that PVB exhibits self-healing property during this research, which is significantly interesting and needs to be clarified the mechanism for the industrial application. Therefore, the self-healing property is demonstrated and investigated in detail.

References

1. Rouse, P. E., A Theory of the Linear Viscoelastic Properties of Dilute Solutions of Coiling Polymers. *J Chem Phys* **1953**, 21 (7), 1272-1280.
2. Zimm, B. H., Dynamics of Polymer Molecules in Dilute Solution: Viscoelasticity, Flow Birefringence and Dielectric Loss. *J Chem Phys* **1956**, 24 (2), 269-278.
3. Vicente, J. D., Rheology. *Intech* **2012**, 350 page.
4. Li, R., Time-temperature Superposition Method for Glass Transition Temperature of Plastic Materials. *Mater Sci Eng, A* **2000**, 278 (1–2), 36-45.
5. Nielsen, L. E., Mechanical Properties of Polymers. Van Nostrand Reinhold **1962**.
6. Williams, M. L.; Landel, R. F.; Ferry, J. D., The Temperature Dependence of Relaxation Mechanisms in Amorphous Polymers and Other Glass-forming Liquids. *J Am Chem Soc* **1955**, 77 (14), 3701-3707.
7. Macosko, C., Rheology: *Principles, Measurements, and Applications*. VCH, New York **1994**.
8. Dealy, J.; Larson, R., Structure and Rheology of Molten Polymers-from Structure to Flow Behavior and Back Again. Hanser, Munich **2006**.
9. Sunthar, P., Polymer Rheology. In *Rheology of Complex Fluids*, Krishnan, J. M.; Deshpande, A. P.; Kumar, P. B. S., Eds. Springer New York **2010**; pp 171-191.
10. Ferry, J. D., Viscoelastic Properties of Polymers. John Wiley & Sons **1980**.
11. Graessley, W., The Entanglement Concept in Polymer Rheology. In *The Entanglement Concept in Polymer Rheology*. Springer Berlin Heidelberg **1974**; Vol. 16, pp 1-179.

12. Shimanouchi, T.; Asahina, M.; Enomoto, S., Elastic Moduli of Oriented Polymers. I. The Simple Helix, Polyethylene, Polytetrafluoroethylene, and a General Formula. *J Polym Sci* **1962**, *59* (167), 93-100.
13. Torres, J. M.; Stafford, C. M.; Vogt, B. D., Elastic Modulus of Amorphous Polymer Thin Films: Relationship to the Glass Transition Temperature. *ACS Nano* **2009**, *3* (9), 2677-2685.
14. Meesiri, W.; Menczel, J.; Gaur, U.; Wunderlich, B., Phase Transitions in Mesophase Macromolecules. III. The Transitions in Poly(ethylene terephthalate-co-p-oxybenzoate). *J Polym Sci: Polym Phys Ed* **1982**, *20* (4), 719-728.
15. Ueberreiter, K.; Kanig, G., Second-Order Transitions and Mesh Distribution Functions of Cross-Linked Polystyrenes. *J Chem Phys* **1950**, *18* (4), 399-406.
16. Schoff, C. K.; Kamarchik, P.; , Rheological Measurements. In *Properties and Behavior of Polymers*. Wiley, New York **2011**; 2.
17. Gedde, U., The Glassy Amorphous State. In *Polymer Physics*. Springer Netherlands **1999**; pp 77-98.
18. Forrest, J. A.; Dalnoki-Veress, K.; Stevens, J. R.; Dutcher, J. R., Effect of Free Surfaces on the Glass Transition Temperature of Thin Polymer Films. *Phys Rev Lett* **1996**, *77* (10), 2002-2005.
19. Fryer, D. S.; Peters, R. D.; Kim, E. J.; Tomaszewski, J. E.; de Pablo, J. J.; Nealey, P. F.; White, C. C.; Wu, W.-l., Dependence of the Glass Transition Temperature of Polymer Films on Interfacial Energy and Thickness. *Macromolecules* **2001**, *34* (16), 5627-5634.

20. Tanaka, K.; Kajiyama, T.; Takahara, A.; Tasaki, S., A Novel Method to Examine Surface Composition in Mixtures of Chemically Identical Two Polymers with Different Molecular Weights. *Macromolecules* **2002**, *35* (12), 4702-4706.
21. Satomi, N.; Tanaka, K.; Takahara, A.; Kajiyama, T.; Ishizone, T.; Nakahama, S., Surface Molecular Motion of Monodisperse α,ω -Diamino-Terminated and α,ω -Dicarboxy-Terminated Polystyrenes. *Macromolecules* **2001**, *34* (25), 8761-8767.
22. Cahn, R. W.; Haasen, P.; Kramer, E. J., Structure and Properties of Polymers. Wiley-VCH **1993**; Vol. 12.
23. McLeish, T. C. B., Tube Theory of Entangled Polymer Dynamics. *Advances in Physics* **2002**, *51* (6), 1379-1527.
24. Rubinstein, M.; Colby, R., Polymers Physics. Oxford **2003**.
25. Larson, R.; Sridhar, T.; Leal, L.; McKinley, G.; Likhtman, A.; McLeish, T., Definitions of Entanglement Spacing and Time Constants in the Tube Model. *J Rheol (1978-present)* **2003**, *47* (3), 809-818.
26. Wang, S.; Wang, S.-Q.; Halasa, A.; Hsu, W.-L., Relaxation Dynamics in Mixtures of Long and Short Chains: Tube Dilation and Impeded Curvilinear Diffusion. *Macromolecules* **2003**, *36* (14), 5355-5371.
27. Turi, E., Thermal Characterization of Polymeric Materials. Elsevier **1981**.
28. Yuan, Y.; Yin, T.; Rong, M.; Zhang, M., Self Healing in Polymers and Polymer Composites. Concepts, Realization and Outlook: a review. *Express Polym Lett* **2008**, *2* (4), 238-250.

29. Jud, K.; Kausch, H.; Williams, J., Fracture Mechanics Studies of Crack Healing and Welding of Polymers. *J Mater Sci* **1981**, *16* (1), 204-210.
30. Varghese, S.; Lele, A.; Mashelkar, R., Metal-ion-mediated Healing of Gels. *J Polym Sci, Part A: Polym Chem* **2006**, *44* (1), 666-670.
31. Murphy, E. B.; Wudl, F., The World of Smart Healable Materials. *Prog Polym Sci* **2010**, *35* (1-2), 223-251.

Chapter 2

Rheological Properties of Poly(Vinyl Butyral)

2.1 Introduction

2.1.1 Poly(vinyl butyral)

Poly(vinyl butyral), a derivative of poly(vinyl alcohol), is widely used in laminated safety glasses, paints, adhesives and binder for ceramics, because of the good adhesive strength to glasses and metals. At present, the largest application of PVB is an adhesive or interlayer in the laminated safety glasses for automotive and aircraft uses. As compared with cellulose acetate which was used for the same application previously, a safety glass made from PVB has superior adhesion. Furthermore, it is tough, stable on exposure to sunlight, clear, and insensitive to moisture.

Poly(vinyl butyral) is normally synthesized by reacting poly(vinyl alcohol) with butyraldehyde with presence of an acid catalyst (Figure 2-1). This polymer usually contains a small amount of vinyl acetate because poly(vinyl alcohol) is prepared from poly(vinyl acetate).

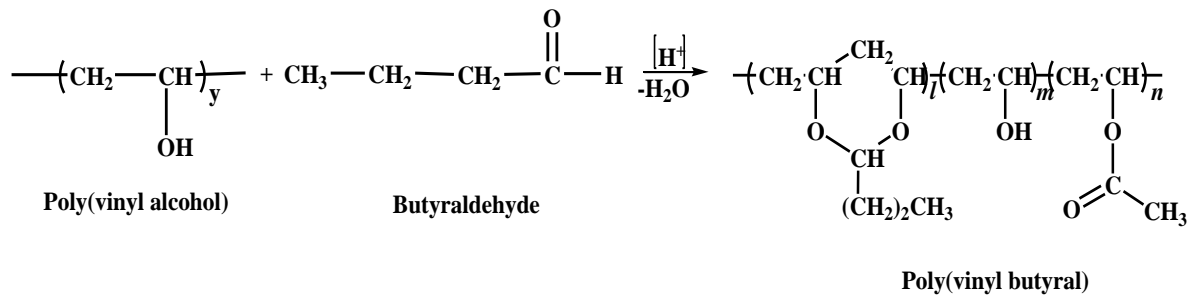


Figure 2-1 Synthesis of poly(vinyl butyral)

Although its common name is “poly(vinyl butyral)”, it is actually a random copolymer composed of vinyl butyral and vinyl alcohol, or a random terpolymer of vinyl butyral, vinyl alcohol, and vinyl acetate, as shown in Figure 2-2. In this thesis, this polymer is represented as “PVB” following the conventional way, although it is not a homopolymer. The details in the chemical composition are mentioned in the experimental part.

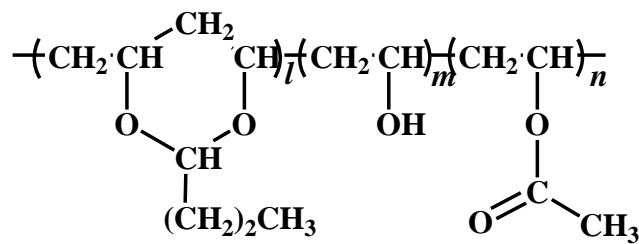


Figure 2-2 Chemical structure of PVB

The molecular characteristics of PVB have been studied mainly by dilute solution properties such as size exclusion chromatography^{1,2} and nuclear magnetic resonance^{3,4} and thermal analysis.^{4,5} According to them, the random distribution of the monomer units in PVB results in a glassy polymer with no discernible crystallinity except the polymers having high vinyl alcohol content (more than 63.3 wt%).⁴ It was also found that the glass

transition temperature T_g increases and the thermal stability decreases, as increasing the vinyl alcohol content.^{4,5} Furthermore, Morais et al. evaluated the surface tension which is an important property for PVB applications.⁶ Regarding the applications such as adhesive to inorganic glass and ceramics, the hydrophilic nature originated from vinyl alcohol and vinyl acetate parts are responsible for the superior properties. Furthermore, it is known that the surface tension decreases linearly with increasing the ambient temperature because of the chemical degradation. Blends with other polymeric materials have been also studied. Because PVB contains both hydrophilic and hydrophobic parts in the structure, it can be compatible with both hydrophilic and hydrophobic polymers. In fact, several researchers have reported on the miscibility and/or compatibility with various polymers such as polyamide,^{7,8} poly(ϵ -caprolactone),⁹⁻¹¹ poly(butylene terephthalate),¹² polyurethane,¹³ poly(ethylene glycol),¹⁴ poly(vinyl chloride),¹⁵ poly(methyl methacrylate),¹⁶ cellulose acetate,¹⁷ and poly(3-hydroxybutyrate).¹⁸ In particular, advanced studies on the miscibility considering the effect of copolymer composed of immiscible monomers have provided the new concept for material design of polymer blends,^{7,11,12,16,18,19} in which PVB is an appropriate candidate for the new type of blends.

As compared to the studies on the blends with other polymers, the rheological properties and mechanical properties of a single polymer have not been studied so much at the best of my knowledge. One of the reasons will be the restricted applications of PVB as mentioned before. However, due to the increase in the attention to the environment, PVB collected from laminated glasses is used as a recycled resin recently, especially in the automobile industry.²⁰ Furthermore, it is inevitable to understand the rheological properties for the material design of a self-healing polymer using molecular interdiffusion

as the repairing mechanism, which is a topic in Chapter 3. Therefore, further studies on the rheological properties are required. Of course, the study on the processability is considerably important to widen the application of PVB including the recycled one.

2.1.2 Poly(vinyl acetate) (PVAc)

Poly(vinyl acetate) (PVAc) is one of the most widely used vinyl ester polymers. It is usually used as the precursor or starting material for other polymers that cannot be synthesized by direct polymerization from monomeric species. The typical polymers are poly(vinyl alcohol) and poly(vinyl acetal), because their starting monomer is unstable. The most important application of PVAc is the starting material for poly(vinyl butyral) and poly(vinyl formal). Only atactic or amorphous poly(vinyl acetate) is currently commercially available. The glass transition temperature, T_g , of PVAc is 29 °C. Consequently, the polymer becomes sticky at temperatures slightly above the ambient. Therefore, it is used for the ingredient in chewing gums. Its adhesive strength is dictated by its water sensitivity. As mentioned above, a major use of poly(vinyl acetate) is in the production of poly(vinyl alcohol) (Figure 2-3), which is itself the starting material for poly(vinyl butyral) and poly(vinyl formal).

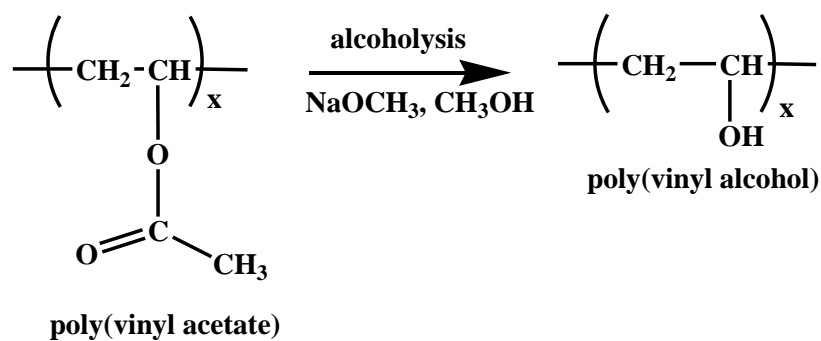


Figure 2-3 Synthesis of poly(vinyl alcohol)

2.1.3 Poly(vinyl alcohol) (PVA)

Vinyl alcohol is known to be unstable; it is isomeric with acetaldehyde. Therefore, poly(vinyl alcohol) (PVA) is obtained indirectly by the alcoholysis of poly(vinyl acetate) in concentrated methanol or ethanol. The reaction is carried out in the presence of acid or base catalyst. PVA has atactic chain structure that exhibits crystallinity. The small size of the OH groups permits them to fit into a crystal lattice. Various PVA grades are available, which have different molecular weight and the degree of hydrolysis that is determined by the solubility in water.

One of the famous applications of PVA is a polarizing film, in which iodine molecules are doped. Moreover, it is used as a stabilizing agent with its water soluble capacity. PVA is also used in the manufacture of poly(vinyl butyral) and poly(vinyl formal). Moreover, it has high tensile strength and flexibility, as well as high oxygen and aroma barrier properties. However, these properties are dependent on the humidity; i.e., more water is absorbed at high humidity conditions. The water, which acts as a plasticizer, will then reduce its tensile strength, but increase its elongation at break and tear strength

2.1.4 Processability

The processability of polymeric materials is characterized by various methods or techniques. Extrusion, injection-molding, and calendaring are well-known as used in industry. In the case of extrusion, various products can be prepared by changing the shape of the die, such as pipes, films, sheets, and bottles. Blow-molding, T-die film processing, tubular-blown film processing, extrusion-casting, wire-coating and conventional extrusion such as pipes and tubes are included in the extrusion processing.

At extrusion processing, high out-put rate operation is always required as similar to cycle time at injection-molding. Although a polymer melt behaves liquid at low shear rate, it behaves like solid at high shear rate. Then, flow instability occurs which limits the production speed. Therefore, understanding the rheological properties of a polymer melt is required to perform the processing operation at a high out-put rate. Moreover, it is also important to control the mechanical properties in the solid state, because rheological properties in the molten state decide the molecular orientation and higher-order structure.

2.1.5 Capillary extrusion

The simplest method to evaluate the extrusion processability is the capillary extrusion using a pressure-driven capillary-type rheometer as shown in Figure 2-4. The capillary flow experiment provides the information on the processability at extrusion, i.e., the appearance of extrudates, with shear viscosity. Furthermore, the method is good at evaluating the shear viscosity at high shear rates as compared with a cone-and-plate rheometer. A polymer solid is fed into the barrel with temperature controller, heated to a fluid state, and extruded through a die. The extruded strand is then solidified after passing

through the die.

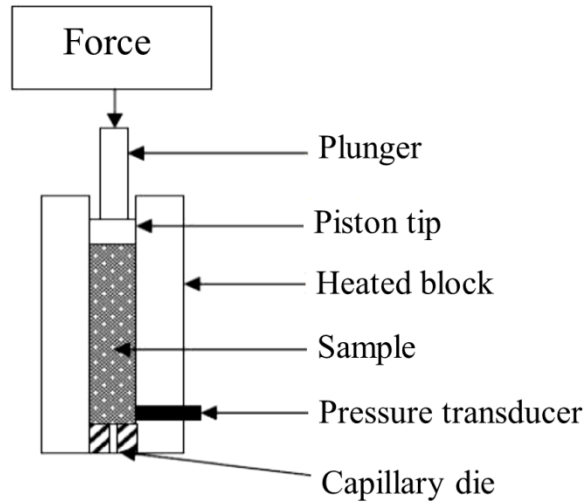


Figure 2-4 Schematic diagram for capillary rheometer

Shear viscosity η and shear rate $\dot{\gamma}$ are calculated by the Hagen-poiseuille law as follows;

$$\eta = \frac{\Delta P \pi r_0^4}{8LQ} \quad (2-1)$$

$$\dot{\gamma} = \frac{4Q}{\pi r_0^3} \quad (2-2)$$

where Q is the volume flow rate, ΔP is the pressure and, L and r_0 are the length and radius of a die.

The maximum production speed in industrial extrusion processes are often decided by the onset of flow instability, such as shark skin and gross melt fracture, which can be also evaluated by a capillary rheometer.

2.1.6 Flow instability

The flow instability is defined as unsteady flow, leading to rough surface or irregular shape of products. Because the flow instability decides the production speed, it has to be comprehended in detail for the industrial application.

In general, it has been recognized that the flow instability at extrusion can be classified into two types; i.e., gross melt fracture and shark-skin failure (Figure 2-5).

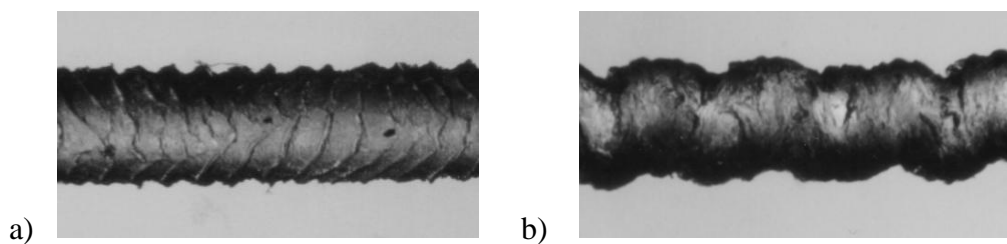


Figure 2-5 Typical flow instabilities for polyolefins; (a) shark-skin failure and (b) gross melt fracture.²¹ (Yamaguchi, M., *Polymer*, 2002)

The gross melt fracture is caused from the instability at die entry, which is often observed for a polymer melt with high elasticity. A melt with high elasticity like a branched polymer shows high elongational viscosity. The elongational flow occurs by the contraction flow at die entry. Once the elongational stress is higher than the critical value, the gross melt fracture occurs. Another one is shark-skin failure, defined as the rough surface on the extrudates. It is often observed for linear polymers when their shear stress at die exit is higher than the critical one.

Figure 2-6 shows the illustration of the onset of flow instability. As increasing the out-put rate at extrusion, both shear stress and elongational stress increase. If the shear stress is higher than the critical value and the elongational stress is lower than the critical one, shark-skin failure decides the maximum out-put rate. In case of PVB, the shark skin

failure is expected to appear at first because of its linear structure.

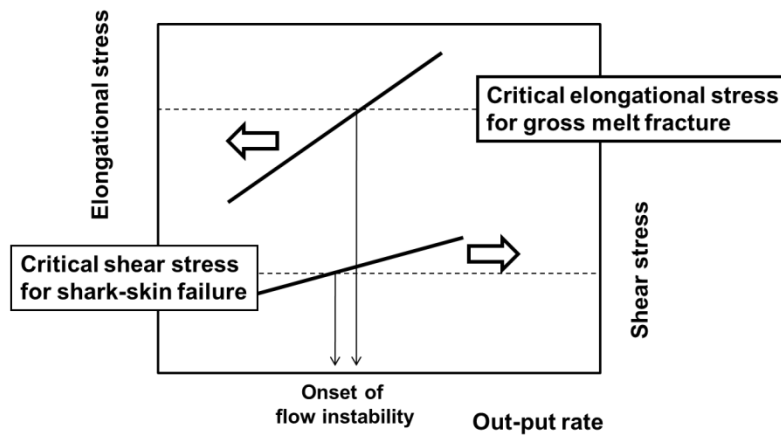


Figure 2-6 Shear and elongational stress plotted against out-put rate²² (Meller, M., *Polym Eng. Sci.*, 2002)

Origin of Shark-skin failure

The origin of shark-skin failure is explained by two mechanisms. One is cohesive failure which is referred to the discontinuous velocity of the polymer surface at the die exit (Figure 2-7). This can be explained as follows; prior to die exit, flow velocity of a polymer melt on the wall v_{wall} is zero, whereas it becomes a constant value V after the die exit. Therefore, the deviation of the flow velocity at the die wall is infinity at the exit. In other word, high level of elongational stress is subjected at surface of the strand. When the elongational stress at the exit is higher than the cohesive stress of a polymer melt, surface on the extrudate becomes rough, i.e., shark-skin failure.

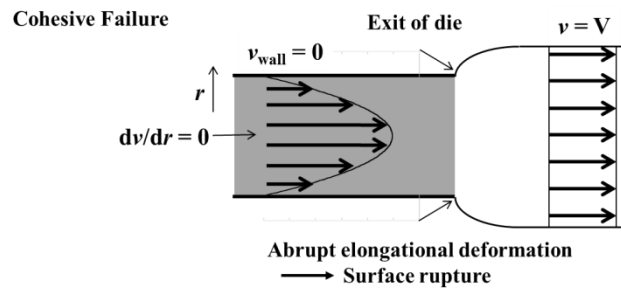


Figure 2-7 Schematic mechanism of cohesive failure

Another one is unsteady slippage which is a kind of adhesive failure between a polymer melt and die wall, as illustrated in Figure 2-8. The detachment of a melt from die surface accompanied with cracks by adhesive failure leads to surface instabilities.²³ Furthermore, Brochard and de Gennes proposed the idea that slippage occurs between a polymer melt and the polymer chains adsorbed on the die wall.²⁴

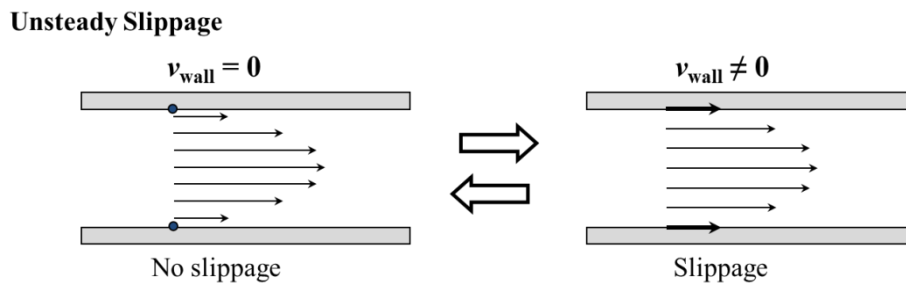


Figure 2-8 Schematic mechanism of unsteady slippage

The critical stresses of the cohesive failure and unsteady slippage have been discussed for a long time. Allal et al. proposed the following relations for the shark-skin failure.^{25, 26}

$$\sigma_c = \frac{1}{2} G_N^0 \frac{N_e}{\sqrt{N_0}} \quad (2-1)$$

$$\sigma_s = \frac{9}{4\pi} G_N^0 C_{ad} \frac{N_e}{\sqrt{N_0}} \quad (2-2)$$

where σ_c is the critical shear stress of cohesive failure, σ_s is the critical shear stress of unsteady slippage, N_e is the number of monomers between entanglements, N_0 is that of monomers per chain and C_{ad} is the fraction of monomers adsorbed on the surface of die wall.

Following the equations, the critical stress is proportional to G_N^0 which is inversely proportional to the average molecular weight between entanglement couplings, M_e , irrespective of the mechanism. Therefore, a polymer having high M_e or low G_N^0 shows both surface rupture and slippage at a low shear stress.

Since G_N^0 is inversely proportional to M_e , the equations can be expressed;

$$\sigma_c = \frac{1}{2} \frac{\rho RT}{M_e} \frac{M / M_e}{\sqrt{M / M_0}} = \frac{1}{2} \rho RT M_0^{0.5} \frac{M^{0.5}}{M_e^2} \quad (2-3)$$

$$\sigma_s = \frac{9}{4\pi} \frac{\rho RT}{M_e} C_{ad} \frac{N_e}{\sqrt{N_0}} = \frac{9}{4\pi} \rho RT C_{ad} M_0^{0.5} \frac{M^{0.5}}{M_e^2} \quad (2-4)$$

where M and M_0 are the molecular weights of a chain and the monomer, respectively.

As seen in the equations, the critical shear stress is also proportional to the molecular weight. A polymer with high molecular weights shows high critical shear stresses.

Finally, Yamaguchi et al. revealed that steady-state shear stress can be expressed by the relaxation time distribution, Deborah number De , and G_N^0 using the Carreau equation:

$$\sigma(\dot{\gamma}) = G_N^0 f^{n-1} De^n \quad (2-5)$$

where f is the ratio of τ_w (weight-average relaxation time) to τ_n (number-average relaxation time), which is a function of the molecular weight distribution.

$$\tau_w \equiv \frac{\int \tau^2 H(\tau) d \ln \tau}{\int \tau H(\tau) d \ln \tau} = \eta_0 J_e^0 \quad (2-6)$$

$$\tau_n \equiv \frac{\int \tau H(\tau) d \ln \tau}{\int H(\tau) d \ln \tau} = \frac{\eta_0}{G_N^0} \quad (2-7)$$

where η_0 is the zero-shear viscosity and J_e^0 is the steady-state shear compliance.

This equation provides the information on processing failures due to the pronounced melt elasticity (high Deborah number) including the shark-skin failure.^{27,28,29,30} When a polymer melt has narrow molecular weight distribution, i.e., small f , Deborah number becomes large at a constant shear stress. As a result, a melt tends to show the shark-skin failure at a low shear rate.

Generally, a polymer having broad molecular weight distribution exhibits high melt elasticity with marked non-Newtonian behavior even in the low shear rate region. Therefore, the processability at some processing operations, such as foaming, blow molding, and T-die extrusion is improved by broadening the molecular weight distribution. Furthermore, high out-put rate operation is possible because the critical shear rate will increase. In contrast, a polymer with narrow molecular weight distribution exhibits high shear stress at processing. In the case of a linear polymer, f is determined by the

molecular weight distribution. Therefore, a polymer having narrow molecular weight distribution possesses small f and large Deborah number, leading to the shark-skin failure easily.

In this chapter, rheological characterization of PVB is carried out by linear viscoelastic measurements as well as the evaluation of extrusion properties using a capillary rheometer. The results obtained in this chapter are used for the material design of a self-healing polymer as discussed in the next chapter.

2.2 Experimental

2.2.1 Materials

Two types of commercially available PVB were used in this study. Both of them are terpolymers composed of vinyl butyral, vinyl alcohol and vinyl acetate at various ratios; PVB 4000-2 is composed of 79:19:2 wt% or 55:42.7:2.3 mol%, respectively, and PVB 4000-4 is composed of 80:20:2 wt% or 57:41:2 mol%, respectively. Both are produced by Denki Kagaku Kogyo, Japan (Denka PVB 4000-2, denoted as PVB1, and 4000-4, as PVB2). The number-, weight-average molecular weights and molecular weight distribution were evaluated by a size exclusion chromatography (Tosoh, Japan, HLC-8020) using chloroform as a solvent; $M_n = 1.1 \times 10^5$, $M_w = 2.2 \times 10^5$ and $DPI = 2.0$ for PVB1 and $M_n = 1.8 \times 10^5$, $M_w = 3.1 \times 10^5$ and $DPI = 1.7$ for PVB2, respectively as a polystyrene standard. Furthermore, absolute molecular weights of PVB2 were evaluated by the simultaneous measurements of multi-angle light scattering (Wyatt Technology, Dawn Heleos) and gel permeation chromatography (Tosoh, HLC-8120GPC) with TSKgel GMHHR-H (Tosoh). Tetrahydrofuran was used as an eluent at a flow rate of 1.0 mL/min

at 40 °C, and the sample concentration was 1.0 mg/mL. The result is shown in Table 2-1.

Table 2-1 Characteristics of PVB used in this work

	Fraction of Monomers			Molecular weights		
	Vinyl butyral	Vinyl alcohol	Vinyl acetate	M_n (10^5 Da)	M_w (10^5 Da)	M_w/M_n
PVB1	79	19	2	*1.1	*2.2	*2.0
PVB2	80	18	2	*1.8 (#0.84)	*3.1 (#1.5)	*1.7 (#1.72)

* polystyrene standard, # absolute molecular weight

2.2.2 Sample Preparation

The samples were compressed into flat sheets by a compression-molding machine (Tester Sangyo, Table-type test-press) at 190 °C under 10 MPa for 3 min. Then, the samples were rapidly cooled down in an ice-water bath. All rheological measurement were performed after vacuum for 1 days.

2.2.3 Measurements

Temperature dependence of oscillatory tensile moduli such as storage modulus E' , loss modulus E'' , and loss tangent $\tan \delta$ was measured at 10 Hz from -10 to 200 °C by a dynamic mechanical analyzer (UBM, E-4000) using rectangular specimens with 5 mm in width and 20 mm in length. The heating rate was 2 °C/min.

Thermal properties were analyzed using a differential scanning calorimeter (Mettler, DSC820) (DSC) under a nitrogen atmosphere (flow rate 75 ml/min). Approximately 10 mg of each sample was encapsulated in a standard aluminum pan. The samples were heated from 25 to 250 °C at a heating rate of 10 °C/min.

X-ray diffraction analysis (XRD) was measured using an X-ray diffractometer (Rigaku, RINT 2500 diffractometer) with Cu K α radiation ($\lambda = 1.542 \text{ \AA}$; 40kV, 30mA). The samples having 300 μm of thickness were mounted and scanned in the range from 0.1 to 50.0 degrees.

Frequency dependence of the oscillatory shear moduli such as storage modulus G' and loss modulus G'' was measured in the temperature range from 100 °C to 250 °C by a rotational-type rheometer (TA Instruments, AR2000) using a parallel plate geometry. The measurements were carried out under a nitrogen atmosphere in order to avoid thermo-oxidative degradation. The time-temperature superposition was applied to the frequency dependence of oscillatory moduli at different temperatures in an attempt to determine the linear viscoelastic properties over a wide range of time scales.

Capillary extrusion was performed by a capillary rheometer (Yasuda Seiki Seisakusyo, 140 SAS-2002) at 190, 220, and 250 °C to evaluate the steady-state shear viscosity and the appearance of extruded strands. The molten polymer was extruded

through a die having the following dimension; 1 mm of the diameter, 10 mm of the length and the entrance angle of 180 °. The Bagley and Rabinowitch corrections were not carried out in this study. The extruded strand was observed by a stereomicroscope (Leica, S6E). Furthermore, the magnified surface images were recorded for some strands using a scanning electron microscope (SEM) (Hitachi, S400) with an acceleration voltage of 20 kV. An ion sputtering machine (Hitachi, E1010) was used to coat non-conducting specimens with Pt/Pd.

Density was measured by a buoyancy method using a chemical balance. Silicone oil (KF-96-100CS, Shin-Etsu, Japan) at 100 °C (900.8 kg/m^3) was used as a liquid.

2.3 Results and discussion

2.3.1 Linear Viscoelastic Properties

Figure 2-9 shows the temperature dependence of dynamic tensile modulus at 10 Hz. As demonstrated by an abrupt drop of the storage modulus E' , the glass transition temperature's T_g 's of PVB1 and PVB2 are found to be located around at 68 °C and 78 °C, respectively. Therefore, the samples behave as a plastic glass at room temperature. Although the origin of the different in T_g between them is not clear, slight difference in the chemical composition may affect T_g .

It should be noted that the rubbery region is observed in the wide temperature range with a relatively high modulus. In general, conventional amorphous plastics do not show such a wide temperature range of rubbery region without crystalline parts.

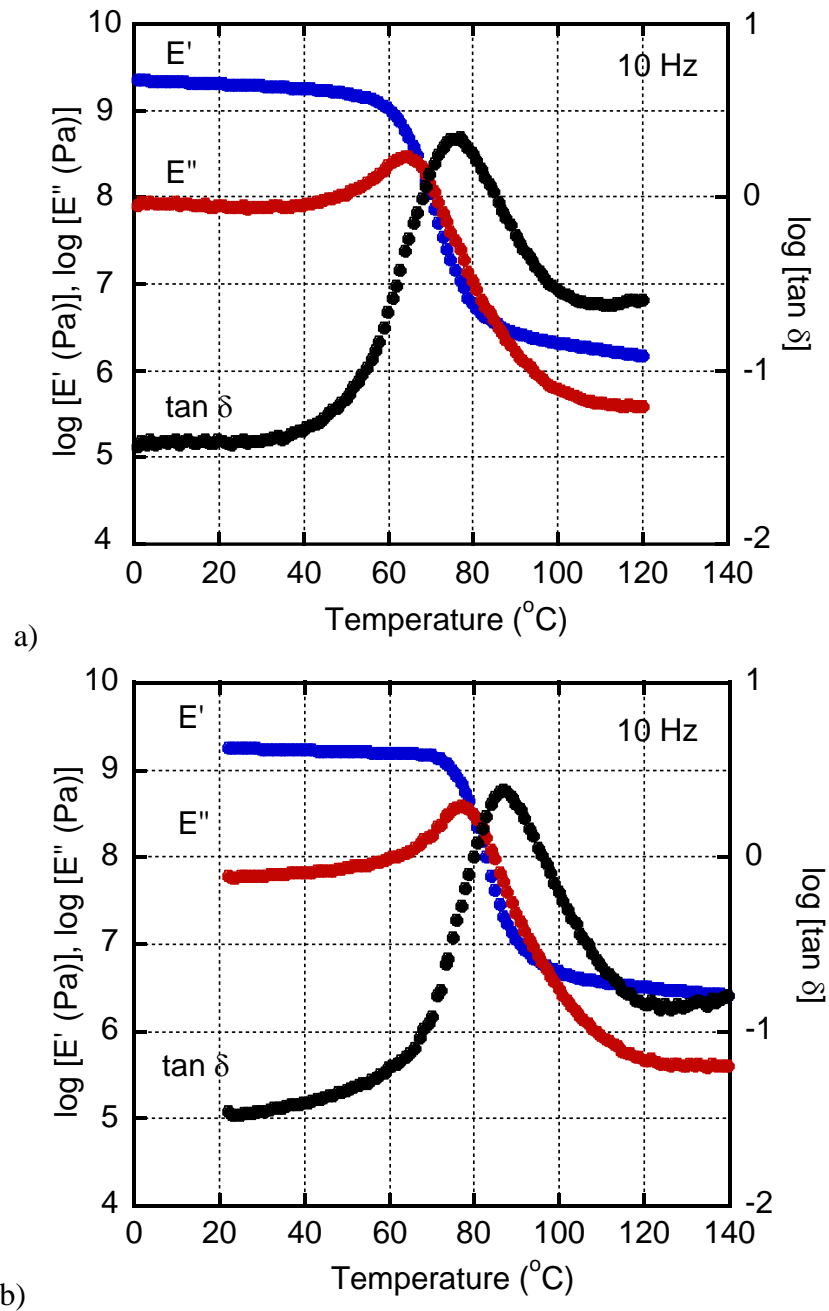


Figure 2-9 Temperature dependence of (blue) tensile storage modulus E' , (red) loss modulus E'' , and (black) loss tangent $\tan \delta$ at 10 Hz for (a) PVB1 and (b) PVB2.

The DSC heating curves are shown in Figure 2-10 for PVB1 and PVB2. Because the samples were kept at room temperature prior to the measurements, the enthalpy relaxation peak is clearly detected. The curves indicate that the samples used in this study are fully amorphous. T_g 's evaluated by DSC are as follows; 75 °C for PVB1 and 76 °C for PVB2.

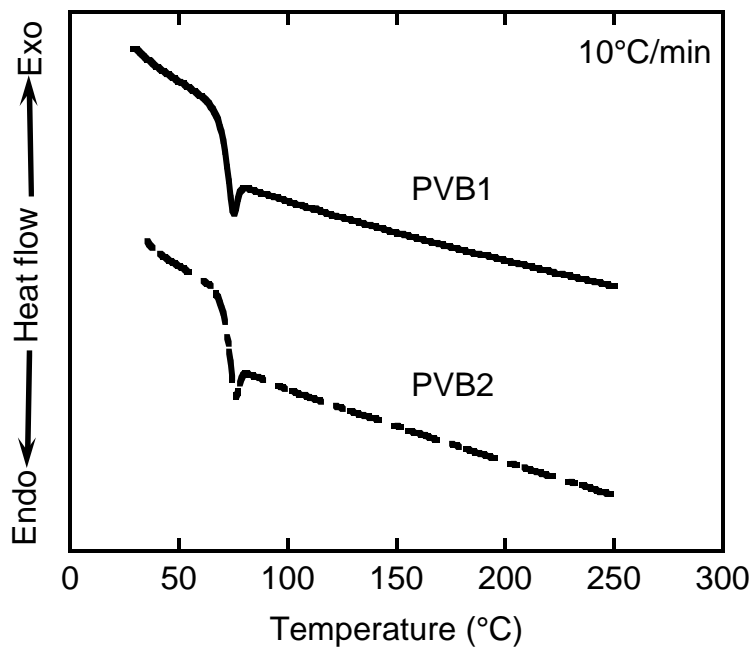


Figure 2-10 DSC heating curves for (line) PVB1 and (dash) PVB2 at a heating rate of 10 °C/min

Moreover, only one diffraction peak in XRD is located at the same position $2\theta=19^\circ$ for PVB1 and PVB2 (Figure 2-11), which is attributed to the amorphous region. Any other peaks are not detected. The results also support that both samples are fully amorphous.

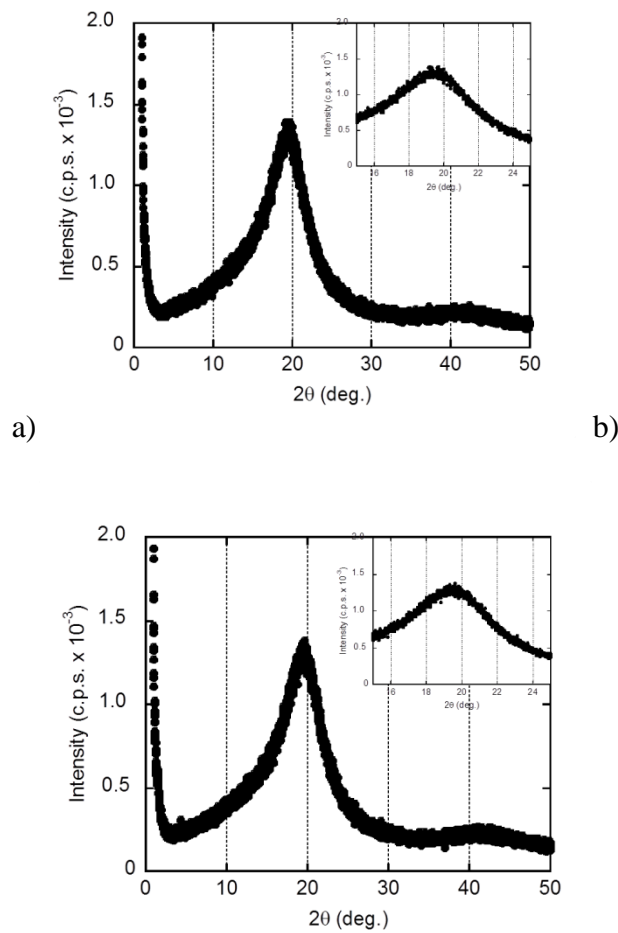


Figure 2-11 X-ray diffraction patterns for (a) PVB1 and (b) PVB2

Figure 2-12 and Figure 2-13 show the master curves of frequency dependence of oscillatory shear moduli such as storage modulus G' and loss modulus G'' . The reference temperature is 100 °C. The curves cover the terminal and rubbery zones in the frequency range. Apparently, the time-temperature superposition principle is applicable to the polymers.

It is reasonable because the material is an amorphous polymer with no crystalline phase. The shift factor a_T is expressed by the following WLF equation³¹ as shown in Figure 2-14.

$$\log a_T = -\frac{c_1(T - T_r)}{c_2 + T - T_r} \quad (2-8)$$

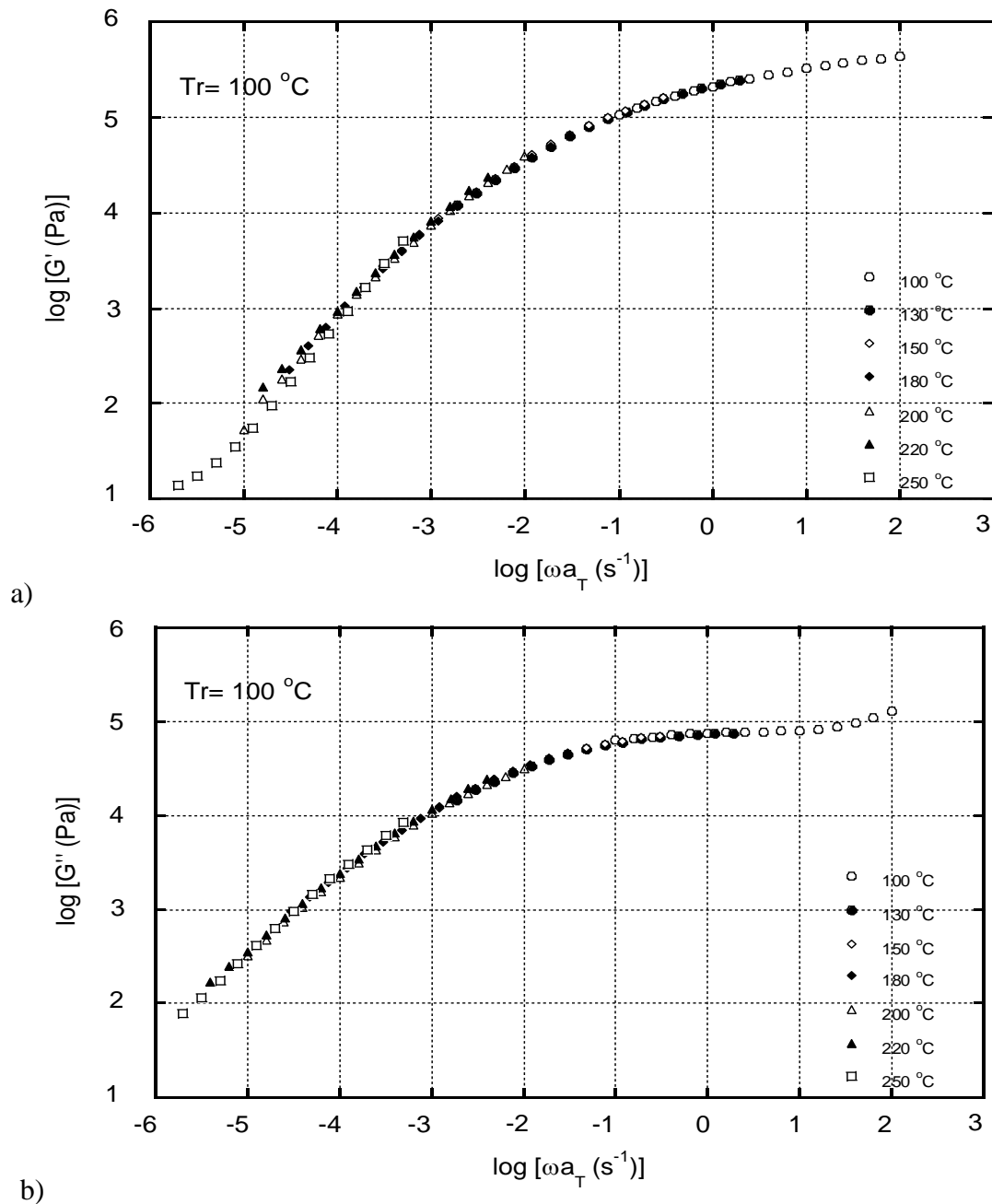


Figure 2-12 Master curves of frequency dependence of oscillatory shear moduli of PVB1 such as (a) storage modulus G' and (b) loss modulus G'' at 100°C as a reference temperature: (open circle) 100°C , (closed circle) 130°C , (open diamond) 150°C , (closed diamond) 180°C , (open triangle) 200°C , (closed triangle) 220°C , and (open square) 250°C .

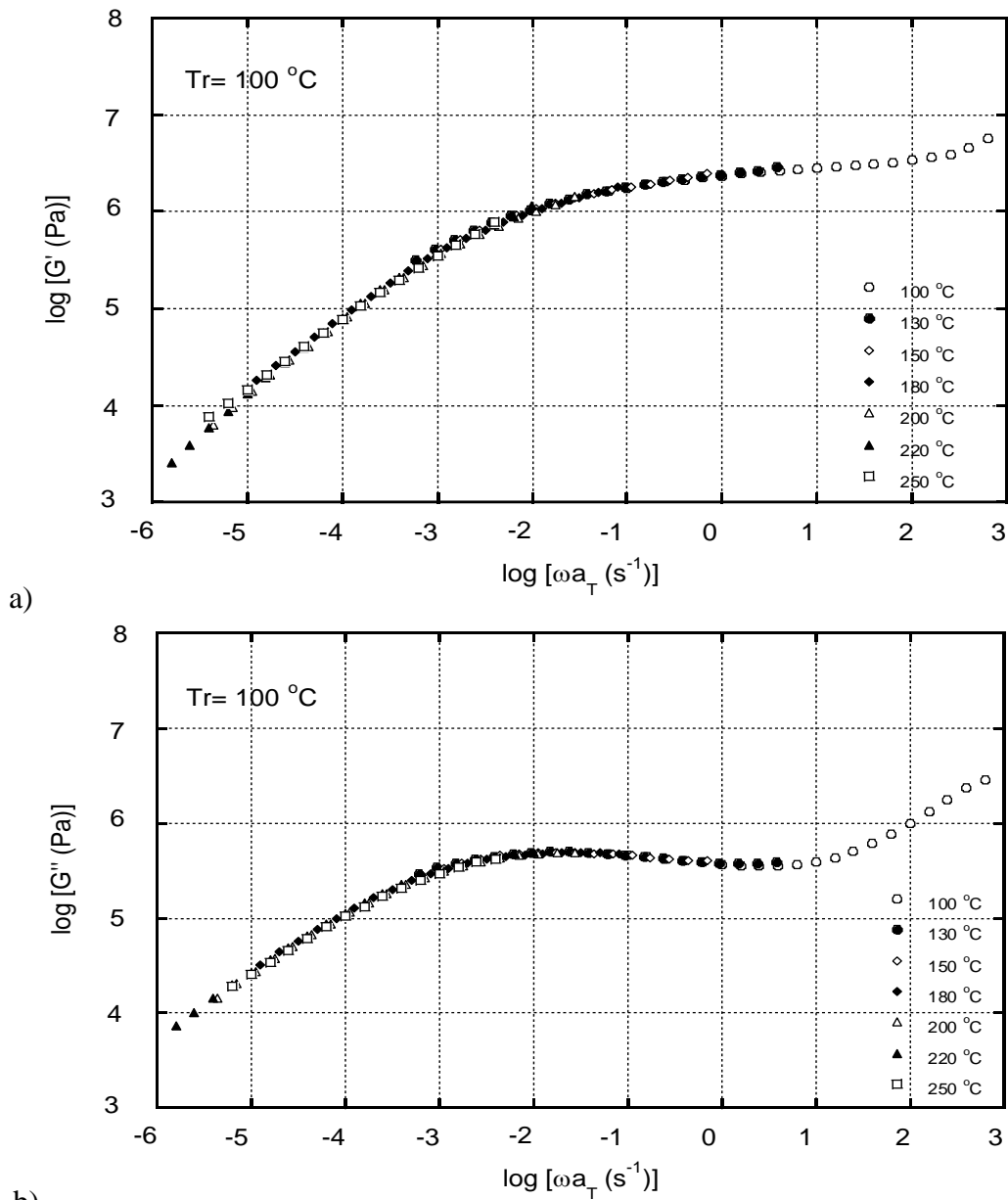


Figure 2-13 Master curves of frequency dependence of oscillatory shear moduli of PVB2 such as (a) storage modulus G' and (b) loss modulus G'' at 100°C as a reference temperature: (open circle) 100°C , (closed circle) 130°C , (open diamond) 150°C , (closed diamond) 180°C , (open triangle) 200°C , (closed triangle) 220°C , and (open square) 250°C .

The shift factors also obey the Arrhenius-type relation (Andrade equation) beyond 150 °C. The apparent flow activation energy beyond 150 °C is calculated to be 55.2 kJ/mol and 52.9 kJ/mol for PVB1 and PVB2, respectively.

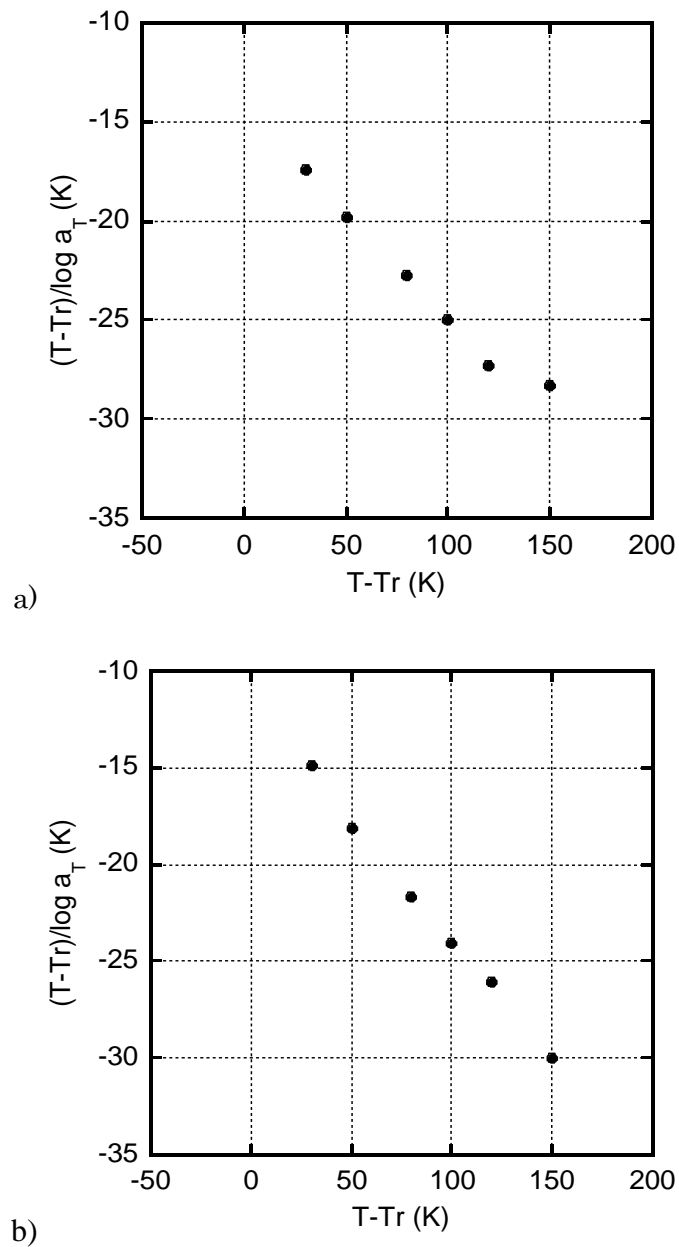


Figure 2-14 Relation between $T-T_r$ and $(T-T_r)/\log a_T$ for (a) PVB1 and (b) PVB2.

Since the polymers have a relatively narrow molecular weight distribution, i.e., $M_w/M_n = 2.0$ and 1.7 for PVB1 and PVB2, respectively, a peak is detected in the G'' curve around at 10^{-1} - 10^{-3} s⁻¹. The rubbery plateau modulus G_N^0 is evaluated by the following equation.

$$G_N^0 = \frac{4}{\pi} \int_{-\infty}^{\frac{a}{2}} G'' d \ln \omega \quad (2-9)$$

where a is the upper limit before the transition zone is entered.

In this study, the G'' versus $\ln \omega$ curve is numerically integrated from $\ln \omega = -\infty$ to the maximum of G'' , and the result was doubled. The G'' curve of PVB1 is not prominent. Therefore, the calculation is performed only for PVB2. It is found that G_N^0 of PVB2 is calculated to be 1.3 MPa at 100 °C, which is significantly higher than those for polystyrene (0.20 MPa) and poly(methyl methacrylate) (0.31 MPa).³²

It is well known that the average molecular weight between entanglement couplings (M_e) is inversely proportional to G_N^0 as,

$$M_e = \frac{\rho RT}{G_N^0} \quad (2-10)$$

where ρ is the density and R is the gas constant.

Furthermore, the density at 100 °C is measured and found to be 1118.1 kg/m³ by the buoyancy method. Therefore, M_e is calculated to be 2,670. Since the time span for the rubbery plateau is proportional to $(M/M_e)^{3.4}$, the low value of M_e is responsible for the wide temperature range of the rubbery region.³³ Furthermore, the value is much smaller

than that of poly(vinyl acetate) ($M_e = 8,500$).³² In case of poly(vinyl alcohol) (PVA), the critical molecular weight ($\cong 2M_e$) is known to be 5,300-7,500.^{34,35} Therefore, M_e of poly(vinyl butyral) homopolymer must be low. It should be interesting to note that polysaccharides with a random-coil conformation such as cellulose, cellulose acetate propionate, and galactomannan have relatively low M_e , 3,200 for cellulose,³⁶ 3,100 for cellulose acetate propionate³⁷ and 4,600 for galactomannan (guar gum),³⁸ suggesting the flexible nature of a saturated ring containing oxygen atoms.

2.3.2 Capillary Extrusion Properties

Figure 2-15 shows the flow curves at various temperatures evaluated by the capillary rheometer. The master curves are shown in Figure 2-16 at the reference temperature of 100 °C. As similar to linear viscoelastic properties, the time-temperature superposition is applicable. Figure 2-17 shows the optical micrographs observed by the stereomicroscope for the strands extruded at various shear rates and temperatures. The flow curves and the pictures indicate that the apparent slippage such as spurt flow and slip-stick failure is not detected in the experimental shear rate range at any temperature. This is presumably attributed to the good adhesive strength of PVB to the die wall. Moreover, the onset of shark-skin failure is shown in Figure 2-18. The tiny surface roughness is detected on the strands.

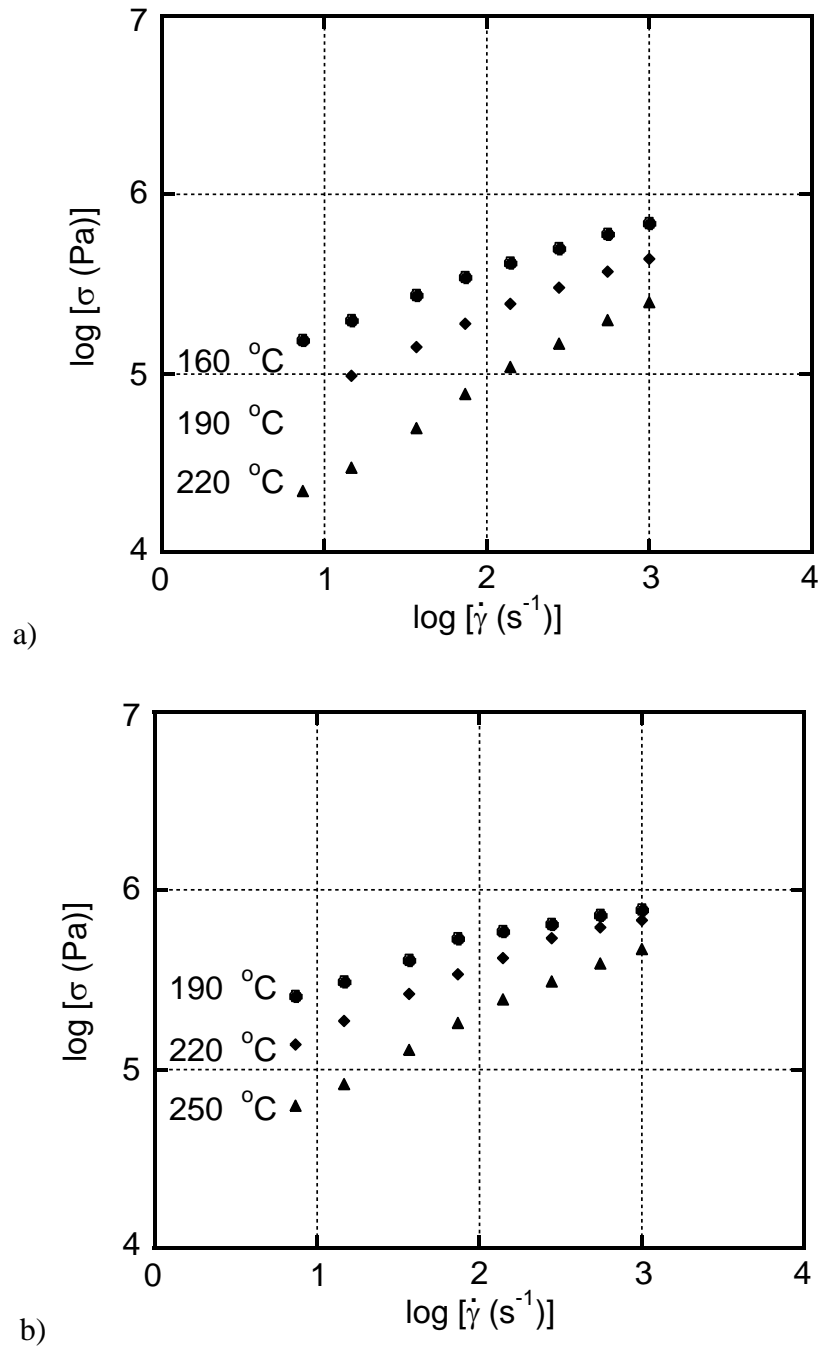


Figure 2-15 Shear stress σ as a function of shear rate $\dot{\gamma}$ of (a) PVB1 at 160°C as a reference temperature: (circle) 160°C, (diamond) 190°C, and (triangle) 220°C and (b) PVB2 at (circle) 190°C, (diamond) 220°C, and (triangle) 250°C.

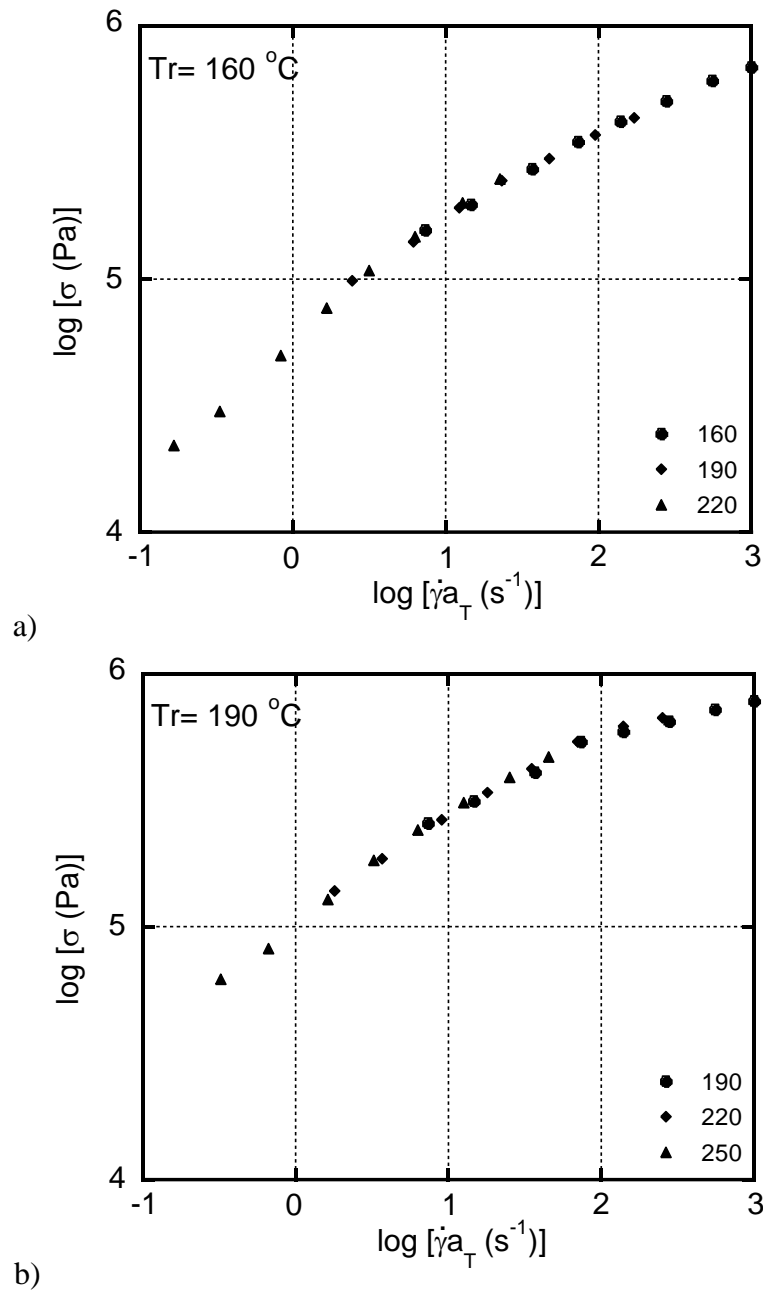
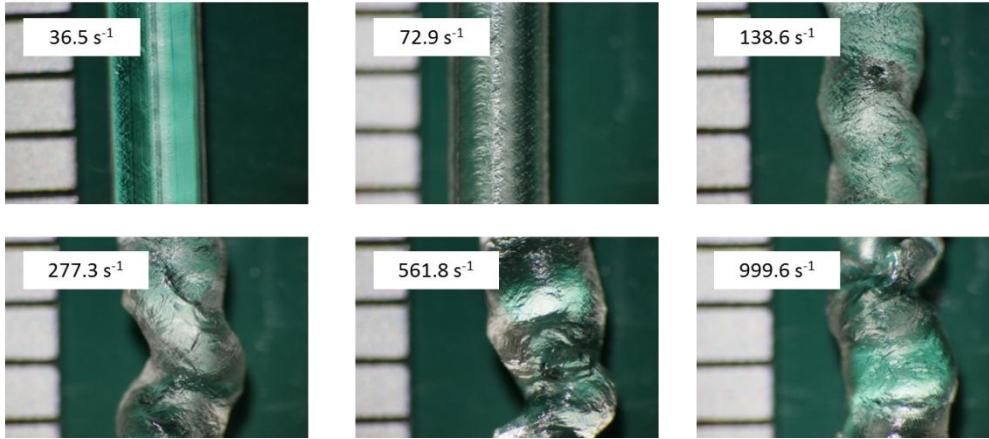
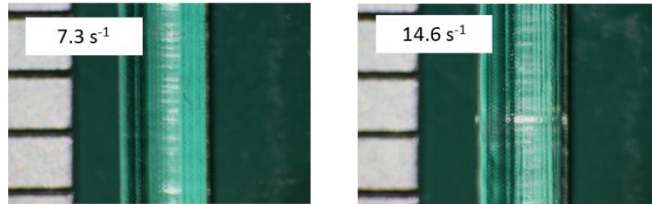


Figure 2-16 Master curves of shear stress σ as a function of shear rate $\dot{\gamma}$ of (a) PVB1 at 160°C as a reference temperature: (circle) 160°C, (diamond) 190°C, and (triangle) 220°C and (b) PVB2 at 190°C as a reference temperature: (circle) 190°C, (diamond) 220°C, and (triangle) 250°C.

160°C

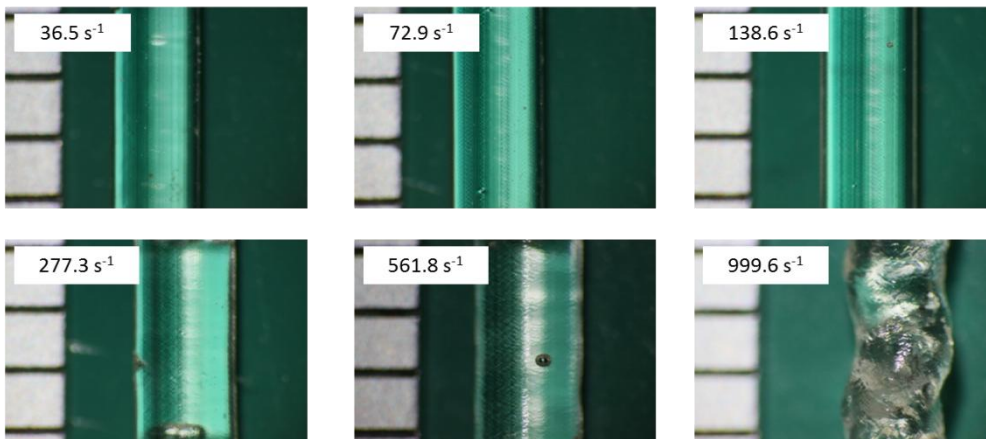
PVB-1



a)

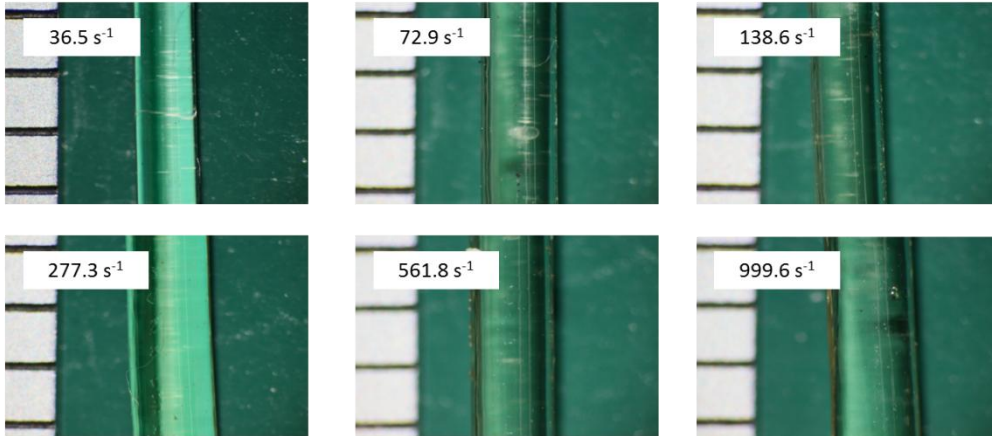
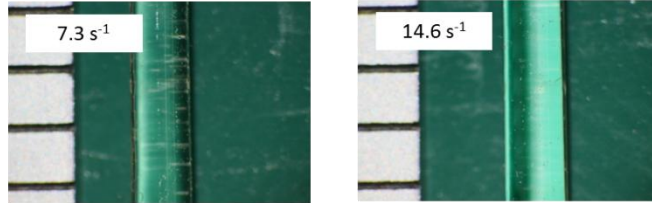
190°C

PVB-1



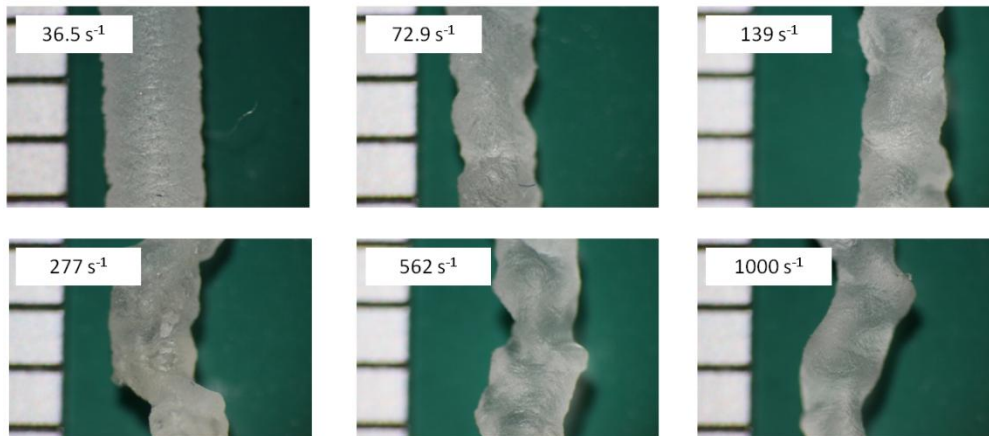
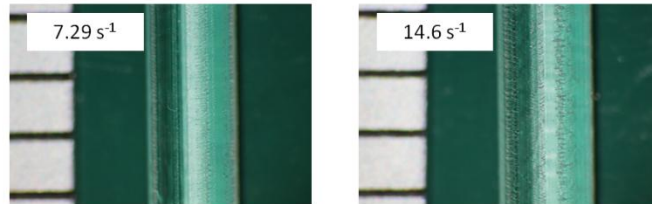
b)

220°C
PVB-1



c)

190°C
PVB-2



d)

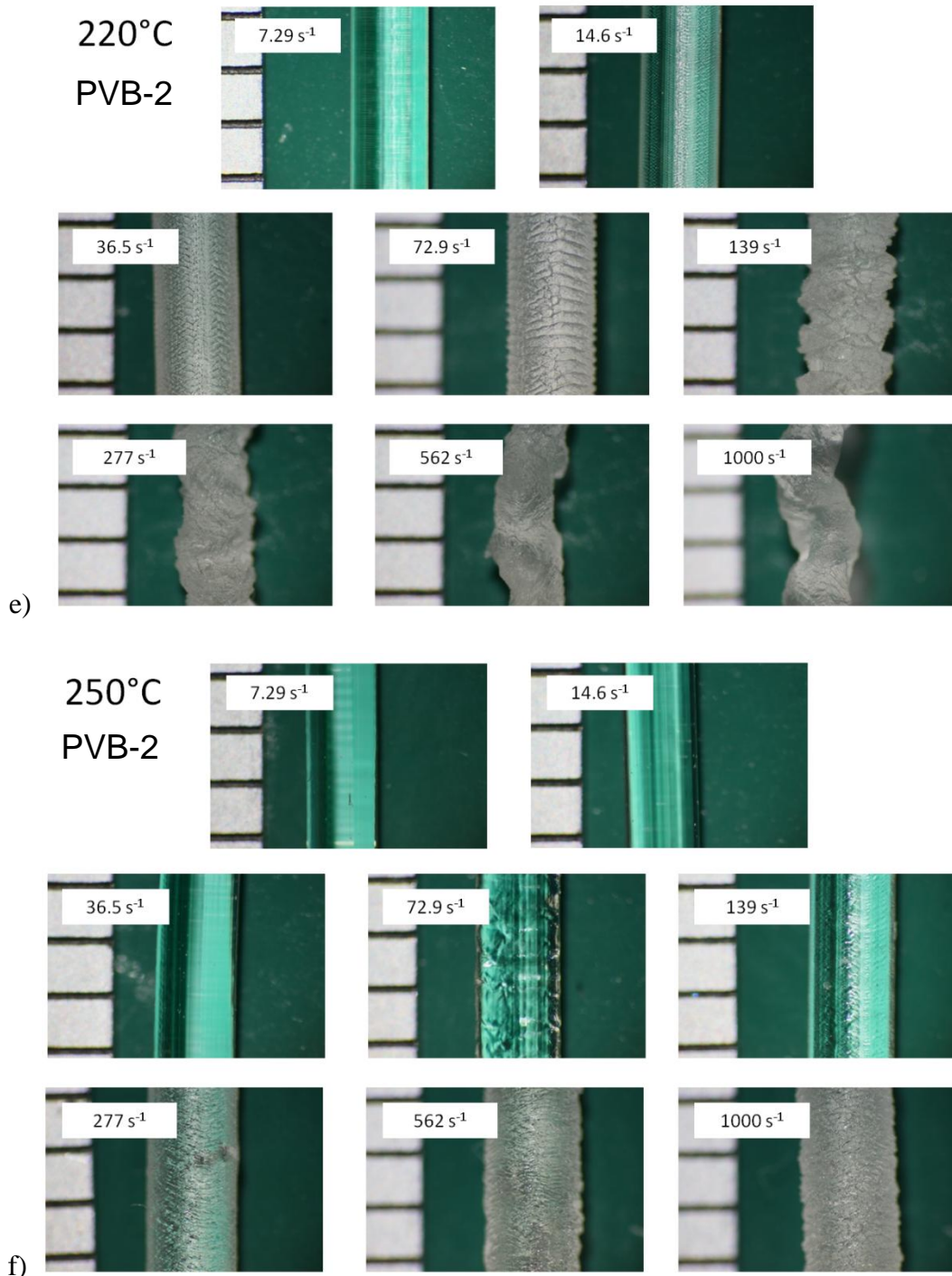


Figure 2-17 Photographs of strands extruded at (a) 160 °C, (b) 190 °C, and (c) 220 °C at various shear rates for PVB1 and (d) 190 °C, (e) 220 °C, and (f) 250 °C at various shear rates for PVB2. The distance between the neighbor lines is 1 mm.

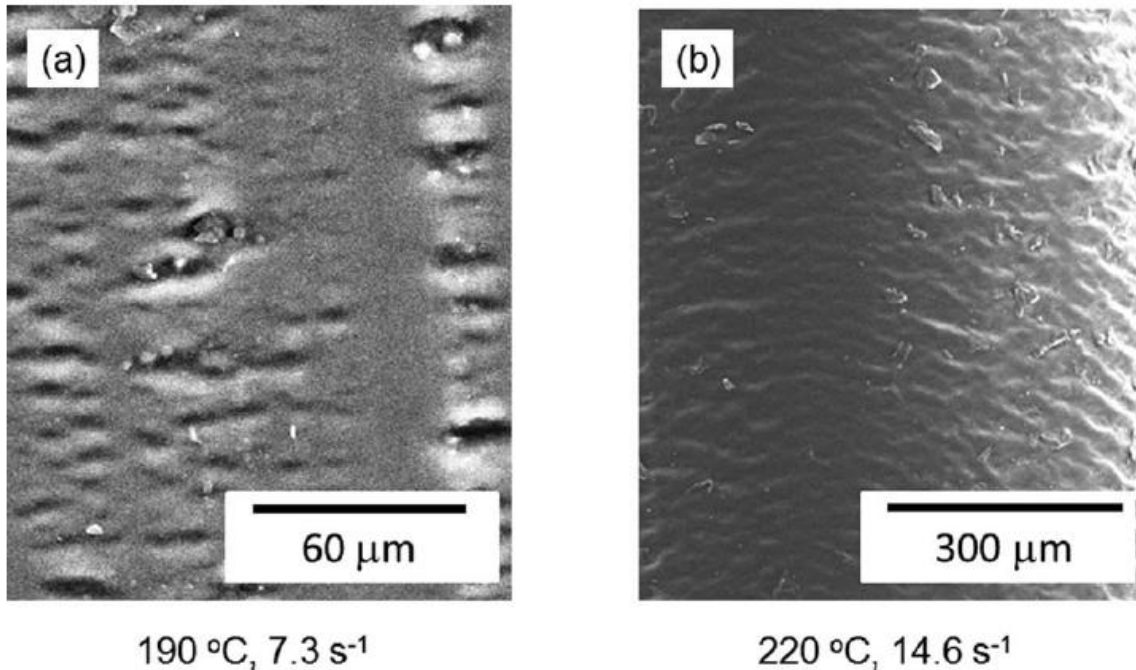


Figure 2-18 SEM images of the surface of strands extruded at the following conditions: (a) 7.29 s⁻¹, 190 °C and (b) 14.6 s⁻¹, 220 °C.

The strands obtained at 190 °C show rough surface at any shear rate (shown in Figure 2-18(a)), suggesting that the onset shear stress is lower than 0.256 MPa (at 7.29 s⁻¹). The gross melt fracture with rough surface is detected at 72.9 s⁻¹ at this temperature. At higher temperatures, rough surface, i.e., shark-skin failure, is detected at 0.185 MPa (14.6 s⁻¹ at 220 °C, as shown in Figure 2-18(b)) and 0.182 MPa (72.9 s⁻¹ at 250 °C). The results indicate that the onset stress of the shark-skin failure is around 0.18 MPa for PVB. The value is almost similar to that of polyethylene and slightly higher than that of isotactic polypropylene.³⁹

Both shark-skin failure and gross melt fracture should be seriously considered for industrial applications, because they decide the production speed. For most linear

polymers, in general, the shark-skin failure appears prior to the gross melt fracture.³⁹⁻⁴¹

As shown in the linear viscoelastic properties, G_N^0 is relatively high for PVB, and thus the onset stress of the shark-skin failure must be low irrespective of the origin. The predicted values of onset stresses for the present sample are $\sigma_c = 0.9$ MPa and $\sigma_s = 1.2 \times C_{ad}$ MPa, respectively at 220 °C. Considering that C_{ad} is around 0.1-0.2,⁴² there is a possibility that the surface slippage is the origin of the shark-skin failure for PVB.

Although Equations (2-1) – (2-4) predict the onset stress for a monodispersed polymer, molecular weight distribution also has a dominant effect on the shark-skin failure as indicated by Yamaguchi et al.²⁸ Since the relaxation time of the present PVB1 is not evaluated, the critical stress cannot be calculated from Equation 2-5. However, the discussion on the onset stress without considering the molecular weight distribution becomes possible. In this study, M_w/M_n of the present sample is only 1.7, which is a typical value for commercialized PVB.^{1,2} However, the value is narrower than those of most commercialized polymers. In spite of the narrow molecular weight distribution, the onset stress is not so low and similar to that of commercially available polyethylenes having broad molecular weight distribution. The result indicates that PVB intrinsically has a high level of onset shear stress for the shark-skin failure.

In the next chapter, PVB1 is employed to study its self-healing ability, as well as the rheological properties. It is found from the dynamic mechanical measurement that PVB shows high level of rubbery plateau modulus, i.e., low entanglement molecular weight. Therefore, PVB with high molecular weight shows broad rubbery region, which is commercially available. In other words, it hardly shows macroscopic flow even beyond T_g .

2.5 Conclusions

In this chapter, the linear viscoelastic properties and the flow instability at capillary extrusion for a terpolymer composed of vinyl butyral, vinyl alcohol, and vinyl acetate are investigated. It is showed that PVB1 and PVB2 are amorphous polymer having T_g around at 68 and 78 °C. Their T_g 's are slightly different because of the slight difference in the chemical composition. Further, it is found that PVB2 has a high level of rubbery plateau modulus $G_N^0 = 1.3$ MPa, i.e., low M_e (2,670). Consequently, it shows the rubbery state in the wide temperature range. The low M_e also affects the high level of the onset shear stress of the shark-skin failure, around 1.8 MPa at 250 °C, leading to high out-put rate at extrusion processing in spite of the narrow molecular weight distribution.

References

1. Remsen, E. E., Determination of Molecular Weight for Poly(vinyl butyral) using Size Exclusion Chromatography/Low - Angle Laser Light Scattering (SEC/LALLS) in Hexafluoroisopropanol. *J Appl Polym Sci* **1991**, *42* (2), 503-510.
2. Striegel, A. M., Mid - chain grafting in PVB - graft - PVB. *Polym Int* **2004**, *53*, 1806-1812.
3. Lebek, B.; Menge, H.; Schlothauer, K.; Schneider, H.; Kivayeva, L.; Fedotov, V., ¹³C NMR Investigation of The Microdynamics of Poly(vinyl butyral). *Polymer* **1991**, *32*, 2335-2339.
4. Cascone, E.; David, D. J.; Di Lorenzo, M. L.; Karasz, F. E.; MacKnight, W. J.; Martuscelli, E.; Raimo, M., Blends of Polypropylene with Poly(vinyl butyral). *J Appl Polym Sci* **2001**, *82*, 2934-2946.
5. Fernandez, M.; Fernandez, M.; Hoces, P., Synthesis of Poly(vinyl butyral)s in Homogeneous Phase and Their Thermal Properties. *J Appl Polym Sci* **2006**, *102*, 5007-5017.
6. Morais, D.; Valera, T. S.; Demarquette, N. R., Evaluation of the Surface Tension of Poly(vinyl butyral) Using the Pendant Drop Method. *Macromol Symp* **2006**, *245-246*, 208-214.
7. Jeong, H. K.; Rooney, M.; David, D. J.; MacKnight, W. J.; Karasz, F. E.; Kajiyama, T., Miscibility of Polyvinyl butyral/nylon 6 blends. *Polymer* **2000**, *41*, 6003-6013.
8. Valera, T. S.; Demarquette, N. R., Polymer Toughening using Residue of Recycled Windshields: PVB film as Impact Modifier. *Eur Polym J* **2008**, *44*, 755-768.

9. Lee, J.-C.; Ajima, K. N.; Ikehara, T.; Nishi, T., Conductive-Filler-Filled Poly(ϵ -caprolactone)/Poly(vinyl butyral) Blends. II. Electric Properties (Positive Temperature Coefficient Phenomenon). *J Appl Polym Sci* **1997**, *65*, 409-416.
10. Lee, J.-C.; Ikehara, T.; Nishi, T., Morphology and Electrical Properties of Carbon Black-Filled Poly(ϵ -caprolactone)/Poly(vinyl butyral) blends. *J Appl Polym Sci* **1998**, *69*, 193-199.
11. Nozue, Y.; Kurita, R.; Hirano, S.; Kawasaki, N.; Ueno, S.; Iida, A.; Nishi, T.; Amemiya, Y., Spatial Distribution of Lamella Structure in PCL/PVB Band Spherulite Investigated with Microbeam Small-and Wide-angle X-ray Scattering. *Polymer* **2003**, *44*, 6397-6405.
12. Tripathy, A. R.; Chen, W.; Kukureka, S. N.; MacKnight, W. J., Novel Poly(butylene terephthalate)/Poly(vinyl butyral) Blends Prepared by in situ Polymerization of Cyclic Poly(butylene terephthalate) Oligomers. *Polymer* **2003**, *44*, 1835-1842.
13. Sincock, T. F.; David, D. J., Miscibility and Properties of Poly(vinyl butyral) and Thermoplastic Polyurethane Blends. *Polymer* **1992**, *33*, 4515-4521.
14. Qiu, Y.-R.; Ouyang, W., Rheological Behavior of Poly(vinyl butyral)/Polyethylene glycol Binary Systems. *Mater Sci Eng, C* **2012**, *32*, 167-171.
15. Peng, Y.; Sui, Y., Compatibility Research on PVC/PVB Blended Membranes. *Desalination* **2006**, *196*, 13-21.
16. Chen, W.; David, D. J.; MacKnight, W. J.; Karasz, F. E., Miscibility and Phase Behavior in Blends of Poly(vinyl butyral) and Poly(methyl methacrylate). *Macromolecules* **2001**, *34*, 4277-4284.

17. Qian, J. W.; Chen, H. L.; Zhang, L.; Qin, S. H.; Wang, M., Effect of Compatibility of Cellulose acetate/Poly(vinyl butyral) Blends on Pervaporation Behavior of Their Membranes for Methanol/Methyl tert-Butyl Ether Mixture. *J Appl Polym Sci* **2002**, *83*, 2434-2439.
18. Chen, W.; David, D. J.; MacKnight, W. J.; Karasz, F. E., Miscibility and Morphology of Blends of Poly(3-hydroxybutyrate) and Poly(vinyl butyral). *Polymer* **2001**, *42*, 8407-8414.
19. Jeong, H. K.; Rooney, M.; David, D. J.; MacKnight, W. J.; Karasz, F. E.; Kajiyama, T., Miscibility and Characterization of The Ternary Crystalline System: Poly(vinyl butyral)/Poly(vinyl alcohol)/nylon6. *Polymer* **2000**, *41*, 6671-6678.
20. Tupy, M.; Merinska, D.; Kasparkova, V., Material Recycling, Trends and Perspectives. *InTech: Croatia* **2012**.
21. Yamaguchi, M.; Miyata, H.; Tan, V.; Gogos, C. G., Relation Between Molecular Structure and Flow Instability for Ethylene/ α -Olefin Copolymers. *Polymer* **2002**, *43*, 5249-5255.
22. Meller, M.; Luciani, A.; Sarioglu, A.; Månson, J. A. E., Flow Through a Convergence. Part 1: Critical Conditions for Unstable Flow. *Polym Eng Sci* **2002**, *42*, 611-633.
23. Kulikov, O.; Hornung, K.; Wagner, M., Silanols Cured by Borates as Lubricants in Extrusion of LLDPE. Impact of Elasticity of The Lubricant on Sliding Friction. *Rheol Acta* **2007**, *46*, 741-754.
24. Brochard, F.; De Gennes, P. G., Shear-dependent Slippage at a Polymer/Solid Interface. *Langmuir* **1992**, *8*, 3033-3037.

25. Allal, A.; Lavernhe, A.; Vergnes, B.; Marin, G., Relationships Between Molecular Structure and Sharkskin Defect for Linear Polymers. *J Non-Newton Fluid* **2006**, *134*, 127-135.
26. Allal, A.; Vergnes, B., Molecular Design to Eliminate Sharkskin Defect for Linear Polymers. *J Non-Newton Fluid* **2007**, *146*, 45-50.
27. Monchai, S.; Mieda, N.; Anh Doan, V.; Nobukawa, S.; Yamaguchi, M., Effect of Shear History on Flow Instability at Capillary Extrusion for Long-chain Branched Polyethylene. *J Appl Polym Sci* **2012**, *124*, 429-435.
28. Yamaguchi, M.; Miyata, H.; Tan, V.; Gogos, C. G., Relation between Molecular Structure and Flow Instability for Ethylene/ α -Olefin Copolymers. *Polymer* **2002**, *43*, 5249-5255.
29. Mieda, N.; Yamaguchi, M., Flow Instability for Binary Blends of Linear Polyethylene and Long-chain Branched Polyethylene. *J Non-Newton Fluid* **2011**, *166*, 231-240.
30. Suzuki, M.; Ali, M. A. M.; Okamoto, K.; Taniike, T.; Terano, M.; Yamaguchi, M., Effect of Stereoregularity of Polypropylene on Flow Instability in Capillary Extrusion. *Adv Polym Tech* **2009**, *28*, 185-191.
31. Ferry, J. D., *Viscoelastic Properties of Polymers*. John Wiley & Sons **1980**.
32. Fetters, L. J.; Lohse, D. J.; Colby, R. H., *Physical Properties of Polymers Handbook*, 2nd ed. Mark, J. E., Ed.; Springer, Berlin **2006**, Chapter 25.
33. Graessley, W. W., *Polymeric Liquids & Networks: In Dynamics and Rheology*. Garland Science, London **2008**.

34. Aharoni, S. M., Correlation Between Chain Parameters and The Plateau Modulus of Polymers. *Macromolecules*. **1986**, *19*, 426-434.
35. Porter, R. S.; Johnson, J. F., The Entanglement Concept in Polymer Systems. *Chemical Reviews* **1966**, *66*, 1-27.
36. Horinaka, J.; Yasuda, R.; Takigawa, T., a. Entanglement Properties of Cellulose and Aylose in an Ionic Liquid. *J. Polym. Sci. B: Polym. Phys.* **2011**, *49*, 961-965.
37. Horinaka, J.-i.; Yasuda, R.; Takigawa, T., Rheological Properties of Concentrated Solutions of Galactomannans in an Ionic Liquid. *Carbohydrate polymers* **2012**, *89*, 1018-1021.
38. Maeda, A.; Inoue, T., On the Viscoelastic Segment Size of Cellulose. *Nihon Reoroji Gakk* **2011**, *39*, 159-163.
39. Koopmans, R.; Doelder, J. d.; Molenaar, J., *Polymer Melt Fracture*. **2010**.
40. Hatzikiriakos, S. G.; Migler, K. B., *Polymer Processing Instabilities*. Marcel Dekker, New York **2005**.
41. Tadmor, Z.; Gogos, C. G., *Principles of polymer processing*. John Wiley & Sons **2006**.
42. Allal, A.; Vergnes, B., Molecular Design to Eliminate Sharkskin Defect for Linear Polymers. *J Non-Newton Fluid* **2007**, *146*, 45-50.

Chapter 3

Self-healing Behavior of Poly(Vinyl Butyral)

3.1 Introduction

As well known, amorphous polymers such as PVB show rheological four regions according to time and temperature, such as glassy, transition, rubbery, and terminal zones as long as the molecular weight is higher than the critical molecular weight. The time/temperature range of the rubbery state is determined by the number of entanglement couplings per a molecule. In the previous chapter, the entanglement molecular weight of PVB was studied and found to be 2,670. This value is relatively low compared to other conventional plastics. Therefore, as shown in chapter 2, PVB with high molecular weight shows a broad rubbery region. Consequently, it hardly shows macroscopic flow. This is very important for a self-healing polymer using molecular interdiffusion.

Self-healing polymeric materials have been inspired by biological systems, in which a damage triggers an autonomic healing response. The self-healing materials have the ability to restore themselves when they are damaged. Up to now, various methods have been reported to provide this ability,^{1,2,3,4} for example, chemical reaction, intermolecular interaction between specific functions, anchor effect and chain interdiffusion.

Among them, the methods to use chemical reaction have been studied greatly these days. Composites with microcapsules^{5,6,7,8,9} and hollow fibers,^{10,11,12} in which a healing agent is loaded, have been developed after the pioneering works by White et al.⁹ and Dry.¹⁰ Reversible chemical reactions such as Diels-Alder/Retro Diels-Alder have been focused to develop thermally reversible gels.^{13,14} Another important reversible reaction is photo-induced cycloaddition of coumarin.¹⁵

Intermolecular interactions between specific groups are also employed, such as hydrogen bonding,^{16,17,18,19,20} ionic interaction in ionomers,^{21,22} and π - π stacking interaction.²³ Furthermore, the addition of thermoplastics into a thermoset resin was proposed,²⁴⁻²⁶ which has a similar concept of the anchor effect at adhesion.

Moreover, the chain interdiffusion, which is also used for an adhesion method available only for a polymer, has been known for a long time to be utilized to recover mechanically-induced damages beyond the glass transition temperature T_g .²⁷ Yamaguchi et al. investigated a polyurethane network having a lot of dangling chains, which exhibits self-healing ability beyond T_g without any chemical reactions.^{28,29,30} Dangling chains in a gel, defined as inelastic partial chains whose one end is free to move, can also show interdiffusion by reptation motion. As a result, a weak gel having a large number of dangling chains exhibits good self-healing ability.

The mechanism of so-called “crack healing” has been summarized and explained by Wool using the minor chain model²⁷ based on the reptation concept.³¹ According to him, there are five stages for the crack healing process through surface rearrangement, surface approaching, wetting, diffusion and randomization.²⁷ Brown et al.³² studied the relation between the interdiffusion of aromatic polyimide and the adhesive strength. They found

that at least 200 nm is required as the diffusion distance in order to show good mechanical strength. Their results suggest that chain mobility at surface is important for the healing behavior, indicating that the surface rheology should be comprehended to prepare a self-healing material. Kajiyama et al. revealed that the surface glass transition temperature T_g^s is lower than the bulk glass transition temperature T_g^b .^{33,34,35,36} The marked molecular motion at the surface was explained in term of chain end effect and reduced chain cooperativity by the large free volume on the surface. Moreover, the surface region also possesses specific chain conformation, which is different from the bulk region.^{37,38}

In this chapter, the self-healing ability of PVB is studied at the temperature below T_g , i.e., in the glassy region.

3.1.1 Approaches to self-healing

3.1.1.1 Capsule-based self-healing materials

This method heals damage by chemical reaction. A healing agent has to be stored in a media and embedded into materials in advance. As soon as the fragile reservoirs are destroyed, the healing agent is released into the cracks due to capillary effect and reacts with a matrix polymer, i.e., heal the cracks. There are two types according to the containers of a repairing agent: capsule-based self-healing materials and vascular self-healing materials. Taking the advantages of crack triggered by healing agent, manual intervention might be no longer necessary.

Capsule-based self-healing materials are studied greatly these days, in which the capsules contain the healing agent (Figure 3-1). When the capsules are ruptured by damage, the healing agent is released to the damaged site for curing and filling the crack. The

reaction is triggered by the catalyst dispersed in the matrix. Subsequent chemical reaction of the healing agent with the aid of and the embedded catalyst heals the material and prevents further growth of cracks. Composites with microcapsules in which healing agent is loaded, have been developed after the pioneering works by White et al.⁹ and Dry.¹⁰

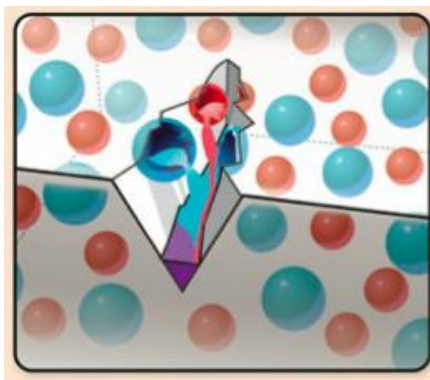


Figure 3-1 Illustration of capsules-based self-healing materials³⁹ (Blaiszik, B., *Macromolecules*, 2010)

The healing occurs based on ring-opening metathesis polymerization (ROMP). For example, a microencapsulated healing agent, dicyclopentadiene (DCPD), and a Grubbs' catalyst, benzylidene ruthenium (IV) dichloride or bis(tricyclohexylphosphine), were mixed and dispersed in an epoxy resin matrix.⁴⁰

White et al.⁹ noted that the addition of microcapsules and catalyst to the epoxy matrix, as compared to the neat epoxy, can almost recover the mechanical toughness (Figure 3-2). The healing efficiency of this specimen was 60% on average, and a maximum value was 75% of the virgin fracture load.

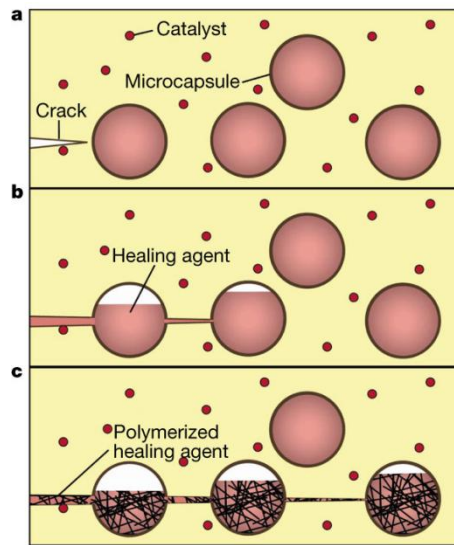


Figure 3-2 Autonomic healing concept incorporating encapsulated healing agent and embedded catalyst particles in an epoxy matrix; (a) damage event causes crack formation in the matrix; (b) crack ruptures the microcapsules, releasing liquid healing agent into crack plane; (c) healing agent polymerizes upon contact with embedded catalyst, bonding crack closed.⁹ (White, S.R., *Nature*, 2001)

In 2002, Brown et al.⁴¹ also investigated the effect of the inclusion of microcapsules and catalyst particles on the mechanical properties of the epoxy matrix. They found that the virgin fracture toughness increased with an increase in the concentration of microcapsules, reaching a maximum at 15 wt%. This value is more than twice of the toughness of the neat epoxy. The catalyst particle size also affects the fracture toughness. The values increase with decreasing the particle size for both virgin and healed samples. The maximum value of toughness was achieved with 180–355 μm catalyst particles. The healed fracture toughness reached a maximum at 2.5 wt% catalyst, and a

significant drop in virgin fracture toughness occurred at 3 wt% catalyst. The maximum healing efficiency was up to 90% for an in-situ sample containing 2.5 wt% Grubbs' catalyst and 5 wt% microcapsules.

In 2008, Chipara et al.⁴² studied the self-healing of block copolymers. In their system, 5% of microcapsules filled with monomer (dicyclopentadiene, DCPD) and 1% Grubbs' catalyst were dispersed into polystyrene-butadiene tri-block copolymer (Figure 1-20). The structure of self-healed block copolymer has been investigated by optical and electron microscopy. Furthermore, the polymerization reaction of the monomer (DCPD) with Grubbs' catalyst was monitored by Raman spectroscopy.

3.1.1.2. Vascular self-healing materials

Vascular self-healing materials sequester the healing agent in a network in the form of capillaries or hollow channels. They are interconnected until a damage triggers self-healing (Figure 3-3). When the vascular tube is damaged, the healing agent is delivered. The network is refilled by an external source or from an undamaged one. This refilling action allows multiple cycles of healing reaction.

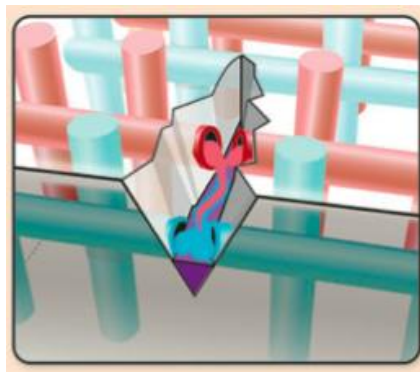


Figure 3-3 Illustration of vascular self-healing materials³⁹ (Blaiszik, B., *Macromolecules*, 2010)

In 2007, Toohey et al.⁴³ published the system composed of liquid DCP as the healing agent and solid Grubbs' catalyst to initiate polymerization of DCP. The catalyst is dispersed into a 700 μm thick epoxy coating. It is applied to the top surface of the microvascular substrate, and the 200 μm wide channels are filled with DCP and then sealed (Figure 3-4). This network of microchannels can be replenished with an additional healing agent, allowing for multiple healing events to occur at the same location in the material. This system achieved the healing efficiency of 60% with 10 wt% catalyst in the top coating, and was able to demonstrate healing for up to seven cycles. The average healing efficiency per a cycle is independent of the amount of catalyst. The limiting factor of healing in this system is the catalyst. Once all of the catalyst has been used for healing, it will no longer occur, even with a continuous supply of monomer.

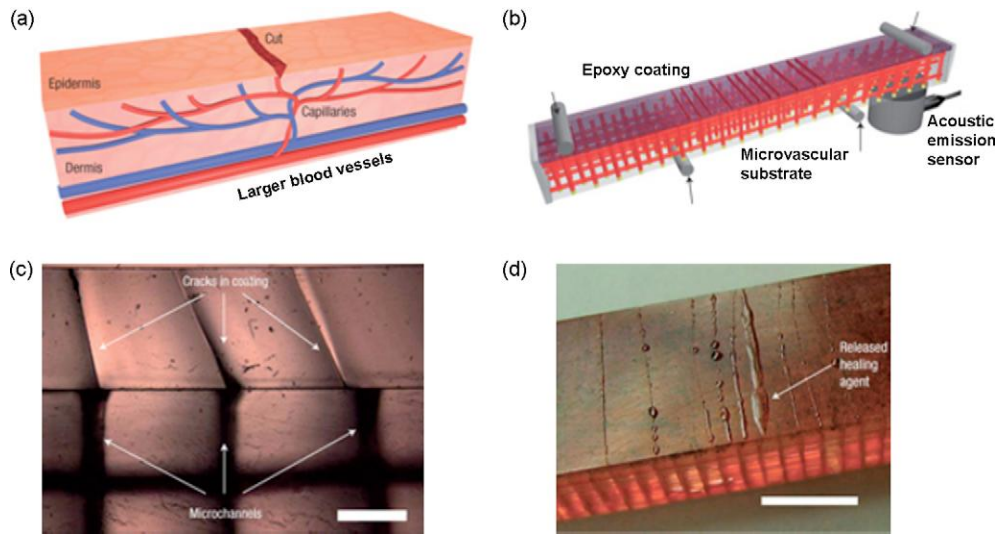


Figure 3-4 (a) Schematic of the vasculature in skin, (b) schematic of the self-healing composite structure containing microvascular substrate, (c) coating of material, showing that the cracks that form at the surface propagate towards the microchannel openings at the interface, and (d) image of self-healing material after cracking, revealing excess healing agent on the surface.⁴³ (Toohey, K. S., *Nature Mater*, 2007)



Figure 3-5 Illustration of intrinsic self-healing materials³⁹ (a) Reversible bonding, (b) Molecular interdiffusion and (c) Ionomeric self-healing (Blaiszik, B., *Macromolecules*, 2010)

3.1.1.3 Self-healing from dispersed thermoplastic polymer

Self-healing in thermoset materials can be achieved by addition of a thermoplastic. Self-healing occurs by the melting and subsequent flow of the thermoplastic material into the crack plane, filling the crack of the matrix material. Luo et al.⁴⁴ prepared a thermally remendable thermoset epoxy resin by dispersing phase-separated poly(caprolactone) (PCL) in an epoxy matrix. Upon heating, the PCL melts and undergoes a volumetric thermal expansion to fill the damage.

3.1.1.4 Self-healing polymers based on reversible reactions

Self-healing material based on reversible reaction includes components that can be reversibly transformed from the monomeric state to the cross-linked polymeric state through the addition of external energy. Generally, a damaged polymer is subjected to heat or intense photoillumination, triggering enhanced mobility in the damage region, bond reformation, and polymer remending. The Diels-Alder (DA) and retro-Diels-Alder (rDA) reactions have been studied widely. Original one was proposed by Chujo.

Chen et al.¹⁵ demonstrated a thermally activated self-healing system based on the DA reaction of synthesized furan-maleimide polymers (Figure 3-6). At temperature above 120 °C, the intermonomer linkages disconnect but the reconnect upon cooling. This process is fully reversible and can be used to restore fractured parts of the polymer.

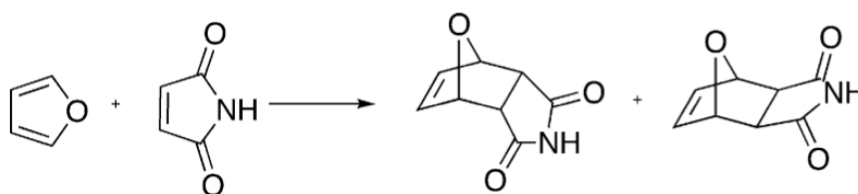


Figure 3-6 Diels-Alder reaction between furan and maleimide¹⁵ (Chen, X., *Science*, 2002)

In 2008, Park et al.^{45,46} utilized the DA reaction to incorporate healing functionality in a novel polymer derived from cyclopentadiene and characterized this derivative both as a bulk matrix and as the matrix in a carbon fiber composite. Later, Murphy et al.⁴⁷ developed the highly cross-linked polymeric materials for healing property using thermally reversible Diels-Alder (r-DA) cycloaddition reaction. The remendable polymers were synthesized by replacing furan-maleimide pair with a single monomer, dicyclopentadiene

(DCPD) core unit. Both diene and dienophile were used for DCPD moiety in the thermally reversible DA cycloaddition reaction. The healing property shows that the strength is enhanced by the crosslinking of the dieophilic DA dimer. Fracture tests showed 46% of healing efficiency at 120 °C for 20 h under an argon atmosphere.

In 2011, Yoshie et al.¹⁴ developed a self-healing polymer with high thermal stability based on the DA reaction between anthracene and maleimide. The material, PEAA₂M₃, is prepared by the DA reaction of anthryl-telechelic poly(ethylene adipate) (PEAA₂) and tris-maleimide (M₃) (Figure 3-7). The thermal dissociation of the DA reaction occurs only at very high temperatures which an organic polymer degrades significantly. Therefore, thermal stability is successfully combined with self-healing ability in PEAA₂M₃.

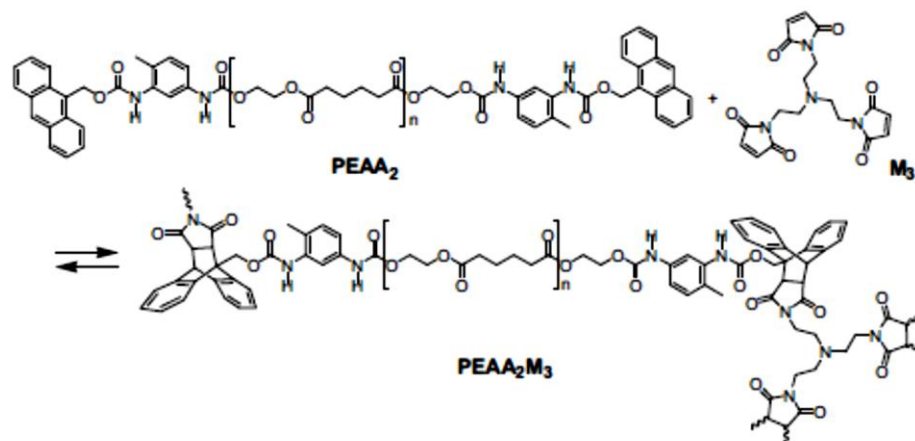


Figure 3-7 Diels-Alder reaction between anthryl-telechelic poly(ethylene adipate) and a tris-maleimide¹⁴ (Yoshie, N., *Polymer*, 2011)

3.1.1.5 Ionomeric self-healing materials

Ionomeric copolymers have ionic segments that can form clusters and act as reversible crosslinks. These clusters can be activated by external stimuli such as temperature or ultraviolet irradiation. Because the cluster formation is reversible, multiple local healing can be applicable to repair the damage. Kalista et al.²¹ prepared poly(ethylene-*co*-methacrylic acid) copolymers with ionic segments and investigated self-healing behavior by ballistic puncture test. The trigger for self-healing in these cases was initiated by heating during projectile damage.

3.1.1.6 Supramolecular self-healing materials

The supramolecular self-healing requires high mobility of molecular chains. The healing process needs to form reversible covalent bonds or non-covalent supramolecular linkages in a polymer. Polymers can be designed strong end- and/or side-group associations via multiple complementary, i.e., reversible hydrogen bonds and π - π stacking interactions.

Chen et al.⁴⁸ synthesized a thermoplastic elastomer containing polystyrene backbone as the hard phase and polyacrylate amide (PA-amide) brushes as the soft phase. Hydrogen-bonding on supramolecular assembly of the PA-amide brushes should lead to the formation of a dynamic microphase-separated nanostructure that can be reversibly broken and reformed, affording spontaneous self-healing behavior (Figure 3-8). The self-healing behavior depends on the amount of PA-amide brush chains and brush repeat unit.

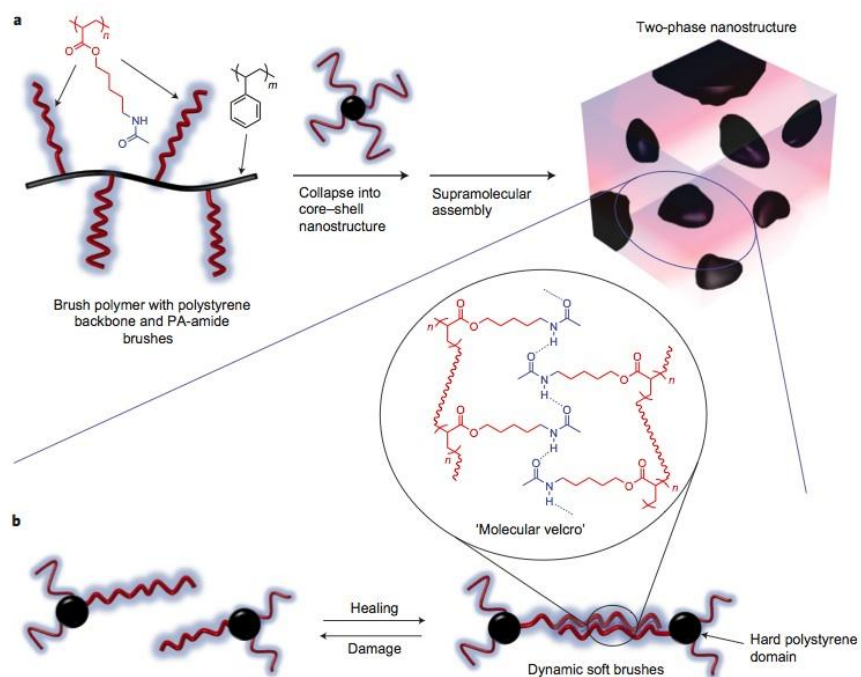


Figure 3-8 Schematic concepts for the multiphase self-healing brush polymer system. (a) The hydrogen-bonding brush polymer self-assembles into two-phase nanostructure morphology during processing. (b) Although mechanically robust, the supramolecular connections between soft brushes can rupture reversibly under stress, in contrast to conventional thermoplastic elastomer systems, where rupture of the purely covalent interdomain connections is irreversible.⁴⁸ (Chen, Y., *Nature Chemistry*, 2012)

3.1.1.7 Self-healing via molecular diffusion

The molecular interdiffusion can occur for both thermoplastic and thermoset resins, which can be used for self-healing. Beyond T_g , the polymer-polymer interface gradually vanishes and the mechanical strength at the initial interface increases by attaching two pieces of identical or even miscible polymers into contact. Thus, the polymer matrix is actually healed just due to molecular diffusion through the polymer-polymer interface.³

Wool and O'Connor systematically studied the phenomena.^{49,2} They pointed out that the healing process through surface rearrangement, surface approaching, wetting, diffusion and randomization (Figure 3-9). The leading role of the worm-like displacement of a chain in the entangle polymer melts and gels is assigned to the mobile chain end.

Mikos and Peppas⁵⁰ reported the molecular theory for the polymer fracture properties using structural and entanglement characteristics of macromolecules. Brown et al.³² studied correlation between the interdiffusion of the aromatic polyimide and the adhesion. They found that the diffusion distance, at least 200 nm, is requested for full bond strength.

Phadke et al.⁵¹ synthesized the acryoyl-6-aminocaproic acid hydrogels as self-healing polymers with dangling hydrocarbon side chains using amide and carboxylic functional groups. The healing behavior can be controlled reversibly by pH change.

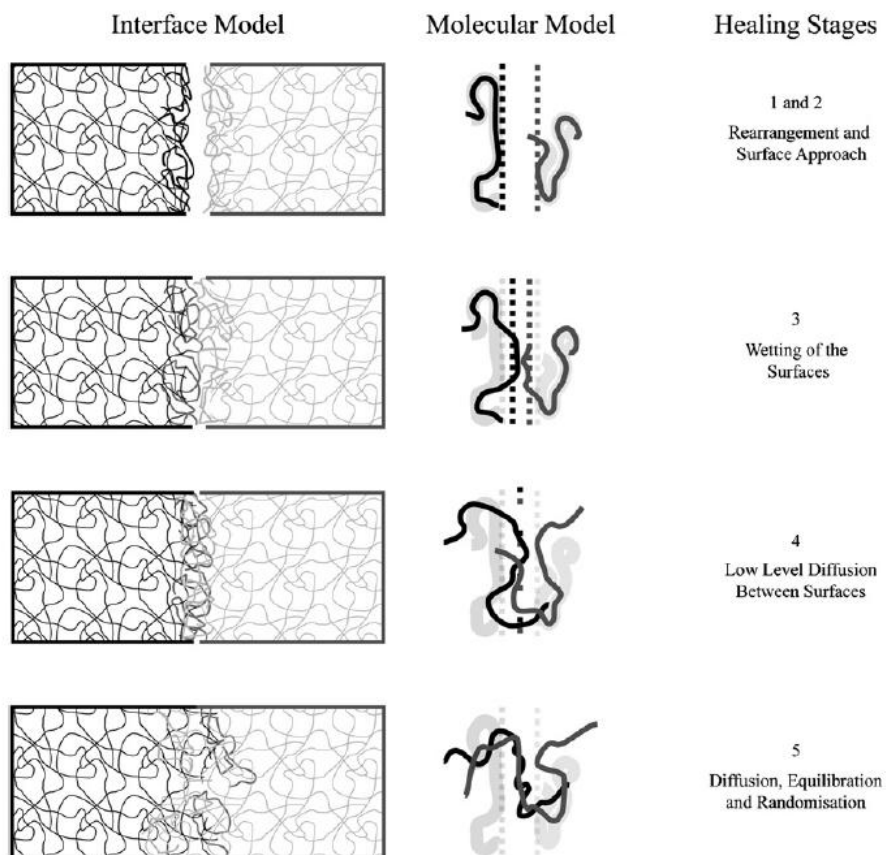


Figure 3-9 Mechanisms involved in self-healing via molecular interdiffusion^{2,49} (Murphy, E. B., *Prog Polym Sci*, 2010, Wool, R. P., *J Appl Phys*, 1981)

Surface rearrangement

When damaged surfaces are created by fracture or fatigue, one should consider the roughness or topography of the surface and how it changes with time, temperature and pressure. For fractured polymers, rearrangement of polymer molecules affects the rate of crack healing. Distributions of chain ends near the surface can change as molecules diffuse into the bulk. If the chain ends are needed for reaction with the fluid, they could be designed to preferentially migrate to the surface using a large free volume of the chain

ends.

Since the surface rearrangements can occur at room temperature, an important role of the healing fluid could enhance the molecular mobility at the surfaces and facilitate the other stages of healing. The dynamics of the surface-layer rearrangement is similar to that in some bulk processes. However, the surface molecules should have greater mobility due to higher degree of freedom.

Surface approach and wetting

This stage is the most critical for self-healing process. Simply, no healing occurs if the surfaces are not attached together. Thus, any debris left over from the damage process pry the surface apart to prevent surface approach and terminate the self-healing process. When the damaged surfaces approach, they need to wet together and form an interface before the interdiffusion process.

Wetting occurs in a time-dependent fashion at the interface. A brief phenomenological description of wetting was provided by Wool.⁴⁹ With surface roughness, good contact and wetting are not achieved instantaneously at all locations. Typically, wetted “pools” appear at random at the interface and propagate radially until coalescence and complete wetting are obtained. This problem has been treated as a two-dimensional nucleation and growth process such that the fractional wetted area, $W(t)$, is given empirically as:

$$W(t) = 1 - e^{(-kt^m)} \quad (3-6)$$

where k and m are constants depending on the nucleation function and radial-spreading rates. This function predicts that a perfect wetting will occur eventually, but this is not the

case depending on how the surfaces are permitted to approach together.

Diffusion stage

The diffusion stage is the most important step for restoring the mechanical properties. The interpenetration of polymers and polymer entanglement occur at this stage.

Kim and Wool⁵² proposed a microscopic model for the last two decades on the basis of reptation model that describes longitudinal chain diffusion responsible for crack healing. Furthermore, Jud and Kausch⁵³ studied the effect of molecular weight on the crack healing behavior of poly(methyl methacrylate) (PMMA) and PMMA–poly(methoxy ethylacrylate) copolymers. They observed crack healing for the samples heated above T_g under slight pressure. It was found that 5 °C higher than T_g and a healing time over 1 min were required for the healing. The establishment of mechanical strength should be attributed to the interdiffusion of chains and formation of entanglements for the glassy polymers.⁵⁴

Healing of thermosets occurs by rearranging partial chains at ambient or elevated temperatures. Chain rearrangement occurring at ambient temperature heals cracks or scratches via interdiffusion of dangling chains^{28,29} or chain slippage in the polymer network. Yamaguchi et al.²⁸ described the self-healing thermoset based on molecular interdiffusion of dangling chains. These self-healing polymers consisted of a polyurethane network prepared using a tri-functional polyisocyanate, polyester-diol and a dibutyl-tin-dilaurate as a catalyst. The authors varied reagent ratios to manipulate the crosslink density and therefore the number of dangling chain ends. Healing was assessed visually by checking slit closure of cut specimens over time. Using the appropriate reagent

ratios enabled healing to occur rapidly (10 min), once the cut surfaces were in contact together. It was concluded that a weak gel (just beyond the critical point) is capable of healing via the entanglement of dangling chain ends (Figure 3-10).

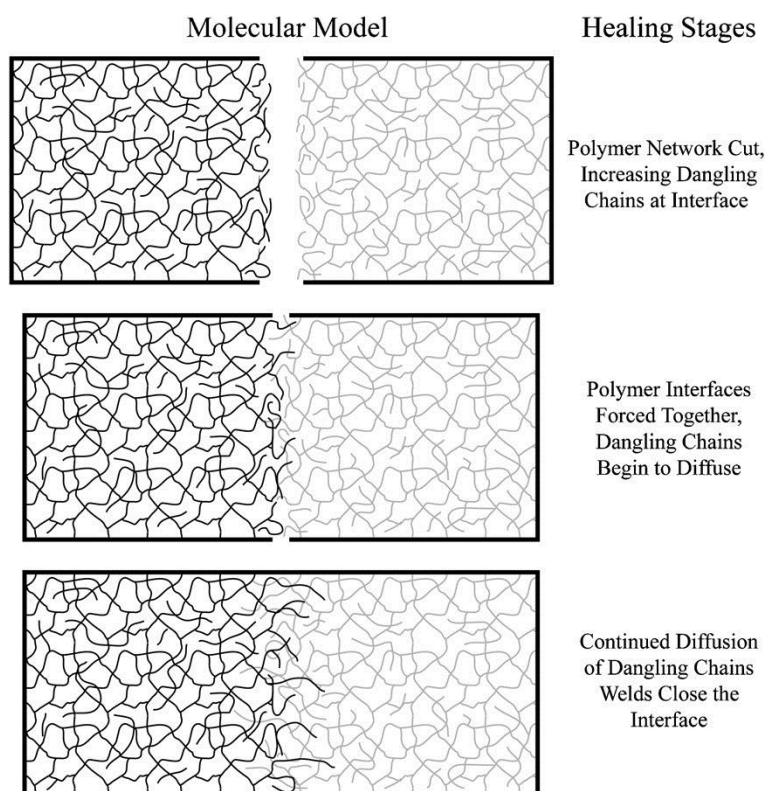


Figure 3-10 Healing of a crosslinked network via dangling chain entanglement.³ (Wu, D. Y., *Prog Appl Sci*, 2008)

According to their previous work, the polyurethane network having a lot of dangling chains show a good self-healing behavior at room temperature in a short time. Numerous kinds of polyurethanes having different degree of crosslink points are employed as rubbery polymers. However, the network polymer shows the low modulus and low strength due to low density of crosslinks. Furthermore, it is unrecyclable because of the permanent network. At present, thermoplastic nature is important to widen the application.

PVB, as one of thermoplastics, is employed in this study for self-healing ability at the temperature below T_g .

3.1.2 Characterization methods

3.1.2.1 Attenuated total reflectance fourier transform infrared spectroscopy (ATR-FTIR)

The main distinction of ATR-FTIR from other spectroscopic techniques is that it depends on total internal reflection and attenuation of a total reflection. ATR-FTIR can be used for either quantitative or qualitative analysis. In qualitative analysis, ATR-FTIR identifies chemical bonds in a molecule by producing an infrared absorption spectrum. It is an effective analytical instrument for detecting functional groups and characterizing covalent bonding information. The quantitative analysis is performed by the measurement of the intensity with incident IR beam. It determines the size of the peaks in the spectrum and gives direct signal of the amount of material present.

In ATR-FTIR, the beam is directed toward a crystal of a high refractive index (Figure 3-11). IR beam reflects from internal surface of a crystal and creates evanescent waves. After the absorption by the sample, some energy returns to a detector. The signal is detected and converted by Fourier transform to provide the spectrum.

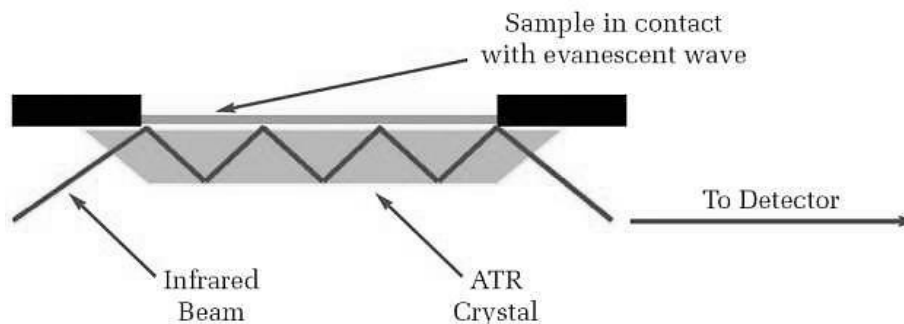


Figure 3-11 A schematic illustration of internal reflections through a high refractive index medium, for example, ZnSe, used as the internal reflection element.⁵⁵ At each reflection, an evanescent wave is produced that decays exponentially into the medium above.

ATR-FTIR operates on a basic principle of a Snell's law:

$$n_1 \sin \theta_1 = n_2 \sin \theta_2 \quad (3-7)$$

where n_1 is the refractive index of an optically dense medium of a high refractive index, n_2 is that of a medium, θ_1 is an angle of an incident light and θ_2 is a refracted angle.

If n_1 is higher than n_2 and the angle of incidence is large, no light in the first medium will enter into the second medium. Therefore, the incident angle must be larger than the critical angle. Then, total internal reflection is observed. The infrared radiation interacts with the sample through a series of standing waves and gives evanescent waves at the surface of a material with a lower refractive index.⁵⁶ IR beam has huge probabilities to interact with the sample, which is known as *depth of penetration*. Depth of penetration (d_p) is defined as a required distance of the sample penetration by an evanescent wave for

electric field amplitude (intensity),⁵⁷ which is expressed as:

$$d_p = \frac{\lambda}{2\pi\sqrt{\sin^2 \theta - (n_2 - n_1)^2}} \quad (3-8)$$

where λ is the wavelength.

Each material has different penetration depth. For example, polymers and aqueous solutions have strongly absorbed medium. Therefore, they show small penetration depth and short path length for infrared absorption. At higher wavenumbers, the penetration depth and ATR intensities decrease in comparison to a transmission spectra.⁵⁷

3.1.2.2 X-ray photoelectron (XPS)

The XPS technique is used to investigate the chemistry at the surface of a sample. The electronic states of atoms below the surface of the sample are excited by photons with a specific energy. The electrons ejected from the surface are energy filtered via hemispherical analyzer. Then, the intensity for a defined energy is recorded by a detector. The resulting energy spectra exhibit the characteristic of the electronic state for atoms at the sample surface. The ejected electrons from depths more than 10 nm have a low possibility of leaving the surface without undergoing an energy loss incident. The energies of the photoelectric lines are well defined in terms of the binding energy of the electronic states of atoms. Further, the chemical environment of the atoms at the surface results in well defined energy shifts to the peak energies.

XPS is a quantitative technique; the number of electrons recorded for a given transition is proportional to the number of atoms at the surface. In practice, however, to produce accurate atomic concentrations from XPS spectra is not straight forward. The

precision of the intensities measured is not in doubt; that is intensities measured from similar samples are repeatable. The results are reported to be atomic concentrations for the elements at the surface. The XPS spectrum is a combination of the number of electrons leaving the sample surface and the ability of the instrumentation to record these electrons.

The efficiency of emitted electrons is recorded dependent on the kinetic energy of the electrons. As a result, the best way to compare XPS intensities is via percentage atomic concentrations. The ratio of the intensities is divided by the total intensity of electrons in the measurement. The ratio of C1s and O1s is defined as:

$$C = \frac{\text{peak area of C1s} \times 0.278}{(\text{peak area of C1s} \times 0.278) + (\text{peak area of O1s} \times 0.78)} \quad (3-9)$$

$$O = \frac{\text{peak area of O1s} \times 0.78}{(\text{peak area of C1s} \times 0.278) + (\text{peak area of O1s} \times 0.78)} \quad (3-10)$$

3.2 Materials

A polymer used in this study was a commercially available terpolymer composed of vinyl butyral (79 wt%), vinyl alcohol (19 wt%), and vinyl acetate (2 wt%) (Denki Kagaku Kogyo, Japan, Denka PVB 4000-2). In this study, the sample is denoted as PVB (PVB1 in the previous chapter). The absolute molecular weight and its distribution were evaluated by simultaneous measurements of multi-angle light scattering (Wyatt Technology, Dawn Heleos) and gel permeation chromatography (Tosoh, HLC-8120GPC) with TSKgel GMHHR-H (Tosoh). Tetrahydrofuran was used as an eluent at a flow rate of 1.0 mL/min at 40 °C, and the sample concentration was 1.0 mg/mL. The number- and weight-average molecular weights of PVB were $M_n = 5.1 \times 10^4$ and $M_w = 1.1 \times 10^5$. Furthermore, PVB has no crystalline phase with T_g of 76 °C, which was confirmed by the DSC measurement at a heating rate of 10 °C/min.

3.2.1 Sample Preparation

After being dried at 60 °C for 6 hrs, the powders were compressed into flat sheets with various thicknesses by a compression-molding machine (Tester Sangyo, Japan, Table-type test-press) at 190 °C under 10 MPa for 3 min. Then, the samples were rapidly cooled down in an ice-water bath.

3.3 Measurements

The healing behavior was evaluated using the sample sheets cut by a razor blade. The initial depth of the scar was approximately 40 μm . The sample was annealed at 25 $^{\circ}\text{C}$ under 50 % of relative humidity (50 %RH) for various periods up to 1 year and 8 months. The effect of humidity on healing behavior was studied by exposure to annealing operation with two levels of relative humidity, i.e., 10 %RH and 95 %RH, for 8 hrs. The annealing temperature was controlled at $T_g - 20$ $^{\circ}\text{C}$ (56 $^{\circ}\text{C}$), in which T_g was defined as the peak temperature of loss tangent $\tan \delta$ at 10 Hz.

The sample surface was observed by a stereomicroscope (Leica, Japan, Leica S6E) before and after the annealing procedure. Furthermore, the depths of the scratches were evaluated by a roughness tester (Time, Japan, TR200) to calculate the healing efficiency H_E defined as follows;

$$H_E (\%) = \frac{D_i - D(t)}{D_i} \times 100 \quad (3-11)$$

where D_i is the initial depth of the applied scar and $D(t)$ is that after t hours.

The sample surface was characterized by attenuated total reflectance Fourier-transform infrared spectroscopy (ATR-FTIR) (Perkin Elmer, UK, Spectrum 100 FT-IR spectrometer) at room temperature. The KRS-5 and Germanium were used as ATR crystals. The spectra were recorded in the mid-infrared region (4000 – 600 cm^{-1}). Prior to the measurements, the sample was kept in an incubator at 25 $^{\circ}\text{C}$ under vacuum for 1 day.

The surface functional groups were also characterized by X-ray photoelectron spectroscopy (XPS) (Kratos, UK, Kratos AXIS Ultra DLD instrument) using a monochromatic Al K α X-ray source at 1486.6 eV and operated at 15 kV and 10 mA with a base pressure in the XPS analysis chamber of 6.67×10^{-6} Pa. High resolution spectra (C1s) were acquired using a pass energy of 20 eV and 0.1 eV energy steps. All binding energies (BEs) were referenced to the hydrocarbon C1s peak at 284.5 eV. The samples were kept in a humidic chamber at 25 °C under vacuum for 2 days before the measurement. The spectra were deconvoluted using the Kratos's VISION software.

The water content was evaluated using a moisturemeter (Mitsubishi Chemical Corporation, Japan, CA-200) using the Karl Fischer method, in which the Karl Fischer reagent, which consists of iodine, sulfur dioxide, a base and a solvent, reacts quantitatively and selectively with water. The square films with 10 mm in both width and length were used for the measurements. The films were kept in a humidic chamber at 25 °C under 50 %RH for 8 hrs before the measurement. The measurements were conducted at 180 °C under a nitrogen atmosphere at a flow rate of 250 ml/min.

Temperature dependence of oscillatory tensile moduli such as storage modulus E' and loss modulus E'' was measured from -10 to 120 °C by a dynamic mechanical analyzer (UBM, Japan, E-4000) using rectangular specimens with 5 mm in width, 20 mm in length, and 300 μ m in thickness. The frequency was 10 Hz and the heating rate was 2 °C/min. Prior to the measurements, the samples were kept at various conditions for 8 hrs; 25 °C under 50 %RH, 56 °C under 10 %RH and 56 °C under 95 %RH.

3.4 Results and discussion

The healing behavior at 25 °C under 50 %RH is exemplified as a function of the periods after cut in Figure 3-12. Apparently, the scar applied by a razor blade is healed to some extent, which is prominent for the sample with a long annealing time. The result demonstrates that the healing of the scar occurs even at room temperature for PVB (Figure 3-13), although the storage modulus at room temperature is around 1 GPa, i.e., glassy state. It indicates that the molecular motion is not fully prohibited even below T_g . The pronounced molecular motion at surface due to the excess free volume would be responsible for the good healing behavior as reported by Boiko using polystyrene.⁵⁸ In fact, Tanaka et al. demonstrated that the surface glass transition temperature T_g^s is lower than the bulk glass transition temperature T_g^b by lateral force microscopy.^{59,60} However, even considering the marked molecular motion at surface, the healing behavior of PVB should be noted, because other plastics with similar T_g , e.g., poly(lactic acid) and poly(ethylene terephthalate), do not show such a good healing behavior at room temperature. Therefore, another mechanism should be taken into consideration for the self-healing property.

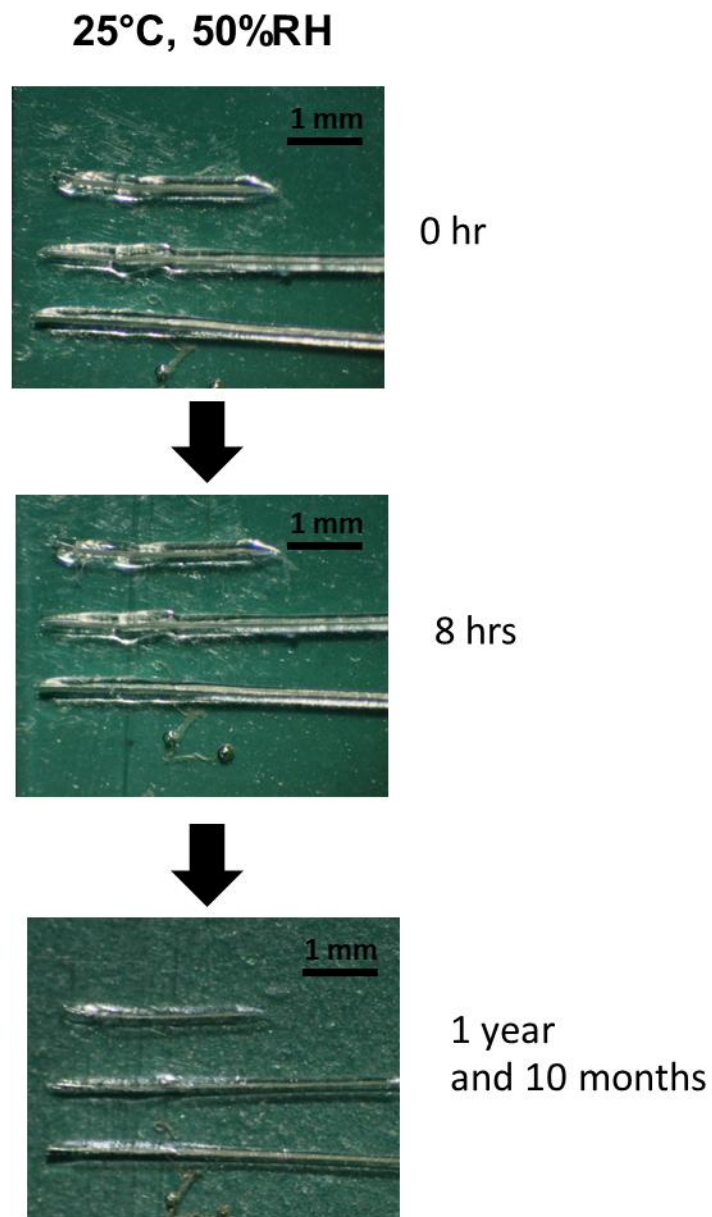


Figure 3-12 Healing behavior at 25 °C and 50 %RH

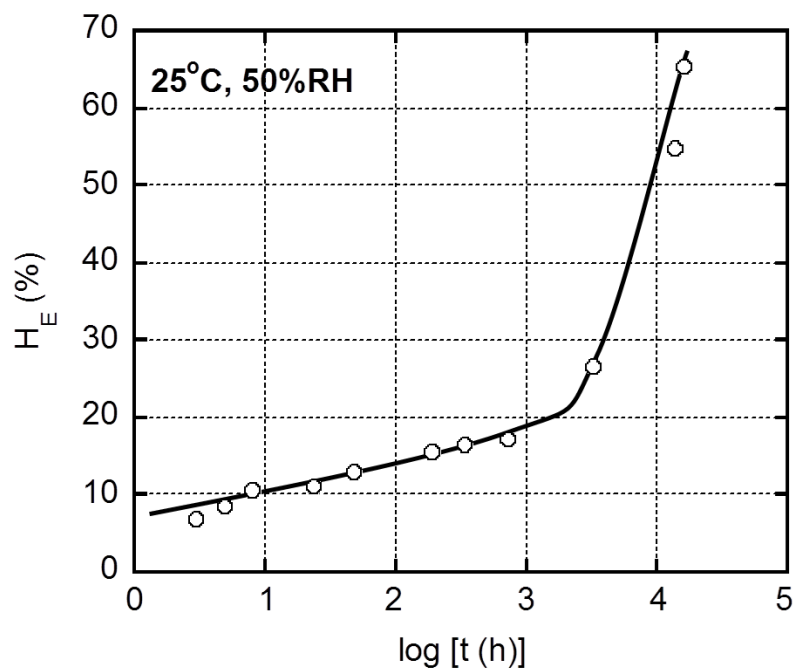


Figure 3-13 Growth of healing efficiency at 25°C and 50 %RH

To investigate functional groups of PVB at surface, ATR-FTIR analysis with different ATR crystals such as Germanium and KRS-5 was performed. The penetration depth of the IR beam d_p is provided by Equation (3-8). Because the refractive indices of Germanium and KRS-5 are 4.0 and 2.4, respectively, the information on the different penetration depth is obtained by using the plates.

As seen in Figure 3-14, the ATR-FTIR spectra show O-H stretching at 3,000- 3,600 cm^{-1} and C=O stretching at 1,600-1800 cm^{-1} . The CO peak is originated from vinyl acetate part in PVB, whereas the OH peak is from vinyl alcohol and/or the moisture interacting with PVB at surface. Following Equation (3-8), the penetration depth of IR beam into the sample at 3,430 cm^{-1} is calculated to be approximately 190 nm and 565 nm for Germanium

and KRS-5 crystals, respectively. Further, the absorption ratios of OH/CO are 105 and 14 for Germanium and KRS-5 crystals, respectively. It indicates that the surface has more hydroxyl group and/or the moisture.

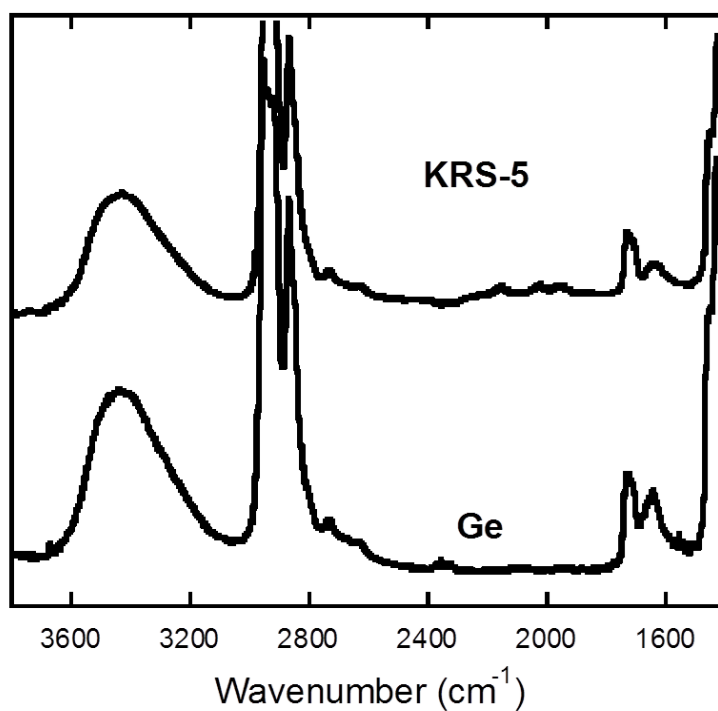


Figure 3-14 ATR-FTIR spectra measured by Ge crystal and KRS-5 crystal

Figure 3-15 shows the XPS spectrum of PVB. The sample was dried under vacuum for 2 days prior to the measurement, and the measurement was performed under vacuum condition. Therefore, the sample is free from the moisture. The XPS spectrum reveals that the functional groups at the surface are C-C, C-O, O-C-O, and C=O at binding energy of 284.5, 285.3, 286.6 and 287.5 eV, respectively (Figure 3-15 (a)).^{61,62} As seen in the figure, C-O peak is significantly strong, which is attributed to vinyl alcohol. The O1s spectrum detect the C=O and C-O functional groups at binding energy of 529.0 and 530.1 eV, respectively, which are originated from vinyl acetate and vinyl alcohol, respectively. Moreover, the O/C ratios of PVB calculated from XPS (Equations (3-9) and (3-10)) and actual value are 1.141 and 0.356, respectively. The results indicate that the hydrophilic groups in PVB prefer to be located on surface. The quantitative composition of PVB surface is shown in Table 3-1 with the actual composition in bulk. The results show that vinyl alcohol and vinyl acetate fractions at the surface are higher than those in the bulk, whereas vinyl butyral content is lower. This result demonstrates that C=O and C-O functional groups are localized on the surface. Therefore, the surface of PVB, having a large amount of the OH group, can absorb water in atmosphere. The water will act as a plasticizer for PVB.

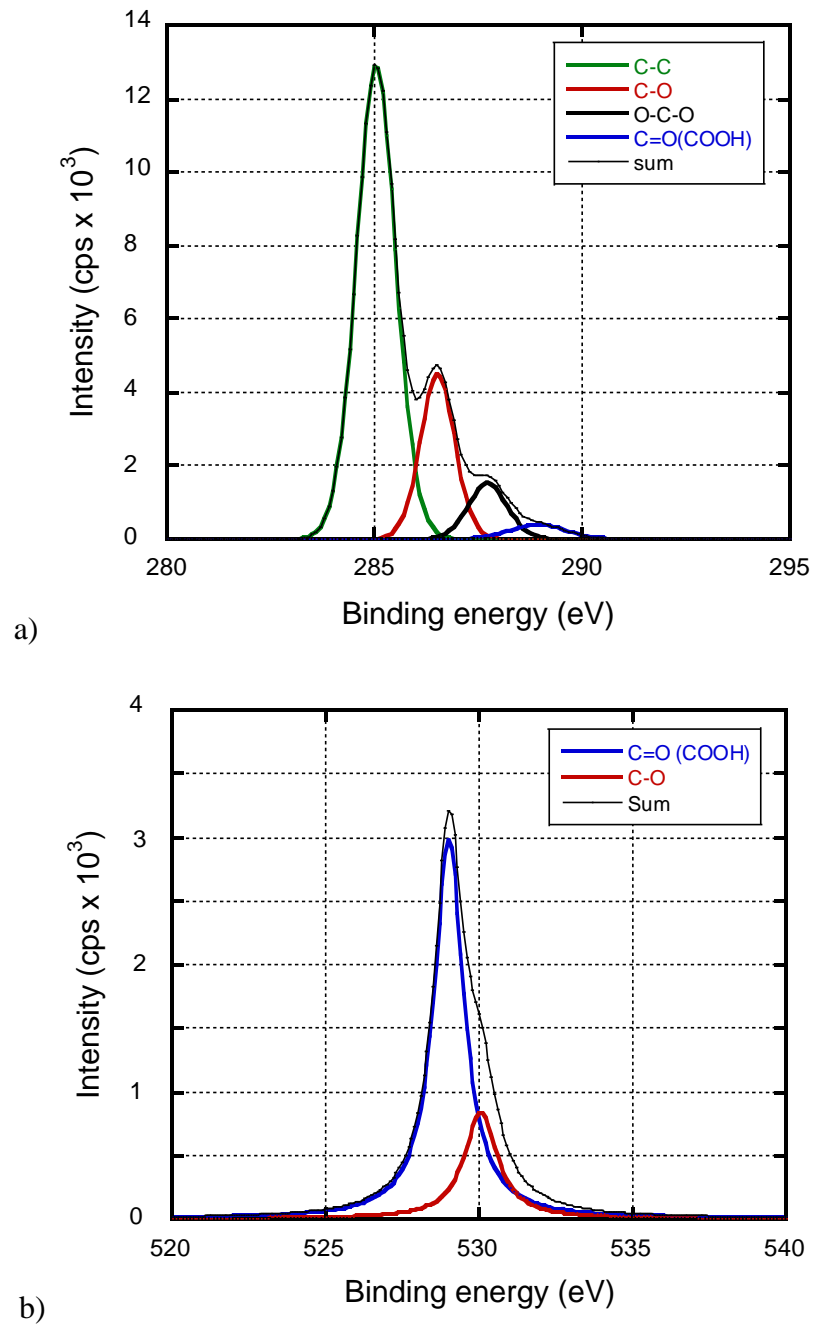


Figure 3-15 XPS spectra of PVB of (a) C1s and (b) O1s

Table 3-1 Surface composition of PVB

	Actual values in bulk (wt%)	Analytical results at surface (wt%)
Vinyl butyral (VB)	79	61
Vinyl alcohol (VA)	19	28
Vinyl acetate (VAc)	2	11

The water content per unit area of the films with various thicknesses is measured by the Karl Fischer technique. The samples were kept in an incubator at 25 °C under 50 %RH for 8 hrs. At first, it was confirmed that the value after 8 hrs is identical to the equilibrium one (Figure 3-16).

The measured water content is plotted as a function of the film thickness. As shown in Figure 3-17, the water content per unit area increases with increasing the thickness. This is reasonable because the sample volume increases with the thickness. Furthermore, the results suggest that the surface contains additional water, which can be evaluated by the intercept of y-axis. The result corresponds with the ATR-FTIR spectra. It is also found from the slope that the water content inside of the sample specimen is 5.32 wt%. The results correspond with ATR-FTIR spectrum.

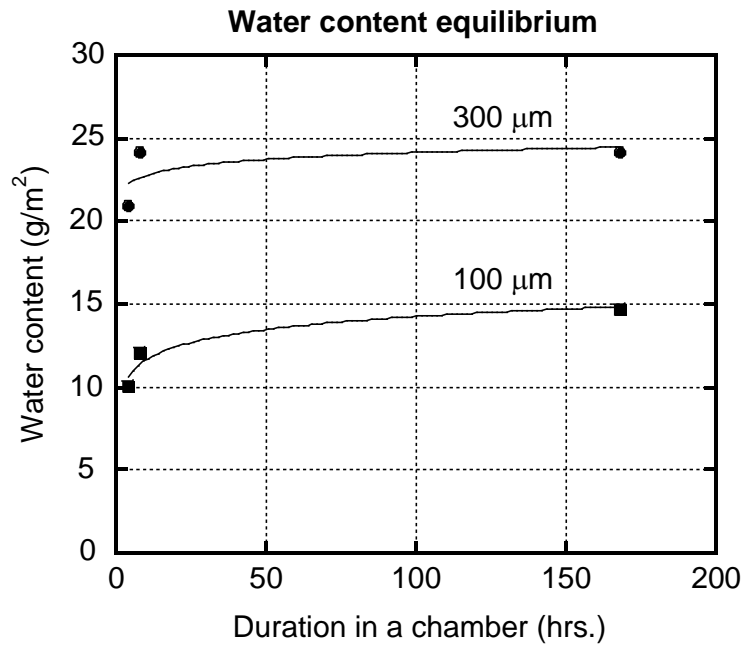


Figure 3-16 Growth of water content per unit area of the film in the chamber controlled at 25 °C and 50 %RH. The film thicknesses were 100 and 300 µm

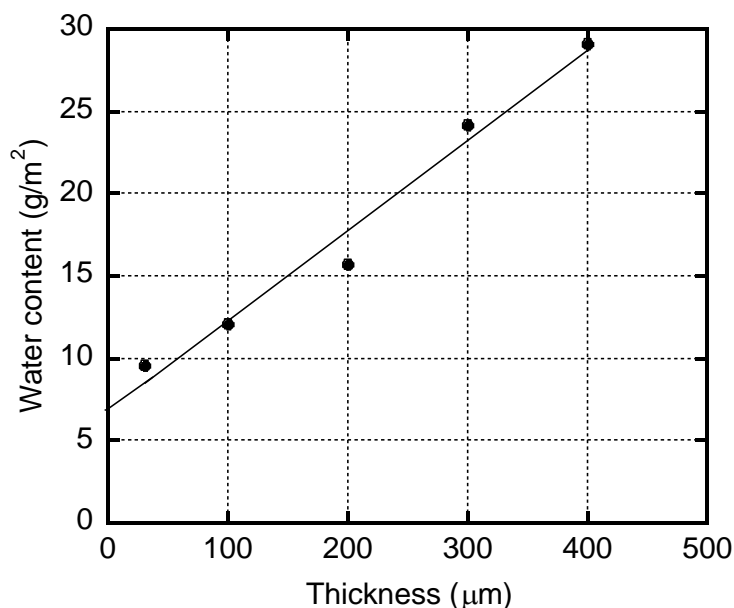


Figure 3-17 Water content per unit area of the films kept in a chamber at 25 °C and 50 %RH for 8 hrs.

The self-healing behavior in this study is ascribed to the marked mobility of polymer chains at surface. Therefore, the information on the rheological properties at surface is significantly important for the material design. Although AFM is known to be sensitive to the surface modulus, it is lack of the quantitative characterization. Therefore, in this study, the temperature dependence of the dynamic mechanical properties is evaluated using films with various thicknesses. Of course, the contribution of the surface to the dynamic mechanical spectra increases with decreasing the film thickness.

The results are shown in Figure 3-18. All samples were kept in an incubator at 25 °C under 50 %RH for 8 hrs before the measurement. It is found that thin films show marked double peaks in the E' and $\tan \delta$ curves. As decreasing the thickness, the peak at low temperature shifts to lower temperature. In contrast, the peak at high temperature is independent of the film thickness, indicating that the peak at high temperature is ascribed

to T_g of the bulk. Thinner films also exhibit the pronounced E' drop at lower temperature, which corresponds to the marked E'' peak. These results demonstrates that the surface region shows marked molecular motion presumably owing to the plasticizing effect of water absorbed on the hydrophilic groups at the surface.

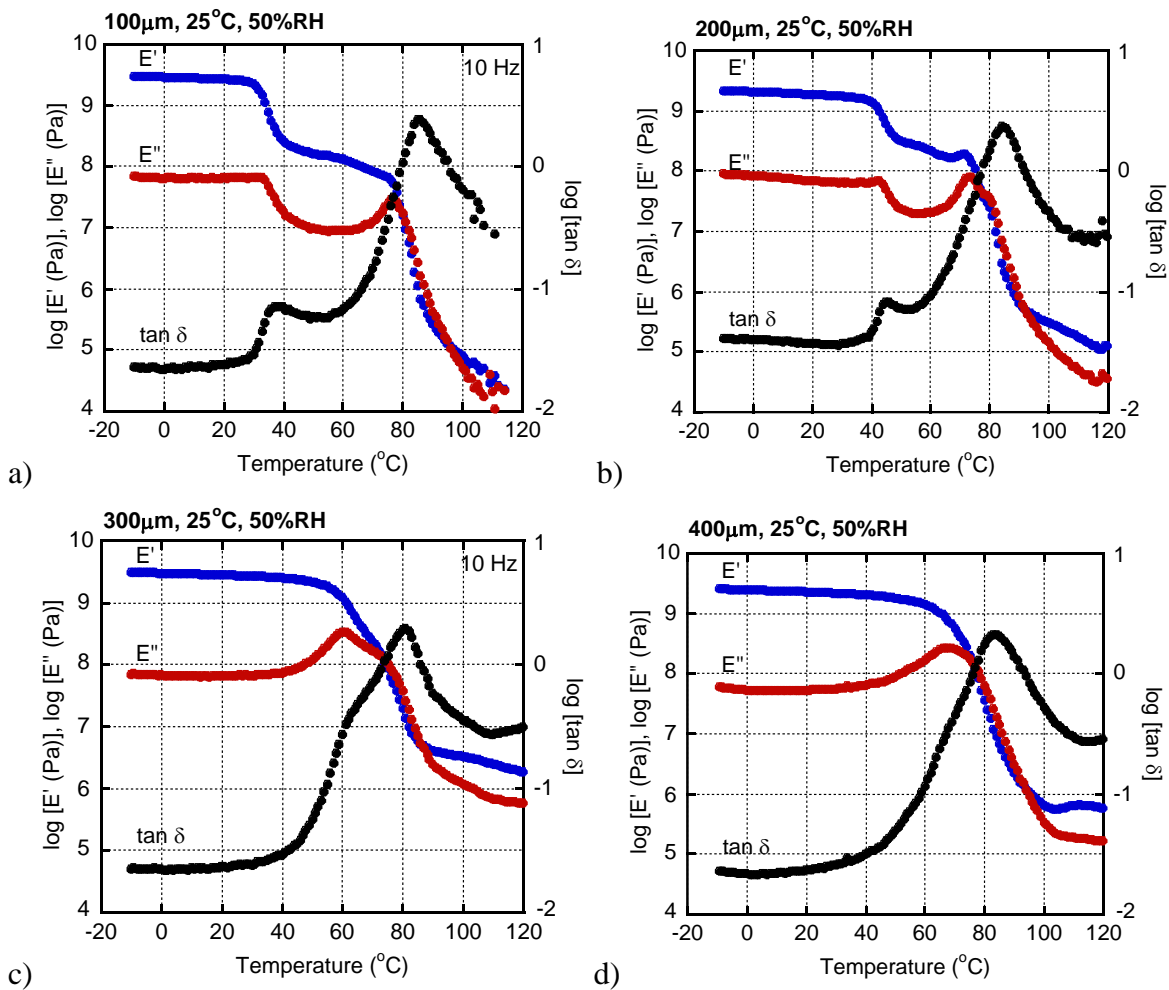


Figure 3-18 Temperature dependence of (blue) tensile storage modulus E' , (red) loss modulus E'' and (black) loss tangent $\tan \delta$ at 10 Hz for the sample kept at 25 °C and 50 %RH with various thicknesses; (a) 100 μm , (b) 200 μm , (c) 300 μm and (d) 400 μm

Further measurements of dynamic mechanical analysis are performed. In order to

understand the effect of humidity on the molecular motion, Figure 3-19 shows the temperature dependence of dynamic tensile modulus is measured using the samples kept in the different humidity condition. The film thickness is 300 μm . The samples were left in an incubator at 25 $^{\circ}\text{C}$ for 8 hours with three conditions; under vacuum (i.e., 0 %RH), 50 %RH and 100%RH (dipped in water). The E'' and $\tan \delta$ curves around T_g for the samples kept at 50 %RH and 100%RH show ambiguous double peaks; one is located at 80 $^{\circ}\text{C}$ and the other is at 60 $^{\circ}\text{C}$ for 50 %RH and 45 $^{\circ}\text{C}$ for 100 %RH. As compared with the figures, the curves in the high temperature range from 75 to 85 $^{\circ}\text{C}$ are the almost similar irrespective of the humidity. This indicates that the dynamic mechanical properties for the inside of the samples, which has a small amount of water, are not affected by the humidity greatly. In contrast, the peak located at the lower temperature is shifted to low temperature at high humidity condition, because of the plasticizing effect of water. The moisture-plasticized surface is responsible for the marked self-healing behavior even at room temperature.

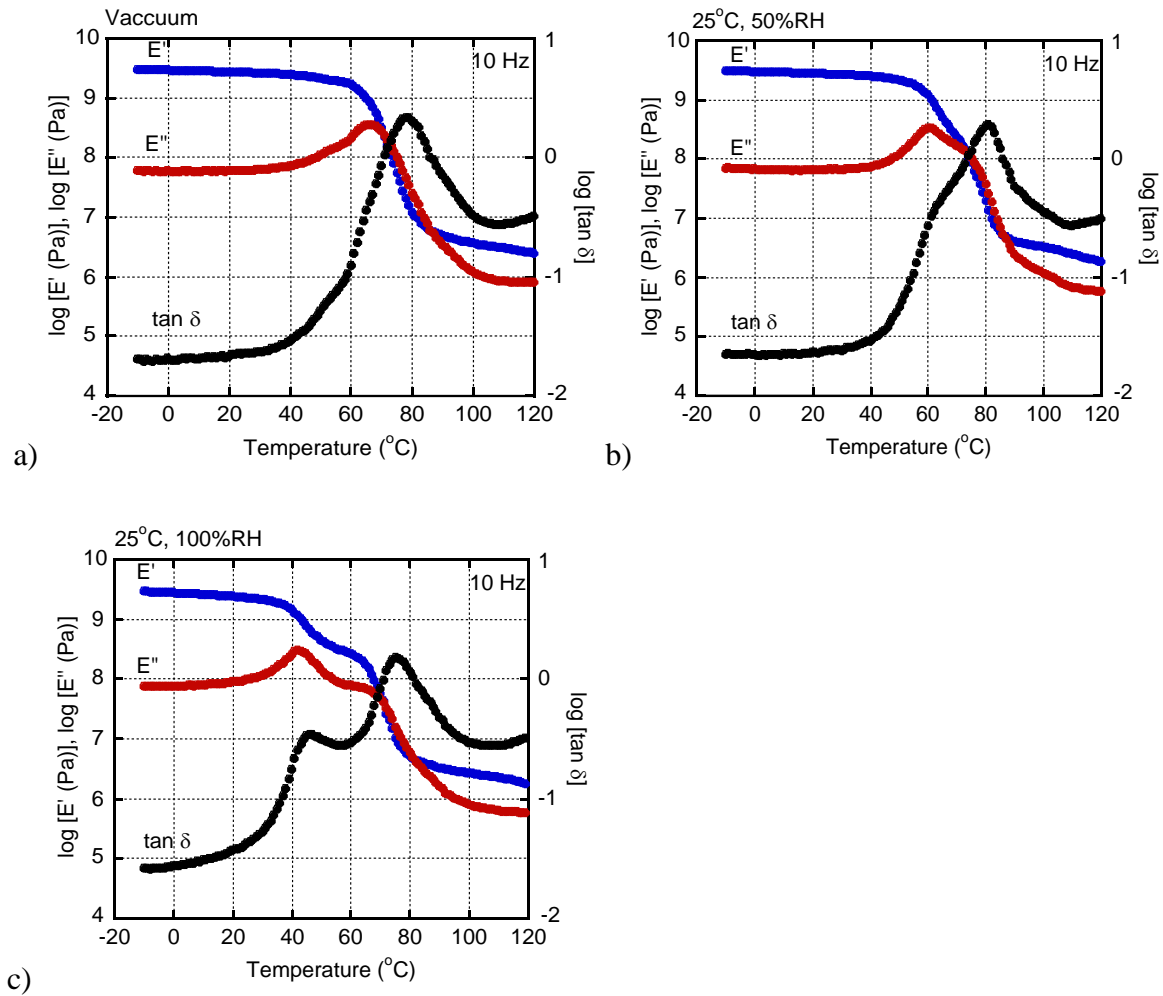


Figure 3-19 Temperature dependence of (blue) tensile storage modulus E' , (red) loss modulus E'' and (black) loss tangent $\tan \delta$ at 10 Hz for the sample kept (a) under vacuum, (b) at 25 $^{\circ}\text{C}$ and 50 %RH and (c) at 25 $^{\circ}\text{C}$ and 100 %RH for the films with of 300 μm thickness

For the better understanding of the effect of humidity, the healing behavior was investigated at different relative humidity, i.e., 10 %RH and 95 %RH, at 20 °C below T_g (56 °C). As shown in Figure 3-20, the healing of the scar occurs in a short time at high humidity. The healing efficiency is around 90% in an hour (Figure 3-21). In contrast, the healing occurs slowly at low humidity. The healing efficiency after 8 hrs is about 45%. Moreover, the temperature dependence of dynamic loss modulus of 95 %RH shows double peaks at 80 °C and 50 °C (Figure 3-22). The low T_g at surface by the plasticizing effect of absorbed water enhances the mobility of molecular chains. The results directly demonstrate that the water absorbed on the surface by the localization of vinyl alcohol plays an important role on the self-healing behavior.

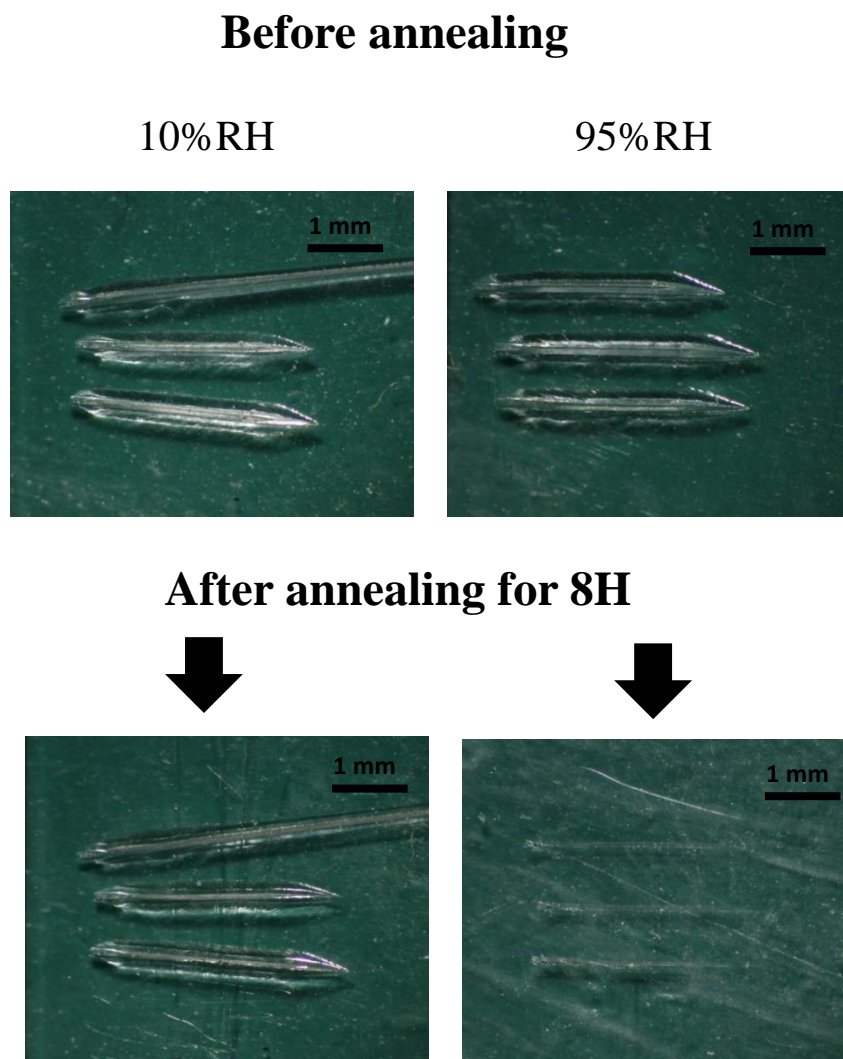


Figure 3-20 Healing behavior at 56°C of annealing temperatures under (left) 10 %RH and (right) 95 %RH for 8 hrs.

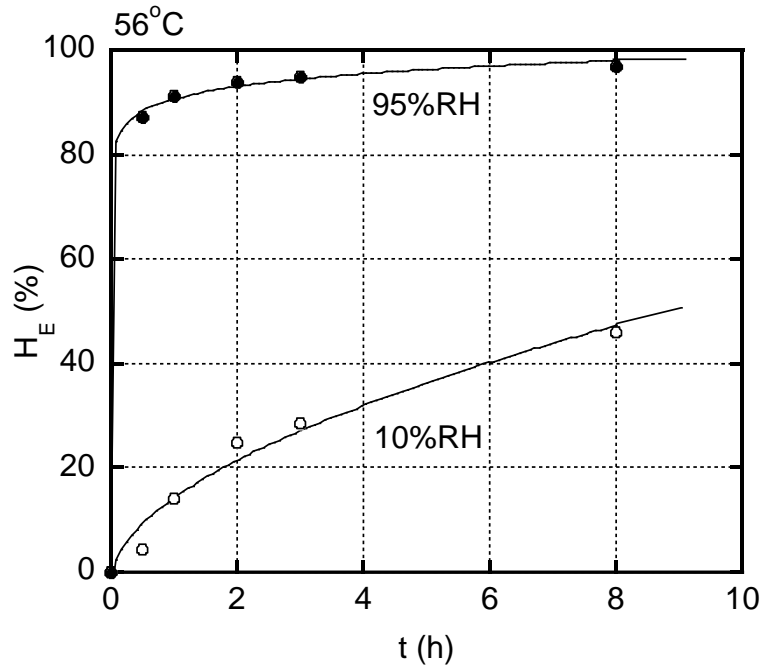


Figure 3-21 Healing efficiency at 56°C; (open) 10 %RH and (closed) 95 %RH

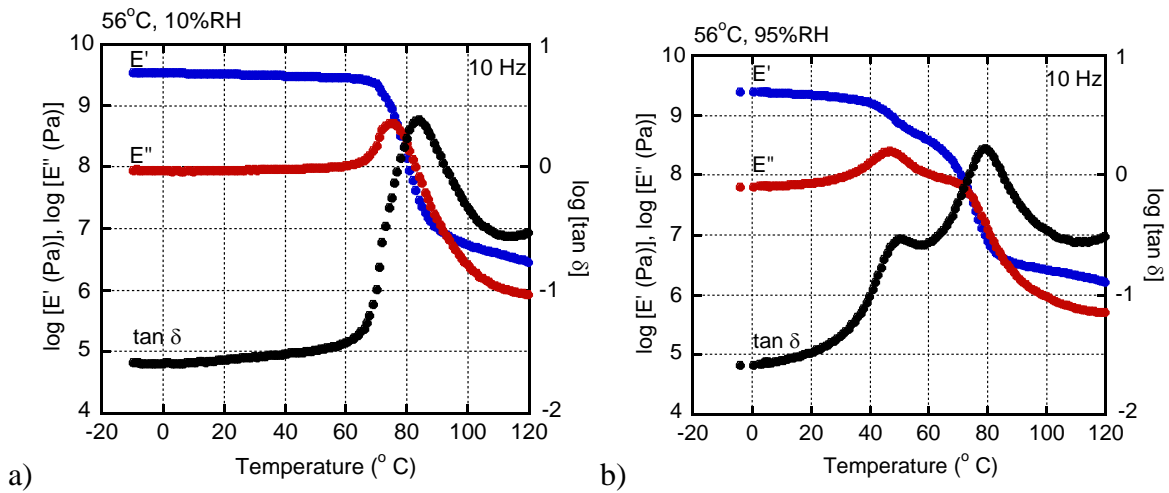


Figure 3-22 Temperature dependence of (blue) tensile storage modulus E' , (red) loss modulus E'' and (black) loss tangent $\tan \delta$ at 10 Hz for the sample kept (a) at 56°C and 10 %RH and (b) at 56°C and 95 %RH.

Moreover, the healing efficiency in water is also investigated at room temperature.

The scar was applied by roughness tester and razor blade, showed in Figure 3-23. The initial depth of scar is around 2.4 μm and 18.5 μm for roughness tester and razor blade, respectively. The healing behavior of scar applied by roughness tester shows that the healing of scar is almost completely healed after annealing for a month. In case of scar applied by razor blade, the result shows healing efficiency around 53% and 65% for 14 days and 30 days of annealing time, respectively. These indicated that the humidity can be enhanced the self-healing behavior even at room temperature. Considering the actual weather, PVB can heal its scratches at rainy days and exhibits as a plastic glass with high T_g at sunny days. This can be concluded that self-healing products of PVB are appropriate to be used for outdoor goods.

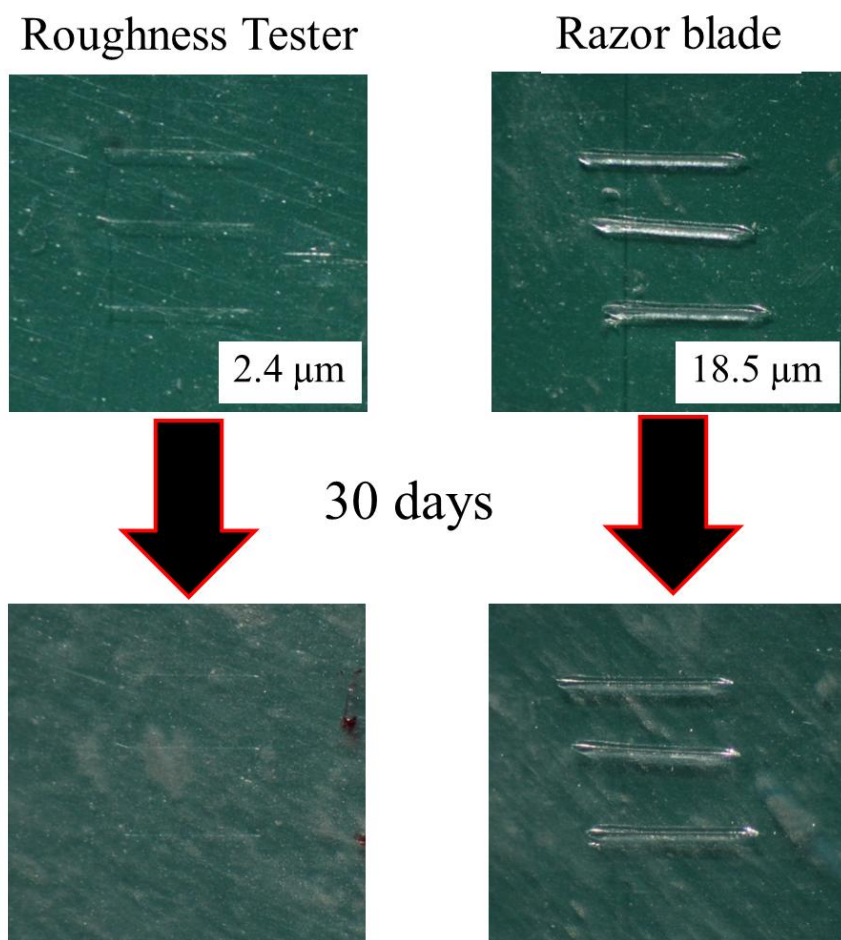


Figure 3-23 Healing behavior at 25°C of annealing temperatures in water; the scar applied by (left) roughness tester and (right) razor blade for a month.

3.5 Conclusion

PVB shows good self-healing behavior even below T_g without chemical reactions. Although T_g of PVB is around 76 °C, the depth of the applied scar is healed up to 50% for 1 year and 8 months at 25 °C. The high level of healing efficiency is attributed to marked molecular motion of polymer chain at the surface, which is confirmed by XPS. At the surface, it contains a large amount of water owing to the surface localization of vinyl alcohol and vinyl acetate. The water acts as a plasticizer, which is also confirmed by the dynamic mechanical properties. T_g at surface decreases with decreasing of thickness which cause from the plasticizing effect of water absorbed on the surface. Consequently, the healing efficiency is extremely enhanced at the high humidity condition because of the marked mobility of polymer chains on surface.

According to the healing process, the wetting appears on the surface caused by the water absorbed with vinyl alcohol and vinyl acetate moieties. Then, the molecular chains are moving in diffusion and randomization steps. Therefore, the healing of an applied scar occurs.

References

1. Bergman, S. D.; Wudl, F., Mendable Polymers. *J Mater Chem* **2008**, *18*(1), 41-62.
2. Wool, R. P., Self-healing Materials: a review. *Soft Matter* **2008**, *4*(3), 400-418.
3. Wu, D. Y.; Meure, S.; Solomon, D., Self-healing Polymeric Materials: A review of Recent Developments. *Prog Polym Sci* **2008**, *33*, 479-522.
4. Murphy, E. B.; Wudl, F., The World of Smart Healable Materials. *Prog Polym Sci* **2010**, *35*, 223-251.
5. Jones, A. S.; Rule, J. D.; Moore, J. S.; Sottos, N. R.; White, S. R., Life Extension of Self-healing Polymers with Rapidly Growing Fatigue Cracks. *J R Soc Interface* **2007**, *4*, 395-403.
6. Liu, X.; Sheng, X.; Lee, J. K.; Kessler, M. R.; Kim, J. S., Rheokinetic Evaluation of Self-healing Agents Polymerized by Grubbs Catalyst Embedded in Various Thermosetting Systems. *Compos Sci Technol* **2009**, *69*, 2102-2107.
7. Nesterova, T.; Dam-Johansen, K.; Pedersen, L. T.; Kiil, S., Microcapsule-based Self-healing Anticorrosive Coatings: Capsule Size, Coating Formulation, and Exposure Testing. *Prog Org Coat* **2012**, *75*, 309-318.
8. Patel, A. J.; Sottos, N. R.; Wetzel, E. D.; White, S. R., Autonomic Healing of Low-Velocity Impact Damage in Fiber-reinforced Composites. *Composites Part A* **2010**, *41*, 360-368.
9. White, S. R.; Sottos, N. R.; Geubelle, P. H.; Moore, J. S.; Kessler, M. R.; Sriram, S. R.; Brown, E. N.; Viswanathan, S., Autonomic Healing of Polymer Composites. *Nature* **2001**, *409*, 794-797.

10. Dry, C., Procedures Developed for Self-repair of Polymer Matrix Composite Materials. *Compos Struct* **1996**, *35*, 263-269.
11. Pingkarawat, K.; Wang, C. H.; Varley, R. J.; Mouritz, A. P., Self-healing of Delamination Fatigue Cracks in Carbon Fibre-epoxy Laminate using Mendable Thermoplastic. *J Mater Sci* **2012**, *47*, 4449-4456.
12. Williams, G.; Trask, R.; Bond, I., A Self-healing Carbon Fibre Reinforced Polymer for Aerospace Applications. *Composites Part A* **2007**, *38*, 1525-1532.
13. Chujo, Y.; Sada, K.; Saegusa, T., A Novel Nonionic Hydrogel from 2-Methyl-2-Oxazoline .4. Reversible Gelation of Polyoxazoline by Means of Diels-Alder Reaction. *Macromolecules* **1990**, *23*, 2636-2641.
14. Yoshie, N.; Saito, S.; Oya, N., A Thermally-stable Self-mending Polymer Networked by Diels–Alder Cycloaddition. *Polymer* **2011**, *52*, 6074-6079.
15. Chen, X.; Dam, M. A.; Ono, K.; Mal, A.; Shen, H.; Nutt, S. R.; Sheran, K.; Wudl, F., A Thermally Re-mendable Cross-Linked Polymeric Material. *Science* **2002**, *295*, 1698-1702.
16. Beijer, F. H.; Sijbesma, R. P.; Kooijman, H.; Spek, A. L.; Meijer, E. W., Strong Dimerization of Ureidopyrimidones via Quadruple Hydrogen Bonding. *J Amer Chem Soc* **1998**, *120*, 6761-6769.
17. Cordier, P.; Tournilhac, F.; Soulie-Ziakovic, C.; Leibler, L., Self-healing and Thermoreversible Rubber from Supramolecular Assembly. *Nature* **2008**, *451*, 977-980.
18. Cui, J.; Campo, A. d., Multivalent H-bonds for Self-healing Hydrogels. *Chem Commun* **2012**, *48*, 9302-9304.

19. Feldman, K. E.; Kade, M. J.; Meijer, E. W.; Hawker, C. J.; Kramer, E. J., Model Transient Networks from Strongly Hydrogen-Bonded Polymers. *Macromolecules* **2009**, *42*, 9072-9081.
20. Leibler, L.; Rubinstein, M.; Colby, R. H., Dynamics of Reversible Networks. *Macromolecules* **1991**, *24*, 4701-4707.
21. Kalista, S. J.; Ward, T. C., Thermal Characteristics of the Self-healing Response in Poly(ethylene-co-methacrylic acid) Copolymers. *J R Soc Interface* **2007**, *4*, 405-411.
22. Varley, R. J.; van der Zwaag, S., Towards An Understanding of Thermally Activated Self-healing of an Ionomer System During Ballistic Penetration. *Acta Mater* **2008**, *56*, 5737-5750.
23. Burattini, S.; Colquhoun, H. M.; Fox, J. D.; Friedmann, D.; Greenland, B. W.; Harris, P. J. F.; Hayes, W.; Mackay, M. E.; Rowan, S. J., A Self-repairing, Supramolecular Polymer System: Healability as A Consequence of Donor-acceptor π - π Stacking Interactions. *Chem Commun* **2009**, 6717-6719.
24. Hayes, S. A.; Jones, F. R.; Marshiya, K.; Zhang, W., A Self-healing Thermosetting Composite Material. *Composites Part A* **2007**, *38*, 1116-1120.
25. Hayes, S. A.; Zhang, W.; Branthwaite, M.; Jones, F. R., Self-healing of Damage in Fibre-reinforced Polymer-matrix Composites. *J R Soc Interface* **2007**, *4*, 381-387.
26. Luo, X. F.; Ou, R. Q.; Eberly, D. E.; Singhal, A.; Viratyaporn, W.; Mather, P. T., A Thermoplastic/Thermoset Blend Exhibiting Thermal Mending and Reversible Adhesion. *ACS Appl Mater Interfaces* **2009**, *1*, 612-620.

27. Wool, R. P., *Polymer Interfaces: Structure and Strength*. Hanser Publishers; Distributed in the USA and in Canada by Hanser/Gardner Publications: Munich; New York; Cincinnati, **1995**.
28. Yamaguchi, M.; Ono, S.; Terano, M., Self-repairing Property of Polymer Network with Dangling Chains. *Mater Lett* **2007**, *61*, 1396-1399.
29. Yamaguchi, M.; Ono, S.; Okamoto, K., Interdiffusion of Dangling Chains in Weak Gel and Its Application to Self-repairing Material. *Mater Sci Eng B* **2009**, *162*, 189-194.
30. Yamaguchi, M.; Maeda, R.; Kobayashi, R.; Wada, T.; Ono, S.; Nobukawa, S., Autonomic Healing and Welding by Interdiffusion of Dangling Chains in A Weak Gel. *Polym Int* **2012**, *61*, 9-16.
31. Doi, M.; Edwards, S. F., *The Theory of Polymer Dynamics*, Oxford; UK, **1986**.
32. Brown, H. R.; Yang, A. C. M.; Russell, T. P.; Volksen, W.; Kramer, E. J., Diffusion and Self-adhesion of the Polyimide PMDA-ODA. *Polymer* **1988**, *29*, 1807-1811.
33. Boiko, Y.; Prud'homme, R., Morphology of Fractured Polymer Surfaces Self-bonded Below the Glass Transition Temperature. *Mech Compos Mater* **1998**, *34*, 473-482.
34. Forrest, J. A.; Dalnoki-Veress, K.; Stevens, J. R.; Dutcher, J. R., Effect of Free Surfaces on the Glass Transition Temperature of Thin Polymer Films. *Phys Rev Lett* **1996**, *77*, 2002-2005.
35. Kajiyama, T.; Tanaka, K.; Takahara, A., Depth Dependence of the Surface Glass Transition Temperature of a Poly(styrene-block-methyl methacrylate) Diblock

- Copolymer Film on the Basis of Temperature-Dependent X-ray Photoelectron Spectroscopy. *Macromolecules* **1995**, *28*, 3482-3484.
36. Satomi, N.; Tanaka, K.; Takahara, A.; Kajiyama, T.; Ishizone, T.; Nakahama, S., Surface Molecular Motion of Monodisperse α,ω -Diamino-Terminated and α,ω -Dicarboxy-Terminated Polystyrenes. *Macromolecules* **2001**, *34*, 8761-8767.
37. Bitsanis, I. A.; Tenbrinke, G., A Lattice Monte-Carlo Study of Long-Chain Conformations at Solid Polymer Melt Interfaces. *J Chem Phys* **1993**, *99*, 3100-3111.
38. Brown, H. R.; Russell, T. P., Entanglements at Polymer Surfaces and Interfaces. *Macromolecules* **1996**, *29*, 798-800.
39. Blaiszik, B.; Kramer, S.; Olugebefola, S.; Moore, J. S.; Sottos, N. R.; White, S. R., Self-healing Polymers and Composites. *Annu Rev Mater Res* **2010**, *40*, 179-211.
40. Bielawski, C. W.; Grubbs, R. H., Living Ring-opening Metathesis Polymerization. *Prog Polym Sci* **2007**, *32*, 1-29.
41. Brown, E. N.; Sottos, N. R.; White, S. R., Fracture Testing of a Self-healing Polymer Composite. *Exp Mech* **2002**, *42*, 372-379.
42. Chipara, M. D.; Chipara, M.; Shansky, E.; Zaleski, J. M., Self-healing of High Elasticity Block Copolymers. *Polym Advan Technol* **2009**, *20*, 427-431.
43. Toohey, K. S.; Sottos, N. R.; Lewis, J. A.; Moore, J. S.; White, S. R., Self-healing Materials with Microvascular Networks. *Nature Materials* **2007**, *6*, 581-585.
44. Luo, X.; Ou, R.; Eberly, D. E.; Singhal, A.; Viratyaporn, W.; Mather, P. T., A Thermoplastic/Thermoset Blend Exhibiting Thermal Mending and Reversible Adhesion. *ACS Appl Mater Interfaces* **2009**, *1*, 612-620.

45. Park, J. S.; Takahashi, K.; Guo, Z.; Wang, Y.; Bolanos, E.; Hamann-Schaffner, C.; Murphy, E.; Wudl, F.; Hahn, H. T., Towards Development of a Self-healing Composite using a Mendable Polymer and Resistive Heating. *J Compos Mater* **2008**, *42*, 2869-2881.
46. Park, J. S.; Kim, H. S.; Thomas Hahn, H., Healing Behavior of a Matrix Crack on a Carbon Fiber/Mendomer Composite. *Compos Sci Tech* **2009**, *69*, 1082-1087.
47. Murphy, E. B.; Bolanos, E.; Schaffner-Hamann, C.; Wudl, F.; Nutt, S. R.; Auad, M. L., Synthesis and Characterization of a Single-component Thermally Remendable Polymer Network: Staudinger and Stille revisited. *Macromolecules* **2008**, *41*, 5203-5209.
48. Chen, Y.; Kushner, A. M.; Williams, G. A.; Guan, Z., Multiphase Design of Autonomic Self-healing Thermoplastic Elastomers. *Nature Chemistry* **2012**, *4*, 467-472.
49. Wool, R. P.; O'Connor, K. M., A Theory Crack Healing in Polymers. *J Appl Phys* **1981**, *52*, 5953-5963.
50. Mikos, A. G.; Peppas, N. A., Polymer Chain Entanglements and Brittle Fracture: 2. Autohesion of Linear Polymers. *Polymer* **1989**, *30*, 84-91.
51. Phadke, A.; Zhang, C.; Arman, B.; Hsu, C.-C.; Mashelkar, R. A.; Lele, A. K.; Tauber, M. J.; Arya, G.; Varghese, S., Rapid Self-healing Hydrogels. *Proc Natl Acad Sci* **2012**, *109*, 4383-4388.
52. Kim, Y. H.; Wool, R. P., A Theory of Healing at a Polymer-polymer Interface. *Macromolecules* **1983**, *16*, 1115-1120.

53. Jud, K.; Kausch, H. H., Load Transfer Through Chain Molecules after Interpenetration at Interfaces. *Polym Bull* **1979**, *1*, 697-707.
54. Kausch, H.; Jud, K., Molecular Aspects of Crack Formation and Healing in Glassy Polymers. *Plast Rubber Process Appl* **1982**, *2*, 265-268.
55. http://shop.perkinelmer.com/content/technicalinfo/tch_ftiratr.pdf.
56. Stefan, I. C.; Mandler, D.; Scherson, D. A., In Situ FTIR-ATR Studies of Functionalized Self-assembled Bilayer Interactions with Metal Ions in Aqueous Solutions. *Langmuir* **2002**, *18*, 6976-6980.
57. Freger, V.; Ben-David, A., Use of Attenuated Total Reflection Infrared Spectroscopy for Analysis of Partitioning of Solutes Between Thin Films and Solution. *Anal Chem* **2005**, *77*, 6019-6025.
58. Boiko, Y. M.; Bach, A.; Lyngaae-Jorgensen, J., Self-bonding in an Amorphous Polymer Below the Glass Transition: A T-peel Test Investigation. *J Polym Sci Pol Phys* **2004**, *42*, 1861-1867.
59. Tanaka, K.; Kajiyama, T.; Takahara, A.; Tasaki, S., A Novel Method To Examine Surface Composition in Mixtures of Chemically Identical Two Polymers with Different Molecular Weights. *Macromolecules* **2002**, *35*, 4702-4706.
60. Tanaka, K.; Ariura, F.; Nagamura, T.; Kajiyama, T., Further Study of Chain End Effect on Surface Mobility in Monodisperse Polystyrene Films. *Polym J* **2004**, *36*, 498-501.
61. Pippig, F.; Sarghini, S.; Holländer, A.; Paulussen, S.; Terryn, H., TFAA Chemical Derivatization and XPS. Analysis of OH and NH_x Polymers. *Surf Interface Anal* **2009**, *41*, 421-429.

62. Ma, X.; Sun, Q.; Su, Y.; Wang, Y.; Jiang, Z., Antifouling Property Improvement of Poly(vinyl butyral) Ultrafiltration Membranes Through Acid Treatment. *Sep Purif Technol* **2007**, *54*, 220-226.

Chapter 4

General Conclusions

Rheology is one of the physical sciences, which deals with deformation and flow of a material under stress. The information obtained from rheological measurements is important for many applications to control the mechanical responses. In general, amorphous polymers show rheological four regions, including glassy, transition, rubbery, and terminal zones, from low temperature or short time region. In rubbery and terminal regions, the material shows self-healing property owing to the intermolecular diffusion at least to some degree. Of course, the degree of healing is determined by the time scale. Furthermore, marked molecular motion at the surface contributes to the healing ability. The most serious problem for self-healing materials using molecular interdiffusion is macroscopic deformation, i.e., flow. Since the time/temperature range of the rubbery region is determined by the number of entanglement couplings per a molecule, a high molecular-weight polymer with low entanglement molecular weight would show a broad rubbery region. This is exceptional for a self-healing polymer using molecular interdiffusion, because it hardly shows macroscopic flow.

In this thesis, poly(vinyl butyral), a terpolymer composed of vinyl butyral, vinyl

alcohol and vinyl acetate, which is called “PVB”, is employed. Although the physical properties were barely understood for this polymer because of the restricted applications such as structural adhesive and coating, it is found in this study that PVB shows good self-healing behavior even at room temperature. In order to understand the mechanism, the rheological properties have to be clarified in detail at first.

In the second chapter, therefore, the rheological four regions of PVB are studied. The master curves of frequency dependence of oscillatory shear moduli covering the terminal and rubbery zones in the frequency range are evaluated. From the curves, the rubbery plateau modulus, G_N^0 , is calculated by the integration of G'' from $\ln \omega = -\infty$ to the maximum of G'' in the rubbery to terminal regions, and found to be 1.3 MPa. The average molecular weight between entanglement couplings (M_e), inversely proportional to G_N^0 , is thus calculated to be 2,670. Because of the low value of M_e , PVB shows wide ranges of the rubbery region, i.e.; it hardly shows macroscopic flow. Moreover, the low M_e is responsible for the high level of the onset shear stress of the shark-skin failure, leading to high out-put rate at extrusion processing even using the sample with narrow molecular weight distribution. It will be a advantage for extrusion, because it can be processed at a high out-put rate condition.

In the third chapter, the self-healing ability of PVB is demonstrated. It is found that the self-healing behavior occurs even below T_g of the bulk by reptation motion without macroscopic flow. This is attributed to the low T_g at the surface as compared with the bulk, which enhances molecular motion. Moreover, the water molecules adsorbed on the surface which is attributed to the surface localization of vinyl alcohol in PVB also affects the

molecular motion, because it acts as a plasticizer. Therefore, the healing efficiency is enhanced at high humidity condition.

In the near future, PVB will be seriously considered to be employed in industry for various products. The good processability also supports the availability in industry. Because the self-healing is pronounced by the moisture, it is applicable for outdoor materials. After raining, the scratch will be repaired automatically. The healing function will be enhanced more by the consideration of primary molecular structure; i.e., the increase in hydroxyl group can improve the absorption of water molecules at surface, leading to reduction of T_g at the surface, while T_g at bulk is still high. In case of processability, the broadening of molecular weight distribution will increase the out-put rate because it can reduce the shear stress and increase in the onset shear stress.

Additionally, from the viewpoint of the polymer design on the self-healing property, the appropriate hydroxyl group in a material will be an important technique to enhance the healing ability by the moisture in atmosphere, because T_g at the surface will decrease while T_g at bulk is still high.

Finally, the result in this thesis provides the new concept of self-healing polymers. Introduction of hydroxyl group only on surface will provide the healing ability by the aid of water as a plasticizer. In particular, polyester and polyamide will be appropriate polymers for this technique. Through this technological progress, I wish various polymers have self-healing property in near future.

Achievements

Publications

1. **Sunatda Arayachukiat**, Monchai Siriprumpoonthum, Shogo Nobukawa, Masayuki Yamaguchi, Viscoelastic Properties and Extrusion Processability of Poly(Vinyl Butyral). *Journal of Applied Polymer Science* 2014, 131 (11), 40337 (7 pages).
2. **Sunatda Arayachukiat**, Vu Anh Doan, Tatsuya Murakami, Shogo Nobukawa, Masayuki Yamaguchi, Autonomic Self-Healing of Poly(Vinyl Butyral). *Journal of Applied Polymer Science* 2015, 132, 42008 (6 pages).
3. Ryuya Osato, **Sunatda Arayachukiat**, Shogo Nobukawa, Masayuki Yamaguchi, Self-Healing Properties of Poly(Ethylene-*co*-Vinyl Acetate), to be submitted.

Presentations

International Conferences

Reviewed

1. **Sunatda Arayachukiat**, Shogo Nobukawa and Masayuki Yamaguchi, “Rheological properties and self-healing behavior of poly(vinyl butyral)”. SPE ANTEC 2014 Conference & Exhibition, 28-30 April 2014, Rio All Suites Hotel, Las Vegas, Nevada, USA.

2. **Sunatda Arayachukiat**, Shogo Nobukawa and Masayuki Yamaguchi. “Repairing behavior of weak gels having dangling chains”. ECCM16 – 16th European conference on composite materials, 22-26 June 2014, Venue barcelo renacimiento, Seville, Spain.

Domestic Conferences

Non-reviewed

1. **Sunatda Arayachukiat**, Shogo Nobukawa and Masayuki Yamaguchi. “Self-repairing ability of plasticized poly(vinyl butyral)”. 63rd Symposium on Macromolecules, 24-26 September 2014, Nagasaki University, Nagasaki, Japan.
2. **Sunatda Arayachukiat**, Shogo Nobukawa and Masayuki Yamaguchi. “Self-healing behavior of plasticized poly(vinyl butyrate)”. 62nd SPSJ Annual meeting, 29-31 May 2012, Kyoto International conference center, Kyoto, Japan.

Other Publications

1. **Sunatda Arayachukeat**, Tanapat Palaga, Supason Wanichwecharungruang, Clusters of Carbon Nanospheres Derived from Graphene Oxide. ACS Applied Materials & Interfaces 2012, 4, 6808-6815.
2. Panitha Phulkerd, **Sunatda Arayachukiat**, Tong Huang, Inoue, T., Shogo Nobukawa, Masayuki Yamaguchi, Melting Point Elevation of Isotactic Polypropylene. Journal of Macromolecular Science, Part B 2014, 1222-1230.

Awards

1. Grant for Researchers Attending International Conference, Marubun foundation to present at SPE ANTEC 2014, Las Vegas, USA, April 2014.
2. Grant for Researchers Attending International Conference, TEPCO foundation to present at ECCM16 – 16th, Seville, Spain, June 2014.
3. Awarded in Ph D. dual degree program (CU-JAIST), Japan Advanced Institute of Science and Technology (JAIST), Japan
4. Awarded in The Special Task force for Activating Research (STAR) from the Centenary Academic Development Project, Thailand
5. Awarded in The 90th anniversary of Chulalongkorn University, Thailand (Ratchadaphiseksomphot Endowment Fund)

Clusters of Carbon Nanospheres Derived from Graphene Oxide

1. Introduction

In the past 50 years, various carbon nanostructures, including spherical buckyballs or fullerenes [1], giant fullerenes [2,3] single-walled and multiwalled carbon nanotubes (SWCNTs and MWCNTs, respectively) [4], graphene sheets, graphene nanoribbons, carbon onions and cones [5], and dahlialike and budlike aggregates [6], have drawn considerable research interest. Their prospective applications as materials for various industries, such as multifunctional nanometer scaled catalytic, magnetic, and optoelectronic materials [7–9], nanoelectronics [10], polymer composites [11], biosensors [12], solar cells [13], surfactants [14] and gas absorption/storage [15], have been pursued. Recently, many biomedical aspects of these various carbon nanostructures have been reported, including their cytotoxicity and bio-compatibility [16–18], and surface modifications for medical applications [19,20]. Their applications as biomaterials have been demonstrated in the areas of drug/gene delivery [21–24], bone tissue engineering [25,26], and cellular imaging [27]. In 2009, Wang et al. demonstrated that sonicating GOSh in concentrated acids could cut them into nanofragments and soluble polyaromatics, which subsequently underwent cavitation-induced condensation to form various carbon nanostructures, including CNTs, fullerene-like carbon nanoparticles, and nanoribbons [28].

Transformation of one carbon nanostructure into other by both gas and solution phase processes have also been reported, including, for example, the transformation of graphene sheets into fullerenes [29], GOSh into CNTs, and MWCNTs into nanoribbons [30]. Aggregation of small carbon nanostructures into larger morphologies, such as the aggregation of carbon nanohorns (20–50 nm in tubule length and 1–3 nm in diameter) into spherical particles of around 100 nm in diameter, and aggregation of C60 fullerenes into spherical particles of around 5–500 nm, has also been demonstrated in the gas phase [31–33]. Indeed, noncovalent interactions can lead to the formation of graphitic carbon in various forms. Here, the in solution transformation of graphite and graphene nanoplatelets (GNPs) into a cluster of carbon nanospheres (CCNs) is reported. Structural characterization of the CCNs using various analytical techniques is reported, and the mechanism of formation of CCNs is proposed. Finally, the application of the CCNs as an efficient curcumin carrier is demonstrated in vitro.

2. Materials and methods

2.1. Materials

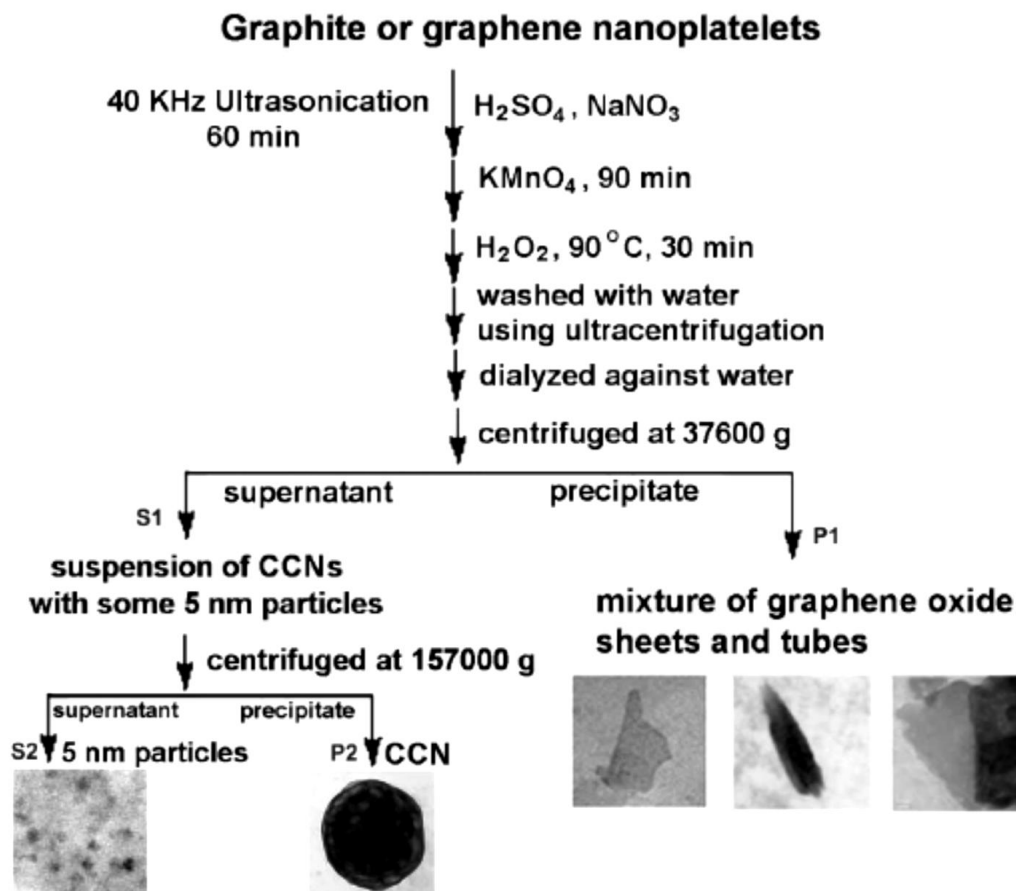
Natural flake graphite (graphite) of 200-300 μm in size was obtained from the Thai Carbon and Graphite Co., Ltd. (Bangkok, Thailand). GNPs of 6-8 nm thick x 5 microns wide were purchased from Strem Chemicals, Inc. (Newburyport, MA, USA). Fuming nitric acid (>90%) and sulfuric acid (95-98%) were obtained from Sigma-Aldrich (USA). Potassium permanganate and hydrogen peroxide (H_2O_2 ; 18% (w/v)) were obtained from Suksapan (Bangkok, Thailand). Dialysis tubing, made from a regenerated cellulose tubular membrane (CelluSep T4) with a MWCO of 12000-14000 Da, 75 mm flat-width size and a

17.9 ml cm⁻¹ volume capacity, was obtained from Membrane Filtration Products (Seguin, TX, USA). All other chemicals were analytical grade reagents.

2.2 Synthesis of Cluster of Carbon Nanospheres (CCNs)

Cluster of Carbon Nanospheres (CCNs) was synthesized from the graphite or GNP using a modification to the method of Hummers and Offeman [34] as follows. One gram of graphite or GNP was exfoliated by mixing with 1.0 g of sodium nitrate and 50 mL of 18 M sulfuric acid and then sonicating the mixture at 40 KHz at room temperature for 1 h. Then, 6.0 g of potassium permanganate was added and the mixture was stirred for 90 min, followed by 100 mL of deionized (DI) water and increasing the temperature to 90 °C for 30 min. After that, 300 mL of DI water was added, the mixture stirred for another 10 min and then the excess potassium permanganate was removed by adding 50 mL of 5% (w/v) H₂O₂ and stirring at room temperature for 30 min. Finally, the obtained mixture was washed with water using centrifugation (6,000 g; 10 min) and dialysis against 5 L water, changed every 24 h until pH 6 was reached. The graphite oxide, of various morphologies, that was obtained at this stage was then centrifuged at 9,400 g for 10 min to remove (precipitate) various artifacts, followed by centrifugation of the supernatant at 11,300 g for 15 min (to pellet the CNTs) and then at 21,100 g for 15 min (to pellet the GOSh). Finally, the supernatant was centrifuged at 37,000 g for 30 min to remove the residual smaller GOSh, leaving the supernatant containing the spheres. The supernatant containing the spheres was then ultracentrifuged at 157,000 g for 30 min to partially separate the CCNs from smaller particles (5 nm particles). The pelleted CCNs were then freeze-dried for storage and later re-suspended in DI water by ultrasonication (40 KHz, 25 °C, 5 min) when

required.



Scheme 1 Synthesis of CCNSs from graphite or graphene nanoplatelets
(GNPs)

2.3. Characterization of the CCNs

2.3.1. Morphology and size of the CCN

The dry particle morphology was evaluated by scanning electron microscopy (SEM) using a JSM-6400 (JEOL) scanning electron microscope and transmission electron microscopy (TEM) using a JEM-2100 (JEOL) transmission electron microscope. The hydrated particle morphology was evaluated, in terms of the hydrated particle size, polydispersity index (PDI) and zeta potential, by dynamic light scattering (DLS) on a freshly prepared aqueous suspension of CCNs using a Zetasizer nanoseries model S4700 (Malvern Instruments).

2.3.2. Chemical structure and composition of CCNs

The freeze-dried CCNs were then characterized as follows. The dry particle morphology was evaluated by scanning electron microscopy (SEM, JSM-6400, JEOL) and transmission electron microscopy (TEM, JEM-2100, JEOL). The chemical structure of the CCNs was evaluated by (i) UV-visible absorption spectroscopy (UV-Vis, UV2500, Shimadzu), (ii) attenuated total reflectance-Fourier transform infrared spectroscopy (ATR-FTIR, Nicolet 6700), (iii) Raman spectroscopy (Thermo Electron Raman microscope, equipped with a triple monochromator, a 5 mW Ar⁺ laser ($\lambda = 780$ nm) excitation source), (iv) X-ray photoelectron spectroscopy (XPS, a Kratos AXIS Ultra DLD instrument using a monochromatic Al K α X-ray source at 1486.6 eV and operated at 150 W, 15 kV and 10 mA with a base pressure in the XPS analysis chamber of 5×10^{-8} Torr, of which high-resolution spectra (C1s and O1s) were acquired using a pass energy of 20 eV and 0.1 eV energy steps and all binding energies were referenced to the hydrocarbon C1s

peak at 285 eV), (v) elemental analysis (EA, combustion through the PE2400 Series II, Perkin Elmer), and (vi) X-ray diffraction analysis (XRD, a Rigaku DMAX 2200/Ultima+ diffractometer using Cu K α radiation source and operating at 40 kV and 30 mA). The hydrodynamic diameter and zeta potential value of the CCNs were evaluated by dynamic light scattering (DLS) on a freshly prepared aqueous suspension of CCNs using a Zetasizer nanoseries model S4700 (Malvern Instruments).

2.3. Synthesis of TAMRA-CCNs

Five mg of tetramethylrhodamine-5-carbonyl azide (TAMRA) was dissolved in 1.0 mL of dimethylformamide (DMF) at 0° C. Then 6.0 mg of 1-ethyl-3-(3-dimethylaminopropyl)-carbodiimide (EDCI) was added and the mixture was incubated for 30 min before 4.0 mg of N-hydroxysuccinamide (NHS) in 0.1 mL DI water was added followed by the addition of 100 mL of the CCNs suspension (0.5 mg/mL), and the mixture was stirred in an ice bath overnight. Finally, the TAMRA-CCNs suspension was dialyzed against DI water until no TAMRA could be detected in the dialysate. The TAMRA-labeled CCNs were further purified by soaking in methanol and then filtering through a centrifugation based filtration tube (Millipore, MWCO 100,000) to remove all of the non-covalently bound TAMRA.

2.4. Curcumin-loaded TAMRA-CCNs

Curcumin solution (4.0 mg curcumin in 0.5 mL ethanol) was added to an aqueous suspension of TAMRA-CCNs (10.0 mL containing 8.0 mg TAMRA-CCNs) and the mixture was incubated at room temperature for 3 h. The suspension was dialyzed against

DI water (3×1 L) under light-proof conditions, and the suspension in the dialysis bag was then collected.

2.5. Encapsulation efficiency (EE) and drug loading

To determine the curcumin encapsulation efficiency (EE) in the TAMRA-CCNs, the freeze-dried curcumin-loaded TAMRA-CCNs were suspended in 5.0 mL of ethanol and incubated under light-proof conditions at room temperature for 1 h. Then, the suspension was centrifugally filtered through a MWCO 100,000 membrane (Amicon Ultra-15, Millipore, MA, USA) and the ethanol extract (elutant) was collected. The concentration of curcumin in the extract was determined by measuring the absorbance at 425 nm by UV/Vis spectroscopy with reference to a standard curve derived from curcumin concentrations in the range of 0.5 – 10 $\mu\text{g/mL}$. The EE and curcumin loading level were calculated using Eqs. (1) and (2), respectively, as follows:

$$\% \text{ EE} = 100(C_e/C_i) \quad (1)$$

$$\% \text{ curcumin loading} = 100(C_e/C_s) \quad (2)$$

Where C_e , C_i and C_s are the weights of the extracted curcumin, the curcumin initially added and curcumin-loaded TAMRA-CCNs, respectively.

2.6. Cell culture

The human embryonic kidney (HEK293T) and human epidermoid cervical carcinoma (CaSki) cell lines (purchased from ATCC) were seeded in 25 cm^2 vented culture flasks and incubated at 37° C in a humidified atmosphere of 95:5 % (v/v) air: CO_2 , in 7 mL of complete medium (CM). CM was comprised of either Dulbecco's Modified Eagle

medium (HyClone, Logan, UT, USA) (for HEK293T cells) or Roswell park memorial institute medium 1640 (for CaSki cells) as the base and then supplemented with 10% (v/v) fetal bovine serum (FBS) (HyClone), 1% (w/v) 100 mM Sodium pyruvate (HyClone), 1% (w/v) 1 M N-2-hydroxyethylpiperazine-N'-2- ethanesulfonic acid (HyClone) (HEPES), 100 U/mL penicillin (General Drugs House Co. Ltd, Bangkok, Thailand) and 0.4 mg/mL streptomycin sulphate (M&H Manufacturing Co. Ltd, Samut Prakan, Thailand). The CM was changed every 2-3 days and cells were repassaged when they reached 80-85% confluency.

2.7. Cellular uptake of CCNs

HEK293T cells, at a density of 3×10^5 cells per well, were seeded in six-well plates on cover slips and incubated overnight. The curcumin, as either 8 ppm free curcumin or as curcumin-loaded TAMRA-CCNs at a curcumin concentration of 8 ppm, as well as the phosphate buffered saline (PBS; 137 mM NaCl, 2.7 mM KCl, 10 mM NaHPO₄/NaH₂PO₄, pH 7.2) negative control, were added directly to the adhered cells in each well and incubated as above for 2 h. The cells were then washed and replaced with fresh complete medium (CM) three times, fixed in 1.0 mL of 4.0% (w/v) paraformaldehyde for 15 min and then washed with CM. Cells were then incubated with 50 µL of 0.1 mg/mL acridine orange solution for 10 min, washed with CM and then analyzed by confocal laser scanning microscopy (CLSM), using a Nikon Digital Eclipse C1-Si equipped with Plan Apochromat VC 100×, Diode Laser and 85 YCA-series Laser (405 nm and 561 nm, respectively, Melles Griot, USA), a Nikon TE2000-U microscope, a 32-channel-PMT-spectral-detector and Nikon-EZ-C1 Gold Version 3.80 software).

2.8. Assessment of cell viability

The assessment of cell viability was performed using the 3-(4,5-dimethylthiazol-2-yl)-2,5-diphenyltetrazolium bromide (MTT) mitochondrial activity assay as a surrogate measure of cell viability. HEK293T and CaSki cells were seeded into 96-well plates at a density of 1×10^4 cells/well in CM and allowed to adhere. After removal of the CM, cells were exposed to 100 μ L of CCNs at various concentrations (range of 0.01-10 μ g/mL) in CM for 48 h under standard culture conditions (section S1 of SI). Then, 10 μ L of PBS containing 1 mg/ml MTT was added to each well and incubated as above for 4 h before removing the media. The cell membranes were permeabilized and the formazan crystals dissolved by aspirating in 200 μ L/well of isopropanol. The plates were then centrifuged at 4840 g for 10 min, and 50 μ L of the supernatant was harvested for measurement of the absorbance at 540 nm using a microplate reader (Anthos 2010, Becthai Bangkok Equipment and Chemical Co., Ltd., Thailand). All conditions were tested in triplicate.

3. Results and discussion

3.1. CCNs Synthesis

By oxidizing graphite (200-300 μ m) or GNP (6-8 nm thick \times 5 microns wide), using a modified process from that of Hummer and Offeman, various shapes of carbon-based materials could be obtained and they could be partially separated from one another by centrifugation (Scheme 1). Centrifugation at 37100 g resulted in suspension of spherical nanoparticles with an average diameter of 130 nm mixed with spherical

nanoparticles with an average diameter of 5 nm. The 130 nm particles (carbon oxide nanospheres or CCNs) could be harvested (with still some contamination from the 5 nm particles) by centrifugation at 157000 g. The freeze-dried CCNs could be re-suspended in water with the aid of ultrasonication to obtain a well dispersed suspension. At the same concentration, the water suspension of the CCNs was transparent yellow-brownish whilst that of the GOSh (precipitate from the centrifugation at 37100 g, see Scheme 1) was a deeper color (Figure 1).



Figure 1 Images of (left) GOSh and (right) CCNs, both at 100 ppm in water.

3.2. CCNs Characterization

3.2.1. Morphology and size of the CCN

SEM photographs of GOSh and CCNs are shown in Table 1. The SEM photograph showed sheet like materials for GOSh and spherical architecture for CCNs. The average diameter of CCNs calculated from SEM image (30,000x) was 129.6 ± 0.1 nm. TEM photographs of GOSh and CCNs are shown in Table 2. The TEM images of GOSh showed sheets like material with size range of 100-300 nm. The TEM images of CCNs showed spherical shape with size range of 100-200 nm. To analyze hydrated particle size, dynamic light scattering (DLS) was used. The average hydrated diameter and surface charge of

GOSh were 271.1 ± 7.22 nm and -50.21 ± 0.73 mV, respectively. The average hydrated diameter and surface charge of CCNs were 132.1 ± 4.74 nm and -47.56 ± 1.18 mV, respectively. The average diameter of CCNs obtained from DLS is quite similar to that of 110.8 ± 0.09 nm obtained from SEM. The highly negatively charged surface (more than -30 mV) of both particles indicated good stability in water.

Table 1 SEM photographs of GOSh and CCNs

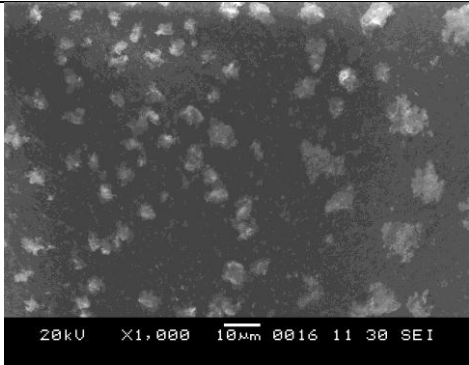
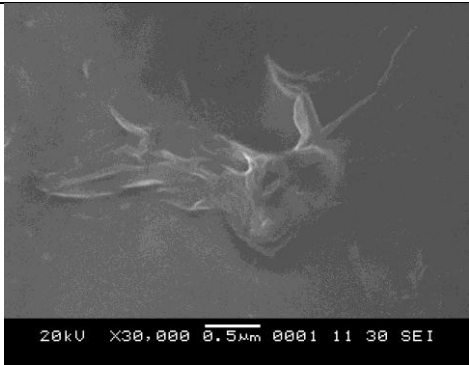
Samples	Magnification	Scale bar (μ m)	SEM photograph
GOSh	1000x	10	
	30,000x	0.5	

Table 1 SEM photographs of GOSh and CCNs (continue)

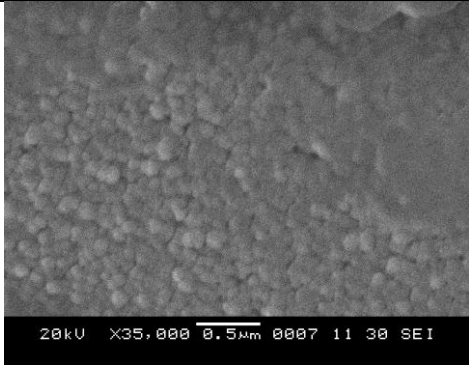
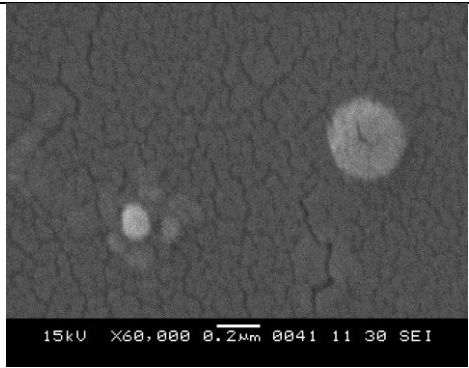
Samples	Magnification	Scale bar (μm)	SEM photograph
CCNs	35,000x	0.5	
	60,000	0.2	

Table 2 TEM photographs of GOSh and CCNs

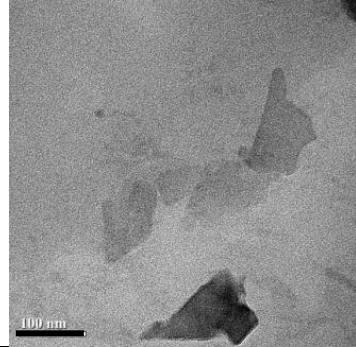
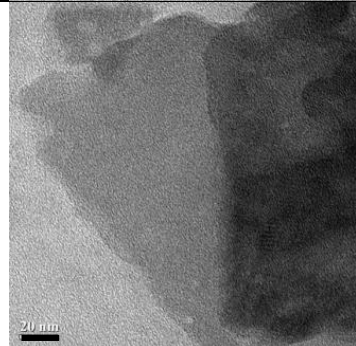
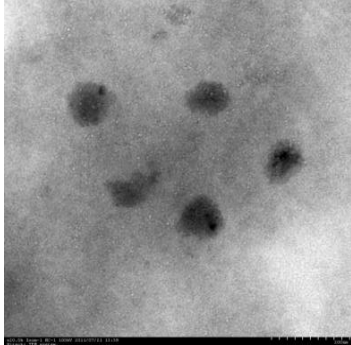
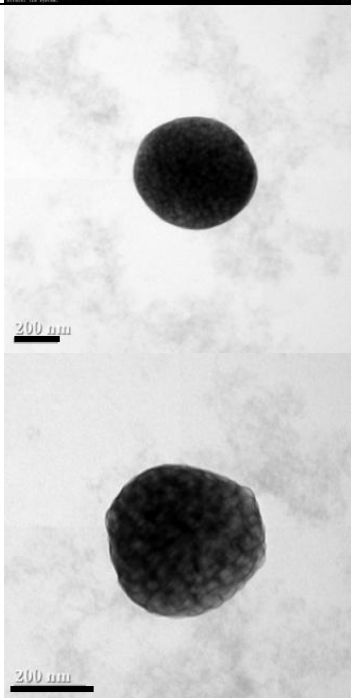
Samples	Magnification	Scale bar (μm)	TEM images
GOSh	20,000x	0.1	
	40,000x	0.02	

Table 2 TEM photographs of GOSh and CCNs (continue)

Samples	Magnification	Scale bar (μm)	TEM images
CCNs	20,000x	0.2	
	60,000x	0.2	

3.2.2. Chemical structure and composition of CCNs

3.2.2.1 UV-spectroscopy

The UV-Vis absorption spectra of GOSh and CCNs were similar with a maximum absorption at 227 nm and an extended absorption up to 600 nm (Figure 2), which corresponded well with the presence of an extended π - π conjugation network.

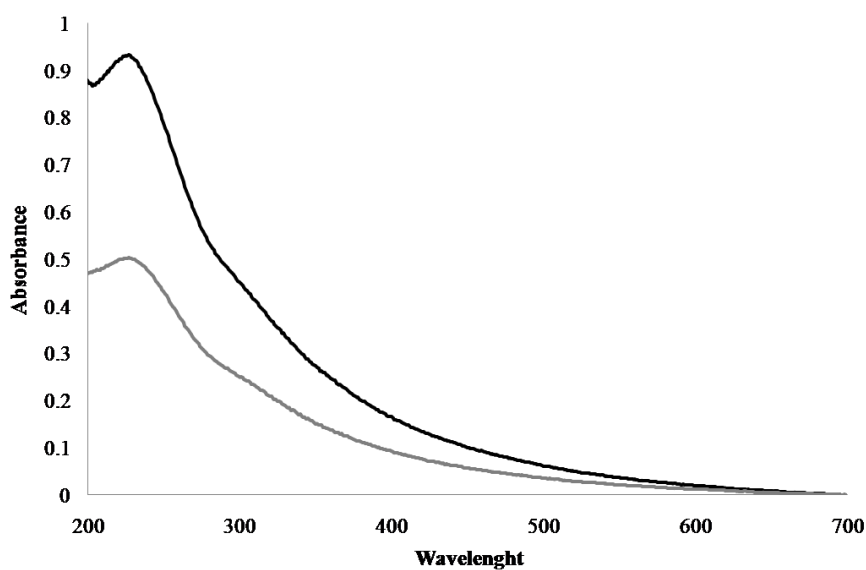


Figure 2 UV absorption spectra of GOSh (gray line) and CCNs (black line) at final concentration of 8 ppm

3.2.2.2 Attenuated total reflectance-fourier transform infrared spectroscopy (ATR-FTIR)

The functional group characterization of CCNs was carried out by ATR-FTIR analysis. CCNs suspension was freeze dried and then subjected to ATR-FTIR analysis. The ATR-FTIR spectrum of CCNs showed a broad OH stretching at $3,344\text{ cm}^{-1}$, obvious C=C stretching at $1,600\text{-}1,800\text{ cm}^{-1}$, O-H bending at $1,362\text{ cm}^{-1}$ and C-O stretching at $1,205\text{ cm}^{-1}$ (Figure 3). The result indicates that CCNs is an oxidized product from the chemical exfoliation/oxidation of graphite.

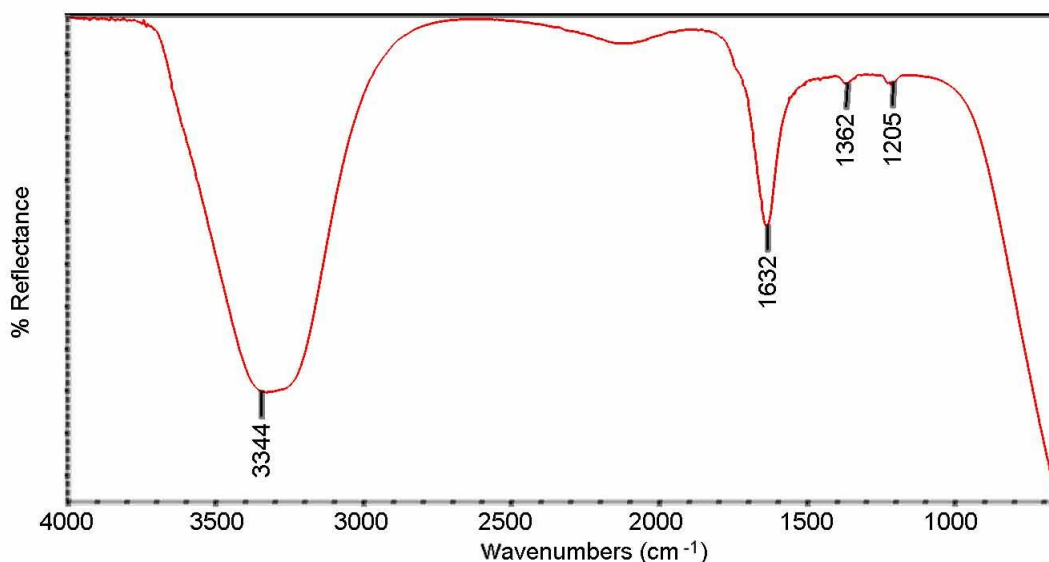


Figure 3 FTIR spectrum of CCNs

3.2.2.3 Raman spectroscopy

The structural characterization of graphite and CCNs was also carried out by Raman spectroscopy. The vibration spectra of graphite and CCNs are shown in Figure 4. The Raman spectrum of graphite showed peak at 1312 cm^{-1} and 1578 cm^{-1} referring to G band and D band, respectively. G band implies the disorder-induced vibrational peak of the sp^2 carbon lattice. D band implies the stretching vibrations peak from the sp^2 -hybridized carbon atoms. The Raman spectrum of CCNs showed broader G and D bands with their slight blue shift at 1329 cm^{-1} and 1594 cm^{-1} , respectively. The Raman spectrum of CCNs also showed an obvious shoulder at $1750\text{--}1800\text{ cm}^{-1}$, implying the structural deformation of the sp^2 -hybrid carbon plane due to graphite amorphization. The shoulder at $1750\text{--}1800\text{ cm}^{-1}$ which correspond to the C=O functionality contains was absent from the Raman spectrum of graphite. This confirms that CCNs contains carbonyl and hydroxyl groups in their carbon network structure.

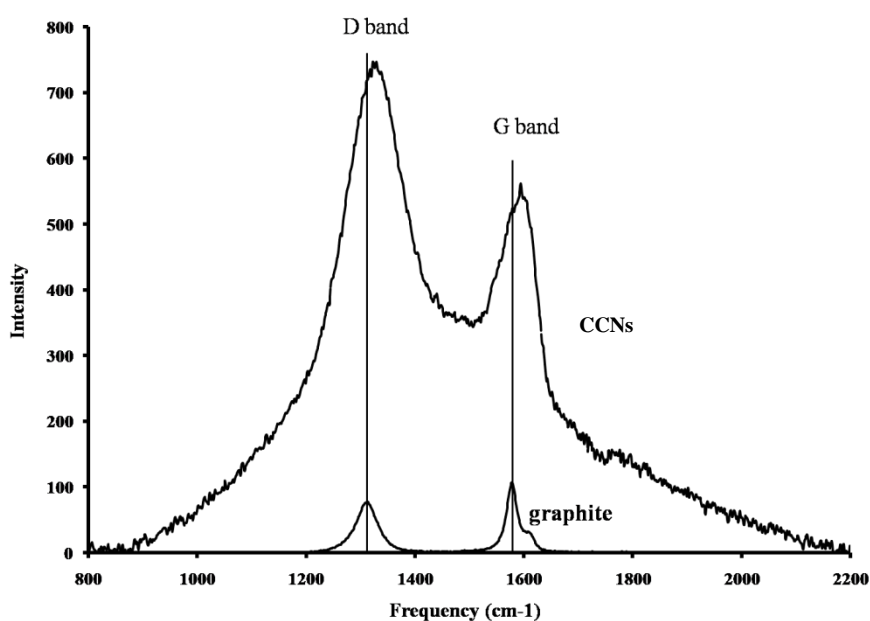


Figure 4 Raman spectra of graphite and CCNs

3.2.2.4 X-ray photoelectron spectroscopy (XPS)

To investigate functional group at surface of carbon-based nanomaterials, XPS analysis was used. All samples, graphite, GOSh and CCNs, were freeze dried and then subjected to XPS. XPS analysis of graphene oxide revealed the C-C, C=C, C-O (from C-O-C and C-OH), C=O and COOH functional groups which are C1s and O1s spectrums. The BE of the C-C, C=C, C-O (from C-O-C and C-OH), C=O, and COOH functional groups from C1s spectrum are 283.6, 284.3, 286.3, 288.1 and 289.4 eV, respectively. The BE of the C-O (from C-O-C and C-OH), C=O, and COOH functional groups from O1s spectrum are 533.0, 531.7 and 530.5 eV, respectively. The C1s spectrum of graphite showed C-C, C=C, C=O and COOH functional groups. The O1s spectrum of graphite showed C=O and COOH functional group. The C1s spectrum of GOSh and CCNs showed C-C, C=C, C-O, C=O and COOH functional groups. The O1s spectrum of GOSh and CCNs showed C-O, C=O and COOH functional groups. The XPS results indicated that GOSh and CCNs have carbonyl and hydroxyl functional groups at surface.

3.2.2.5 Elemental analysis (EA)

Quantitative analysis of the elemental composition of the carbon-based nanomaterials was identified by combustion elemental analysis. The C/O molar ratios of all samples are shown in Table 1. The C/O molar ratio of graphite, GNPs, GOSh and CCNs were 7.4, 12.7, 1.29 and 1.55, respectively. The two starting materials, graphite and GNPs, possess higher C/O than GOSh and CCNs. These indicated that GOSh and CCNs were heavily oxidized of the whole structure. Moreover, the C/O molar ratios of graphite, GOSh and CCNs calculated from XPS were 0.800, 0.428 and 0.295, respectively. XPS results corresponded to surface C/O composition of the material. The comparison between the C/O molar ratio of XPS and EA, indicated that the particles were more oxidized and/or hydrated at the surface. Furthermore, GOSh and CCNs were more oxidized than starting material, graphite. However, it should be noted that both the GOSh and CCNs were prepared in an aqueous environment and dried under vacuum, so it is very likely that some water molecules would be trapped in the materials, giving the low C/O ratios.

3.2.2.6 X-ray diffraction analysis (XRD)

The crystallinity of graphite and CCNs, was determined by X-ray diffraction analysis. The XRD pattern of graphite showed sharp peak around 26 degree (Figure 5). The XRD pattern of the CCNs showed a broad peak around 10 degree. XRD results indicated that graphite possess high crystalline structure which CCNs was less crystallinity. This indicated that the oxidation of graphite and GNPs reduced crystallinity.

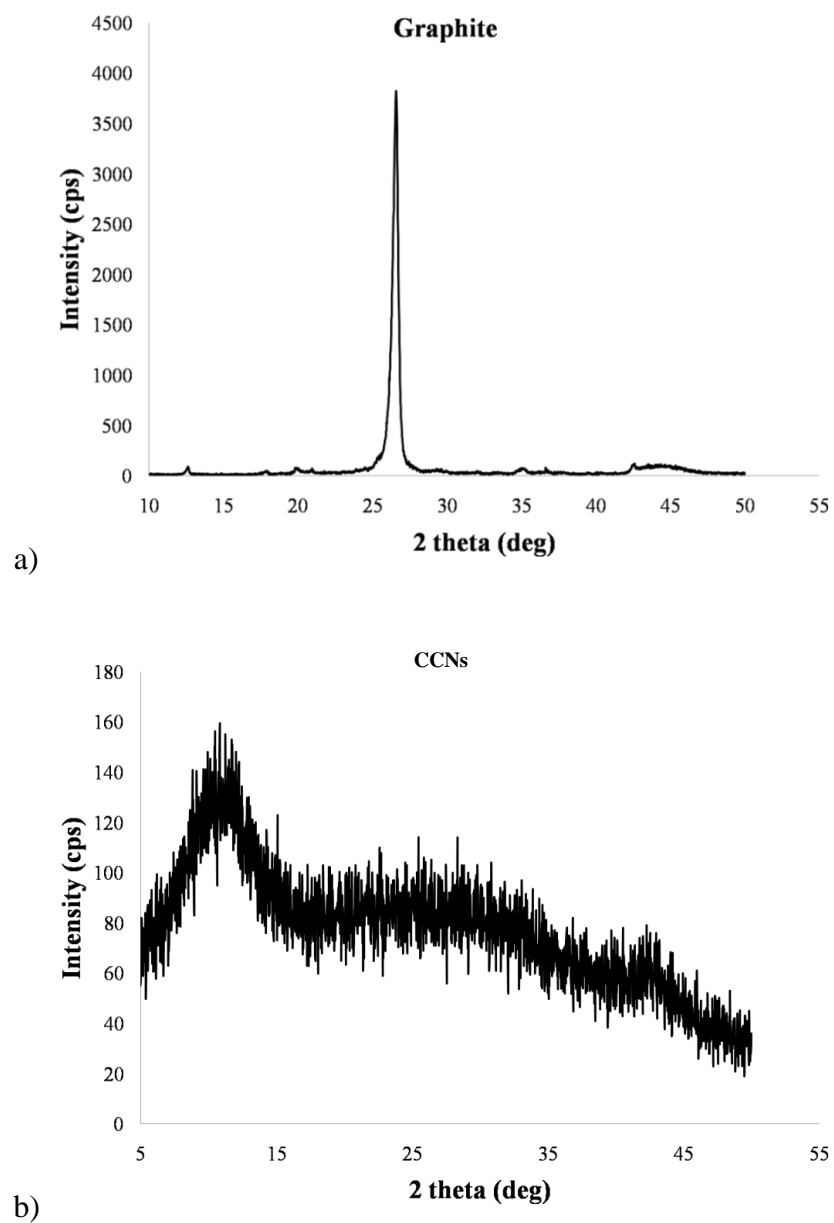


Figure 5 The XRD pattern of (a) graphite and (b) CCNs

3.4. TAMRA labeling

In order to follow CCNs within cells, we covalently linked the fluorophore 5,6-carboxytetramethylrhodamine (TAMRA) to the CCNs to obtain TAMRA-CCNs (CCNsT). Successful grafting was confirmed by the appearance of a new small absorption band at 565 nm in the UV-Vis absorption spectrum of CCNsT (Figure 6) and also the obvious fluorescent nature of the CCNsT particles under the fluorescent microscope.

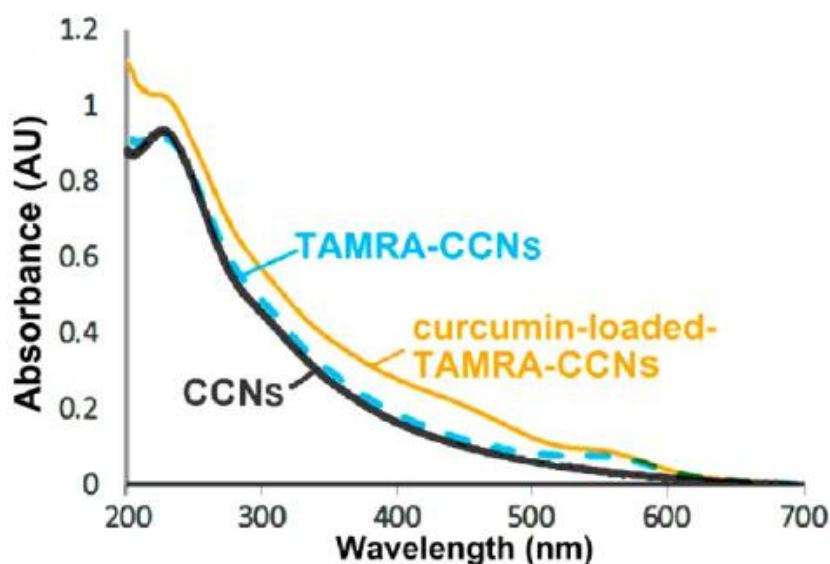


Figure 6 UV absorption spectra of CCNs and CCNsT and the curcumin-loaded CCNsT

3.5. Curcumin loading

The UV-Vis absorption spectrum of the water suspension of the curcumin-loaded CCNsT is shown in Figure 6. Inspection of the suspension under optical microscopy showed no curcumin precipitate. The amount of bound curcumin (extracted from CCNs) was 18.5 ± 1.4 % (w/w of curcumin to curcumin-loaded CCNsT), the number agrees with the value obtained through the quantitative analysis of the dialysate water.

3.6. Cellular uptake of CCNs

To track the cellular uptake and localization of CCNsT and curcumin *in vitro*, CLSM was used. The HEK293T cells were placed on cover slip for 24 h and then were exposed to either free curcumin or CCNsT-C. After incubation with samples for 2 h, the cells were then thoroughly washed and stained with acridine orange (green). After that the sample was subjected to CLSM analysis. The obtained fluorescent images from various areas were deconvoluted to obtain single fluorescent signal of curcumin, CCNsT and acridine orange. All the unmixing was carried out using Nikon-EZ-C1 gold v3.80 software. It was possible because the three emission spectra (curcumin, CCNs and acridine orange) were significantly different. The CLSM images of free curcumin and CCNsT-C are shown in Figure 7. Autofluorescence of the curcumin is shown in yellow. The CCNsT is shown in red and acridine orange is shown in green. In this study, acridine orange stain corresponds to cytoplasm. The CLSM images revealed both curcumin and TAMRA inside the cells at different localizations (Figure 7b). The curcumin fluorescence (yellow) was observed in the nucleus (Figure 7b2) whilst CCNsT (red) was found only in the cytoplasm (Figure 7b3). In the control experiment in which free curcumin at the same concentration was incubated with the cells (Figure 7a). The curcumin fluorescence was also observed only in the nucleus (Figure 7a2). The comparison between free curcumin and CCNsT-C, showed that without the CCNsT carriers, the uptake of curcumin into the cells was dramatically reduced. Therefore, it indicated that CCNs could be taken up by the cells and also used as drug carrier. Moreover, this implies that curcumin dissociated from the CCNsT carriers once inside the cells and then entered the nucleus.

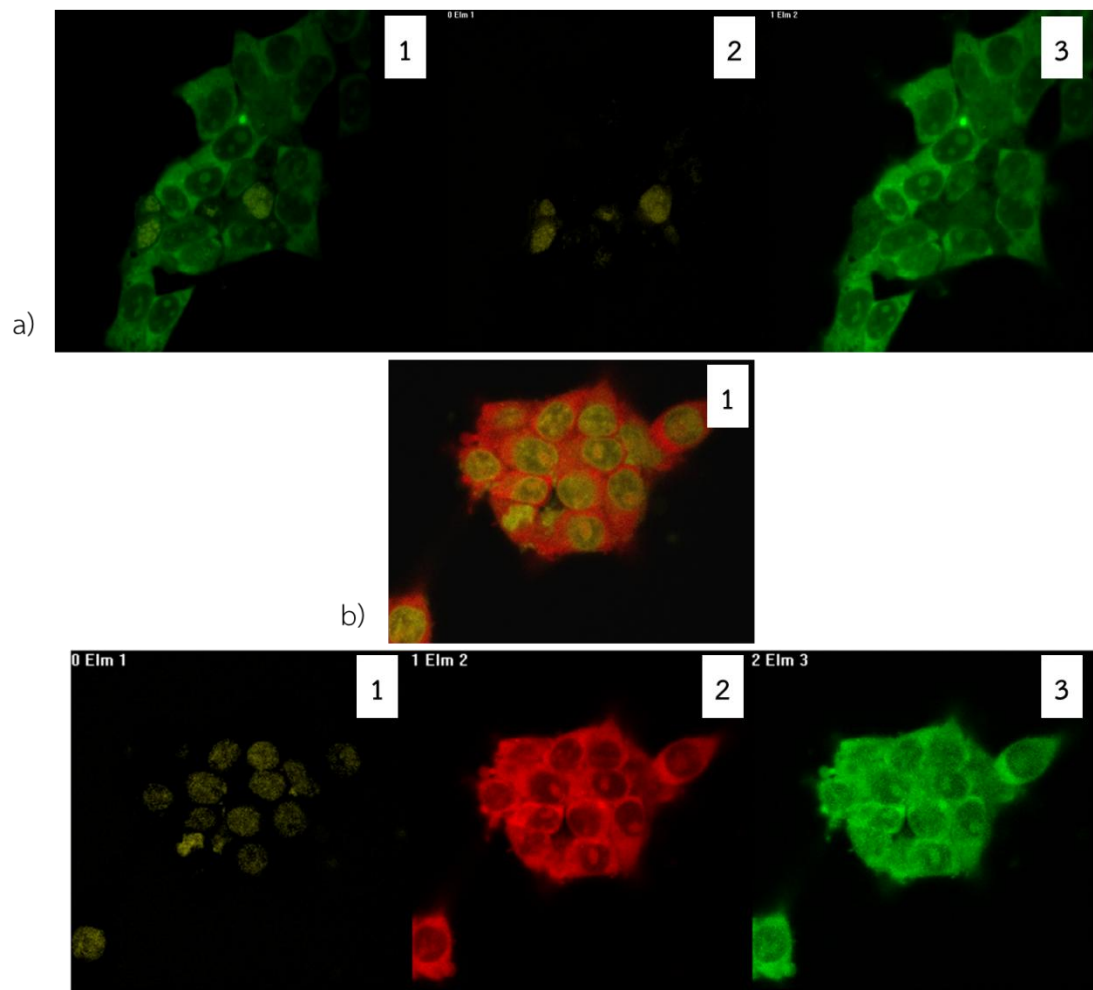


Figure 7 CLSM images of free curcumin (a) and CCNsT-C (b)

3.7. Cytotoxicity of CCNs

To evaluate cytotoxicity of CCNs against human cells, the 3-(4,5-dimethylthiazol-2-yl)-2,5-diphenyltetrazolium bromide (MTT) mitochondrial activity assay was used. The human embryonic kidney 293 cells (HEK293T) and human epidermoid cervical carcinoma cells (CaSki) were used as a model system. The HEK293T cells and CaSki cells were pre-seeded into 96 well plates for 24 h and then were exposed to 0.01-10.0 $\mu\text{g/mL}$ CCNs for 48 h. At the CCNs concentrations of 1.0 $\mu\text{g/mL}$, the cell viability was 102% and 90% for the HEK293T and CaSki cells, respectively (Figure 4.13). At higher concentration of CCNs of 10.0 $\mu\text{g/mL}$, the cell viability decreased to 86% and 74%, respectively. The relatively low *in vitro* cytotoxicity of the CCNs indicated the biocompatibility of CCNs. The results indicated that CCNs is non-cytotoxic at concentrations of $\leq 10.0 \mu\text{g/mL}$.

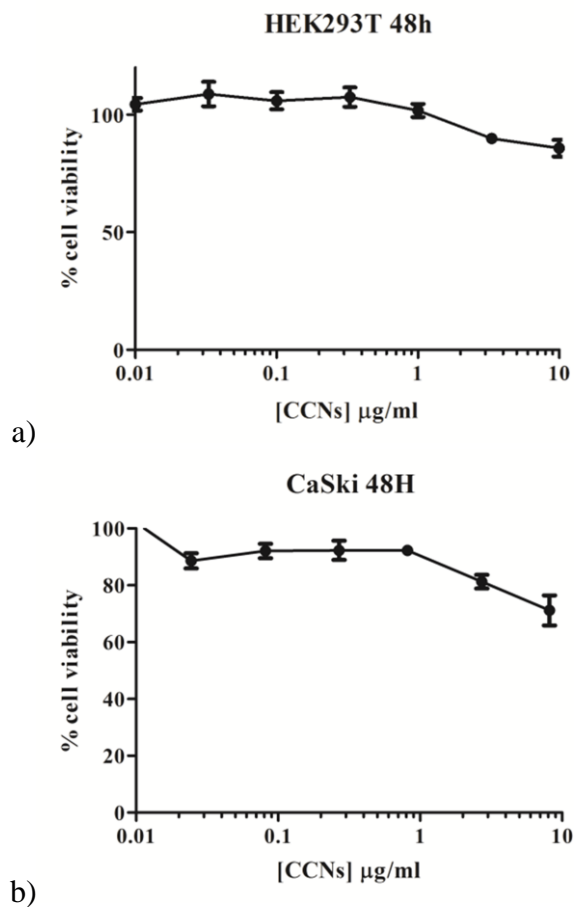


Figure 8 Cytotoxicity of various concentrations of CCNs in HEK293T (a) and CaSki (b) cells after 48 h incubation as determined by MTT assay

4. Conclusion

A new nano-architectural form of carbon-based material, CCNs of approximately 130 nm diameter spheres, were synthesized through a sonication assisted oxidation/exfoliation of graphite or GNPs, and then centrifugally separated from other nanostructures. TEM analysis revealed that the CCNs were likely to be composed of an aggregate of 5 nm hollow particles (giant fullerenes) and GOSh. Although CCNs is first reported here, its structure resembles the theoretically studied carbon nano-structure presented earlier [35]. CCNs appear to be able to be used as an effective drug carrier and offers (i) a 19% (w/w) loading of curcumin, a hydrophobic drug with a π conjugation substructure, (ii) the ability to be taken up into the cells, probably by endocytosis, (iii) the ability to release the loaded curcumin once inside the cells, (iv) non-invasiveness of the CCNs to the nucleus, and (v) a low cytotoxicity when used at $\leq 3.3 \mu\text{g/mL}$. The evaluation of CCNs as a delivery system for high potency anti-cancer drugs, such as paclitaxel, is warranted.

5. References

1. Kroto, H. W.; Heath, J. R.; O'Brien, S. C.; Curl, R. F.; Smalley, R. E., C₆₀: Buckminster fullerene. *Nature* **1985**, 318, 162-163.
2. Smalley, R. E., Self-assembly of the Fullerenes. *Accounts Chem Res* **1992**, 25, 98-105.
3. Rietmeijer, F. J. M.; Rotundi, A.; Heymann, D., C₆₀ and Giant Fullerenes in Soot Condensed in Vapors with Variable C/H Ratio. *Fuller Nanotub Car N* **2004**, 12, 659-680.
4. Iijima, S.; Ajayan, P. M.; Ichihashi, T., Growth Model for Carbon Nanotubes. *Phys Rev Lett* **1992**, 69, 3100-3103.
5. Ugarte, D., Curling and Closure of Graphitic Networks under Electron-beam Irradiation. *Nature* **1992**, 359, 707-709.
6. Kasuya, D.; Yudasaka, M.; Takahashi, K.; Kokai, F.; Iijima, S., Selective Production of Single-wall Carbon Nanohorn Aggregates and Their Formation Mechanism. *J Phys Chem B* **2002**, 106, 4947-4951.
- 7 Muszynski, R.; Seger, B.; Kamat, P. V., Decorating Graphene Sheets with Gold Nanoparticles. *J Phys Chem C* **2008**, 112, 5263-5266.
8. Xu, Y.; Liu, Z.; Zhang, X.; Wang, Y.; Tian, J.; Huang, Y.; Ma, Y., A Graphene Hybrid Material Covalently Functionalized with Porphyrin: Synthesis and Optical Limiting Property. *Adv Mater* **2009**, 21, 1275-1279.
9. Yoshitake, T.; Shimakawa, Y.; Kuroshima, S.; Kimura, H.; Ichihashi, T.; Kubo, Y., Preparation of Fine Platinum Catalyst Supported on Single-wall Carbon Nanohorns for Fuel Cell Application. *Physica B* **2002**, 323, 124-126.
10. Ni, G.-X.; Zheng, Y.; Bae, S.; Tan, C. Y.; Kahya, O.; Wu, J., Graphene-

Ferroelectric Hybrid Structure for Flexible Transparent Electrodes. *ACS Nano* **2012**, *6*, 3935-3942.

11. Xu, L. R.; Bhamidipati, V.; Zhong, W.-H.; Li, J.; Lukehart, C. M.; Lara-Curzio, E., Mechanical Property Characterization of a Polymeric Nanocomposite Reinforced by Graphitic Nanofibers with Reactive Linkers. *J Compos Mater* **2004**, *38*, 1563-1582.

12. Liu, Y.; Yu, D.; Zeng, C.; Miao, Z.; Dai, L., Biocompatible Graphene Oxide-Based Glucose Biosensors. *Langmuir* **2010**, *26*, 6158-6160.

13. Wang, X.; Zhi, L.; Tsao, N.; Tomović, Ž.; Li, J.; Müllen, K., Transparent Carbon Films as Electrodes in Organic Solar Cells. *Angew Chem* **2008**, *120*, 3032-3034.

14. Kim, J.; Cote, L. J.; Kim, F.; Yuan, W.; Shull, K. R.; Huang, J., Graphene Oxide Sheets at Interfaces. *J Am Chem Soc* **2010**, *132*, 8180-8186.

15. Bekyarova, E.; Murata, K.; Yudasaka, M.; Kasuya, D.; Iijima, S.; Tanaka, H.; Single-wall Nanostructured Carbon for Methane Storage. *J Phys Chem B* **2003**, *107*, 4681-4684.

16. Hu, W.; Peng, C.; Luo, W.; Lu, M.; Li, X.; Li, D.; Graphene-Based Antibacterial Paper. *ACS Nano* **2010**, *4*, 4317-4323.

17. Wick, P.; Manser, P.; Limbach, L. K.; Dettlaff-Weglikowska, U.; Krumeich, F.; Roth, S., The Degree and Kind of Agglomeration Affect Carbon Nanotube Cytotoxicity. *Toxicol Lett* **2007**, *168*, 121-131.

18. Zhang, X.; Yin, J.; Peng, C.; Hu, W.; Zhu, Z.; Li, W., Distribution and Biocompatibility Studies of Graphene Oxide in Mice after Intravenous Administration. *Carbon* **2011**, *49*, 986-995.

19. Heister, E.; Neves, V.; Tîlmaciu, C.; Lipert, K.; Beltrán, V. S.; Coley, H. M., Triple

Functionalisation of Single-walled Carbon Nanotubes with Doxorubicin, a Monoclonal Antibody, and a Fluorescent Marker for Targeted Cancer Therapy. *Carbon* **2009**, 47, 2152-2160.

20. Lacerda, L.; Pastorin, G.; Gathercole, D.; Buddle, J.; Prato, M.; Bianco, A., Intracellular Trafficking of Carbon Nanotubes by Confocal Laser Scanning Microscopy. *Adv Mater* **2007**, 19, 1480-1484.

21. Liu, Z.; Chen, K.; Davis, C.; Sherlock, S.; Cao, Q.; Chen, X., Drug Delivery with Carbon Nanotubes for In vivo Cancer Treatment. *Cancer Res* **2008**, 68, 6652-6660.

22. Yang, X.; Zhang, X.; Liu, Z.; Ma, Y.; Huang, Y.; Chen, Y., High-Efficiency Loading and Controlled Release of Doxorubicin Hydrochloride on Graphene Oxide. *J Phys Chem C* **2008**, 112, 17554-17558.

23. Zhang, L.; Lu, Z.; Zhao, Q.; Huang, J.; Shen, H.; Zhang, Z., Enhanced Chemotherapy Efficacy by Ssequential Delivery of siRNA and Anticancer Drugs using PEI-grafted Graphene Oxide. *Small* **2011**, 7, 460-464.

24. Zhang, L.; Xia, J.; Zhao, Q.; Liu, L.; Zhang, Z., Functional Graphene Oxide as a Nanocarrier for Controlled Loading and Targeted Delivery of Mixed Anticancer Drugs. *Small* **2010**, 6, 537-544.

25. Shi, X.; Sitharaman, B.; Pham, Q. P.; Liang, F.; Wu, K.; Edward Billups, W., Fabrication of Porous Ultra-short Single-walled Carbon Nanotube Nanocomposite Scaffolds for Bone Tissue Engineering. *Biomaterials* **2007**, 28, 4078-4090.

26. Zanello, L. P.; Zhao, B.; Hu, H.; Haddon, R. C., Bone Cell Proliferation on Carbon Nanotubes. *Nano Lett* **2006**, 6, 562-567.

27. Sun, X.; Liu, Z.; Welsher, K.; Robinson, J.; Goodwin, A.; Zaric, S.,

- Nano-Graphene Oxide for Cellular Imaging and Drug Delivery. *Nano Res* **2008**, 1, 203-212.
28. Wang, S.; Tang, L. A. I.; Bao, Q.; Lin, M.; Deng, S.; Goh, B. M., Room-Temperature Synthesis of Soluble Carbon Nanotubes by the Sonication of Graphene Oxide Nanosheets. *J Am Chem Soc* **2009**, 131, 16832-16837.
29. Chuvilin, A.; Kaiser, U.; Bichoutskaia, E.; Besley, N. A.; Khlobystov, A. N., Direct Transformation of Graphene to Fullerene. *Nat Chem* **2010**, 2, 450-453.
30. Kosynkin, D. V.; Higginbotham, A. L.; Sinitskii, A.; Lomeda, J. R.; Dimiev, A.; Price, B. K., Longitudinal Unzipping of Carbon Nanotubes to Form Graphene Nanoribbons. *Nature* **2009**, 458, 872-876.
31. Yuge, R.; Yudasaka, M.; Toyama, K.; Yamaguchi, T.; Iijima, S.; Manako, T., Buffer Gas Optimization in CO₂ Laser Ablation for Structure Control of Single-wall Carbon Nanohorn Aggregates. *Carbon* **2012**, 50, 1925-1933.
32. Zhu, S.; Xu, G., Single-walled Carbon Nanohorns and Their Applications. *Nanoscale* **2010**, 2, 2538-2549.
33. Park, S.; Ruoff, R. S., Chemical Methods for the Production of Graphenes. *Nature Nanotechnol* **2009**, 4, 217-224.
34. Hummers, W. S.; Offeman, R. E., Preparation of graphite oxide. *J Am Chem Soc* **1958**, 80, 1339.
35. Grimme, S.; Mück-Lichtenfeld, C.; Antony, J., Noncovalent Interactions between Graphene Sheets and in Multishell (Hyper)Fullerenes. *J Phys Chem C* **2007**, 111, 11199-11207.

Acknowledgements

Firstly and foremost I would like to express the deepest gratitude to my supervisor, Prof. Masayuki Yamaguchi for supporting, educating, supervision, and give me motivation throughout the completion of my doctoral study even during tough times in my Ph.D. life. I am extremely grateful for his teaching and advice, not only the research methodologies but also many other methodologies in life. Only the words written in here are still not enough to express my feeling. It is a great honor for me to be a member and graduate from Yamaguchi's laboratory. I appreciate all his contributions of time, ideas, and funding to make my Ph.D. experience productive and stimulating. Without his supports, I would not have achieved this far and this thesis would not have been completed.

Secondly, I would like to express my appreciation to Prof. Minoru Terano and Assist. Prof. Shogo Nobukawa, who provided me a lot of valuable support. I also deeply appreciate the members of my committee: Prof. Noriyoshi Matsumi, Associate Prof. Yuki Nagao and Associate Prof. Toshiaki Taniike of JAIST, and Assoc. Prof. Ken Kojio of Kyushu University for their helpful comments. I am profoundly grateful to Assoc. Prof. Yuki Nagao for his generous hospitality and support throughout my minor research. Further I would like to thank dual degree program (CU-JAIST) Scholarships for financial support during my doctoral study. Without these facilities and sponsorship, I would not have been able to achieve and complete my study.

I would like to express my appreciation to all of my teachers during I was a bachelor and master student in Chulalongkorn University, especially to Assoc. Prof. Supason Wanichwecharungreung for valuable advice during my completion sub-theme research. Without her, I would not have been able to achieve and complete my study.

I am indebted to my colleagues who supported me throughout my study. My special thanks are extended to all present and former members of Yamaguchi Laboratory. Moreover, thank you all Thai members in JAIST and everyone else for their warm love, emotional support and take part in a one of good memory in my life.

Finally, I would like to extend my deepest gratitude to my beloved family, Arayachukiat's family, for their unconditional loves. Without their love, assistance, and encouragement, it is impossible to finish my Ph. D degree.